

Kondo-Majorana coupling in Double Quantum Dots.

by

Jesús David Cifuentes Pardo

Advisor: Luis Gregorio Dias da Silva

MASTER OF SCIENCE

in

Instituto de Física

(Condensed Matter Physics)

UNIVERSIDADE DE SÃO PAULO

(R. do Matão, 1371 - Butantã, São Paulo)

March 6, 2019

© Jesús David Cifuentes Pardo 2017

Abstract

Majorana zero modes (MZMs) appearing at the edges of topological superconducting wires are a promising platform for fault-tolerant quantum computation. Novel proposals use MZMs tunneling inside quantum dots (QDs) to implement quantum architectures because today's precise experimental control over the QD parameters offers the unique possibility of manipulating the Majoranas inside multi-dot systems. In addition, recent experimental works reporting the detection of such quasi-particles together with Kondo anomalies , including a recent paper published by the advisor of this dissertation and collaborators [1], set out to explore the interplay of such Majorana zero-modes with the Kondo effect. The simplest case where Majorana manipulation is possible is in a double quantum dot (DQD). This model shows several possibilities for manipulation of MZM, including different geometric couplings such as linear and T junctions. In this project we perform analytical (non-interacting) and numerical(interacting) quantum transport studies of the transition of the Majorana signature. By tuning the model parameters we show that it is possible to control the localization of the MZM inside the DQD and explore its interplay with the Kondo effect.

Table of Contents

List of Figures	5
1 Abbreviations	9
2 Introduction and Motivation:	
The Pursuit of Majorana Fermions in superconducting wires.	10
2.1 The Kitaev Chain	12
2.1.1 Topological phase transition	15
2.1.2 Non-abelian statistics	17
2.1.3 Real implementations of the Kitaev Chain	19
2.2 Detecting Majorana zero modes using quantum dots	21
2.2.1 Why double quantum dots?	22
2.3 Overview	23
3 Preliminaries	24
3.1 Transport process in quantum dots (QDs)	24
3.2 The Anderson Model	26
3.3 The Kondo Effect	28
3.3.1 Kondo Effect in QDs	30
4 Theory and Methods	32
4.1 Green function formalism	32
4.1.1 Green function of fermion operators and the equations of motion	33
4.1.2 Graph-Gauss-Jordan elimination process: Solving the equations of motion	35
4.1.3 Graph Algorithm	38
4.1.4 Non-interacting DOS in a double quantum dot coupled to a lead	38
4.2 The Numerical Renormalization Group (NRG)	40
4.2.1 From the Renormalization Group to Wilson's Chain	40
4.2.2 Iterative Diagonalization	43
4.2.3 Symmetries	44
4.2.4 Iterative diagonalization in a single QD attached to a metallic lead	44
4.2.5 The Density Matrix Renormalization Group (DM-NRG)	47

Table of Contents

4.2.6	Specifications of the NRG Code	49
4.2.7	NRG results in a double quantum dot coupled to a metallic lead	51
5	Coupling a QD with a Majorana zero mode	54
5.1	Model	54
5.2	Non-interacting QD coupled to Majorana chain	56
5.3	Kondo-Majorana physics	59
6	Coupling the Majorana Zero Mode to a Double Quantum Dot	62
6.1	Applying our methods to the DQD-Majorana system	63
6.1.1	Non-interacting Green function:	63
6.1.2	NRG for the interacting system	65
6.2	Manipulation of Majorana zero modes	65
6.2.1	Non-interacting manipulation	67
6.2.2	Interacting manipulation	70
6.3	Additional results	74
6.3.1	Indirect exchange through the Majorana mode	75
6.3.2	Indirect Majorana coupling through the lead	77
6.3.3	Critical behavior in zero-bias DOS	77
7	Conclusions	78
	References	79
	Bibliography	80

Appendices

A	Appendix	87
A.1	From the logarithmic discretization to the Wilson's chain.	87
A.2	Initial DQD-Majorana Hamiltonian.	91

List of Figures

2.1	Coffee→donut: adiabatic evolution	10
2.2	Illustration of the Kitaev chain for open boundary conditions in the Majorana representation. Dirac fermions are depicted by the big globes. Each one of them contains two Majoranas (small blue and red circles) a)Represents the trivial case where the hopping and the superconducting term approaches to 0. b) The non-trivial topological phase. The coupling is produced between Majoranas in different Dirac fermions <i>By the author</i>	13
2.3	Spectrum of Hamiltonian Equation 2.5 with 30 sites and $t = \Delta $ s. Method: Numerical diagonalization. <i>By the author</i>	14
2.4	Path of \hat{H}_k for the interval $[-\pi, \pi]$. a) Trivial phase: The resulting path can be homotopically deformed to a point. b) Non-trivial phase: The path is a non-contractible loop around the unitary circle. <i>By the author</i>	16
2.5	Representation of non-abelian braiding	18
2.6	(a) Setup of a Majorana wire with high spin-orbit coupling, over a superconducting plane and an induced Zeeman field. (b) Splitting of the energy bands with different spins in the non-superconducting regime (red and yellow bands). With superconducting proximity , a gap is opened and the red and blue energy bands are projected forming the black bands. <i>Adapted from [2]</i>	20
2.7	(a) Experimental setup (b) Observed magnetic field dependance of the zero bias peak. <i>[3]</i>	21
2.8	a) Braiding proposal b) Basic architecture with four Majorana Zero Modes in a scalable quantum computer. <i>Adapted from (a) [4] (b) [5]</i>	22
3.1	a) Vertical quantum dot. b)Atomic force microscopy picture of two coupled lateral QDs (bright central circles). Gates 1 and 2 act as drain and source voltage. A negative voltage is applied at gates A, B to allow the formation of the droplets inside the free space in the 2D electron gas. <i>Adapted from [6]</i>	24
3.2	Representation of the Density of States of a QD. The gate potential V_G can be tuned to change the fermi energy of the dot.	25

LIST OF FIGURES

3.3	(a) Representation of transport through QD. The red curve represents the hybridized energy level. The gate voltage tunes this level. In the case represented, the energy level is in the middle of the drain and source voltages allowing transport between the leads. (b) Charging diagram of a quantum dot. Differential conductance dependence over the gate voltage V_G and the source-drain voltage ($V_{SD} = V_S - V_D$). Coulomb blockade occurs at the diamond-shaped regions with zero conductance. At these regions the number of electrons is constant and increases 1 by 1 when the gate voltage is scaled up. <i>(b) Adapted from [7]</i>	26
3.4	(a) Resistivity minimum near the Kondo temperature T_k . (b) Kondo cloud formed by a singlet grouped around the impurity divided in spin- \uparrow ,spin- \downarrow regions. <i>Adapted from a) [8], b) [9]</i>	29
3.5	Observation of the Kondo effect in a single electron transistor. Color scale temperatures from 15mk (Black) to 800mk(Red) a) Dependence of the zero bias conductance over the gate voltage. A plato in the conductance peak appears in the odd particle regimes. b) Dependence of the conductance over the gate source drain voltage inside an odd electron regime. A zero bias conductance peak (ZBCP) of height $\frac{2e^2}{h}$ is observed. This is the Kondo signature. <i>Adapted from [10]</i>	31
4.1	Graph representation of Gauss-Jordan elimination a) Graph $\mathcal{G}_{d_1 d_2}$ b) After the elimination of vertex c_k , the energies of dots d_1 and d_2 , and the coupling parameter are changed. c) After Gaussian elimination of dot 2 the energy of the remaining dot $\varepsilon_D QD^+$ represents the transport information through d_1 of the entire DQD.	36
4.2	Evolution of the density of states at each QD (Left: dot 1, Right: dot 2) at three distinct arrangements of DQD-lead coupling. The inset at the first column depicts the type of coupling. The purple line represents the tuning variable. The energy unit is Γ_1 . $e_1 = e_2 = 0$ in all arrangements. (a),(b) The lead is connected to both QDs. Tuning variable: Γ_2 . (c)(d) Indirect coupling of the second dot through dot one. Tuning variable: t_{dots} . (e)(f) Triangular coupling. Tuning variable: t_{dots}	39
4.3	NRG algorithm: The logarithmic discretization of the conduction band according to the discretization parameter Λ . The system with the lead attached to the QD-impurity is mapped to the Wilson's chain, such that each step of the chain contains the contributions at different energy scales $\Lambda^{-N/2}$	41
4.4	Schematic representation of the spectrum in the iterative diagonalization process. a)→b): Rescaling. b)→c): Including next site and diagonalizing. c)→d): Truncation of high energy states. <i>Adapted from [11]</i>	43
4.5	Evolution of the QD-spectrum vs number of iterations of the code for $U' = 0.5$, $\varepsilon' = -0.25$, $\Gamma = 2.82 \times 10^{-2}$	46
4.6	Wilson's chain depicted as an open quantum system. Adapted from [12].	49

LIST OF FIGURES

4.7	Diagram of the NRG code	50
4.8	Density of states for the DQD attached to the lead at different configurations. Left insets: Setup that is being used. Right insets: Low energy DOS.	52
5.1	Model for the QD-Majorana system. Solid lines: Hopping interactions: V_1 couplings of QD1 . Dashed lines: Majorana spin- \downarrow effective couplings (Equation 5.2) t_1 . The atomic energy levels appear inside each QD ε_1 are tuned by the gate voltages. The coulomb interaction is represented by U_1 separates two energy levels. The red dashed horizontal lines represent the Fermi level.	55
5.2	Graph \mathcal{G}_M representing the transport equations.	57
5.3	Density of states for a Majorana coupled to a QD under the tuning of different parameter. The tuning parameter is drawn in purple line in the inset model.	58
5.4	DOS at $t_1 = \Gamma_1$ at the PHS-point. Insets: Left: QD-Majorana model. Right: Zoom to low energy DOS.	59
5.5	(a)&(b): Dependance of the DOS over the gate voltage $\Delta\varepsilon_1$ at $t_1 = \Gamma_1$. (a)Spin- \uparrow (b) Spin- \downarrow . (c) DOS at the red-dashed horizontal cut in (a)&(b). Insets: Left: QD-Majorana model. Right: Low energy DOS. (d) DOS at the Green-dashed vertical cut in (a)&(b).	60
5.6	Dependence of the zero-bias conductunce over tuning voltage Adapted from [1].	60
6.1	Model for the DQD-Majorana system. Solid lines: Hopping interactions (t_{dots} : inter-dot coupling , V_1, V_2 couplings of QD1 and QD2 with the lead.). Dashed lines: Majorana spin- \downarrow effective couplings (Equation 5.2) t_1, t_2 . The atomic energy levels appear inside each QD $\varepsilon_1, \varepsilon_2$ are tuned by the gate voltages. The coulomb interaction is represented by U_1, U_2 . The red dashed horizontal lines represent the Fermi level.	62
6.2	Graph method applied to a DQD coupled to a Majorana zero mode. a) Initial stage. b) Eliminated vertexes $c_k^\dagger, c_k, d_{2,\downarrow}, d_{2,\downarrow}^\dagger$ in that order. c) Eliminated vertexes $d_{1,\downarrow}^\dagger$ and f_\downarrow , the final energy is $\omega - G_{d_1, d_1^\dagger}(\omega)$	64
6.3	66
6.4	Non-interacting DOS in the symmetric coupling(Figure 6.3(a)) at each QD. First column: Dot 1. Second column: Dot 2. The gate voltages vary at each row. First row: Zero-bias in both dots $\varepsilon_1 = \varepsilon_2 = 0$. Second row: $\varepsilon_1 = 5\Gamma_1, \varepsilon_2 = 0$. Third row: $\varepsilon_1 = 0, \varepsilon_2 = -5\Gamma_1$. Bold blue lines: Spin- \uparrow DOS. Thin red lines: Spin- \downarrow DOS. The insets at the right show which dot carries a Majorana signature, represented by a red dashed circle. Upper: First dot. Lower: Second dot.	67

LIST OF FIGURES

6.5 Non-interacting DOS of the T-dot coupling Figure 6.3(b). (b). First line (a),(b): $\varepsilon_1 = \varepsilon_2 = 0$. Second line (c),(d): $\varepsilon_1 = 5\Gamma_1$, $\varepsilon_2 = 0$. Third line (e),(f): $\varepsilon_2 = -5\Gamma_1$, $\varepsilon_1 = 0$. Blue bold lines: Spin- \uparrow DOS. Red thin lines: Spin- \downarrow DOS. The inset at the upper-right corner of each line indicates which dots exhibit Majorana signature, which is represented by a red dashed circle inside the dot.	68
6.6 Non-interacting DOS of the set up in Figure 6.3(c). First line (a),(b): $\varepsilon_1 = \varepsilon_2 = 0$. Second line (c),(d): $\varepsilon_1 = 5\Gamma_1$, $\varepsilon_2 = 0$. Third line (e),(f): $\varepsilon_2 = -5\Gamma_1$, $\varepsilon_1 = 0$. Blue bold lines: Spin- \uparrow DOS. Red thin lines: Spin- \downarrow DOS. The inset at the upper-right corner of each line indicates which dots exhibit Majorana signature, which is represented by a red dashed circle inside the dot.	69
6.7 Density of states of both dots in the symmetric coupling without gate voltages between the Majorana and the interacting DQD. Bold blue lines: Spin- \uparrow DOS. Thin red lines: Spin- \downarrow DOS. Inset: Low-energy DOS.	70
6.8 (a)-(d) Dependence of the density of states of setup in Figure 6.3(a) over ω and the gate voltage $\Delta\varepsilon_2$. $\Delta\varepsilon_1 = 0$ Up: Dot 1. Down: Dot 2. Left: Spin- \uparrow . Right: Spin- \downarrow . (e) Evolution of the relation $\frac{\rho_{\uparrow}(0)}{\rho_{\downarrow}(0)}$ for both QDs. While QD2 losses rapidly the Majorana signature, QD1 maintains it till $\Delta\varepsilon_2 \sim 5$	71
6.9 The same as in Figure 6.4 for the interacting DOS in the symmetric coupling setup (Figure 6.3).	72
6.10 The same as in Figure 6.4 for the interacting DOS of the T-dot junction Figure 6.3(b). Inset in b): Low-energy DOS.	73
6.11 Logarithmic dependence of the density of states in setup Figure 6.3(c) over ω and the gate voltage $\Delta\varepsilon_1$. $\Delta\varepsilon_2 = 0$. The dependence over $\Delta\varepsilon_2$ produces similar results.	73
6.12 The same as in Figure 6.4 for the interacting DOS of the setup in Figure 6.3(b). Inset in b): Low-energy DOS.	74
6.13 Dependence of the DOS in the symmetric model Figure 6.3(a) over $t_1 = t_2$ and ω . Up: High energy . Down: Zoom to low energy states.	75
6.14 Dependence of the DOS in the symmetric model Figure 6.3(a) over $t_1 = t_2$ and ω . Up: High energy . Down: Zoom to low energy states.	76
6.15 DOS at both dots for the model in the left inset. The right inset zooms the low-energy DOS in the second dot.	76
6.16 Logarithmic dependence of the DOS in the second dot for setup in Figure 6.3(b) over the second gate voltage. Cut at $5\Gamma_1$ corresponds to Figure 6.10(f).	77
7.1 Table of Majorana signatures in the studied cases. Non-interacting	79

Chapter 1

Abbreviations

Chapter 2

Introduction and Motivation: The Pursuit of Majorana Fermions in superconducting wires.

"It started out with a toy model demonstration, and then I realized it was very good model. You don't understand the full implications until other people start thinking it is true and they observe the big picture [...] Now, that toy model is like Hydrogen atom for topological materials- it turned out to be the first example of topological quantum matter."

– F. Duncan M. Haldane

In 2001 Alexei Yu Kitaev presented a toy model that could lead to the implementation of topological qubits [13], an innovative idea that promised to sort out the problem of high decoherence in quantum computation. Kitaev used the properties of an exotic quasi-particle bound at the edges of a superconducting wire. This "bound state" was cataloged as a "Majorana fermion", the iconic particle predicted by Ettore Majorana in the 1930s. Majoranas were initially proposed as a real field solution of the Dirac equation, which describes fermions that are their own antiparticle[14]. So far, no fundamental particle with these characteristics has been observed. However, novel exciting proposals are oriented to search these particles at the boundaries of topological superconducting wires.

These "topological superconductors" belong to an emergent group of materials that experience phase transitions without passing through a symmetry breaking, meaning that they cannot be characterized by Landau theory. Instead, these phases of matter are described by a new type



Figure 2.1: Coffee→donut: adiabatic evolution

of order determined by topology. In mathematics, the word topology is used to describe non-local features of surfaces (or manifolds) that are preserved under smooth deformations. The cliché, but always educative, joke to explain this concept says that "Topologists cannot tell the difference between a donut and a coffee cup, since one of them can always be continuously deformed into the other through a sequence of smooth and small alterations" (Figure 2.1).¹ However it wouldn't be possible to topologically transform a soccer ball into a donut since no there is no way of putting a hole into the ball by performing smooth deformations. We then say that coffee and donuts are topologically equivalent to each other, but not to the ball.

The insight of topology into the field of condensed matter physics is the following. Those materials who are attributed a topological characterization are endowed with a characteristic stability under smooth deformations (or adiabatic evolutions). Moreover, they usually present exotic excitations at its boundaries . The most famous example of this behavior is the integer quantum hall effect (IQHE), which exhibits an insulating bulk with electron currents passing through the edges of the material. More importantly, the magnetic field defines conductive platoes representing different topological phases. This effect is so robust that it allowed to define with high precision a resistivity standard unit $R_K = \frac{h}{e^2} = 25812.807557(18)\Omega$, which had major impact in science and technology.

Kitaev's toy model describes a one dimensional topological chain. Similar to the IQHE, this chain exhibits bizarre edge states, which are documented as bounded Majorana quasi-particles . Besides topological protection, these Majoranas have another important characteristic. Displayed in multi-state system Majoranas can display anionic non-abelian statistics [15]. This means that if we have three Majorana fermions γ_1, γ_2 and γ_3 and we, somehow, get to exchange the first two Majoranas and then the second and the third, it produces a different state than exchanging the last two Majoranas first and then the first two. This is a very interesting property for quantum computing since it allows to encode information in many body systems. Kitaev pointed out that the combination of these two properties of Majoranas, topological stability and non-abelian statistics, could lead to the implementation of fault-tolerant quantum computers . This marked the beginning of a new area called topological quantum computing [16], which combines areas as different as topology, knot theory [17] and condensed matter physics.

These ideas motivated the pursuit of Majorana fermions in condensed matter systems [2, 18–20]. Indeed, the last decade has been full of excitement, as new experiments have turned some of the theoretical predictions of the 1990s and 2000s into reality. Very recently the first evidence of Majorana end states in TS has been found in multiple experiments [3, 21–24] following the prescription by Oreg et al. [25] and Lutchyn et al. [26]. These experiments have been based on tunneling spectroscopy in junctions between TS and non metallic (NM) leads, where resonances have been observed at zero energy, consistent with the presence of Majorana zero-energy modes.

In the following section we will present a review of the main ideas behind the Kitaev chain (section 2.1) taking special attention on its topological characterization and non-abelian

¹For decades, this has been the main reason for the absence of donuts at topology workshops.

statistics. Finally, we will tell how that model inspired real implementations of Majorana wires in subsection 2.1.3. This discussion will eventually bring us closer to the main motivation of this thesis which is taken in the next section: The detection Majorana zero modes using quantum dots.

2.1 The Kitaev Chain

Kitaev's tight binding toy model represents an spinless superconducting chain with the following Hamiltonian

$$H = \sum_{i=1}^N \left[-t(a_i^\dagger a_{i+1} + a_{i+1}^\dagger a_i) - \mu a_i^\dagger a_i + \Delta a_i a_{i+1} + \Delta^* a_{i+1}^\dagger a_i^\dagger \right]. \quad (2.1)$$

Where μ is the chemical potential, so that $\mu a_i^\dagger a_i$ is the energy associated to each step in the chain, and $t(a_i^\dagger a_{i+1} + a_{i+1}^\dagger a_i)$ represents the interaction between neighboring sites which is determined by the hopping term t . The remaining terms describe the superconducting properties of the system as it is established by the BCS theory of superconductivity. Here, Δ is a complex superconducting parameter with the form $\Delta = e^{i\theta} |\Delta|$. The associated terms represent the Cooper pairs which can be created or annihilated at neighboring sites of the system hence breaking particle number. However, the system still preserves fermion parity, a property that will be very important during the rest of the project.

There are different ways to diagonalize this Hamiltonians. The usual method is to perform a Bogoliubov-de Gennes transformation which makes the problem equivalent to diagonalize a $2N \times 2N$ -matrix. However, Kitaev's brilliant solution passes through another transform. Lets define the operators $\gamma_{A,j}$ and $\gamma_{B,j}$ such that

$$\gamma_{A,j} = e^{i\theta/2} a_j + e^{-i\theta/2} a_j^\dagger, \quad \gamma_{B,j} = -i(e^{i\theta/2} a_j - e^{-i\theta/2} a_j^\dagger). \quad (2.2)$$

It is simple check that these operators are self-adjoint ($\gamma_{A,j}^\dagger = \gamma_{A,j}$, $\gamma_{B,j}^\dagger = \gamma_{B,j}$) , which implies that they are their own antiparticle. Moreover, they satisfy the fermion anti-commutation relations

$$\begin{aligned} \{\gamma_{A,i}, \gamma_{A,j}\} &= \{\gamma_{B,i}, \gamma_{B,j}\} = 2\delta_{ij}, \\ \{\gamma_{A,i}, \gamma_{B,j}\} &= 0. \end{aligned} \quad (2.3)$$

These relations are characteristic from a Clifford algebra, which basically describes a fermion which is its own antiparticle. A Majorana fermion. Thus, we can think $\gamma_{A,i}, \gamma_{B,i}$ as Majorana operators.

Taking the inverse of (2.2) we obtain that each (Dirac) fermion in Hamiltonian (2.1) is composed by two Majorana fermions such that

$$a_j = \frac{e^{-i\theta/2}}{2} (\gamma_{A,j} + i\gamma_{B,j}), \quad a_j^\dagger = \frac{e^{i\theta/2}}{2} (\gamma_{A,j} - i\gamma_{B,j}). \quad (2.4)$$

2.1. The Kitaev Chain

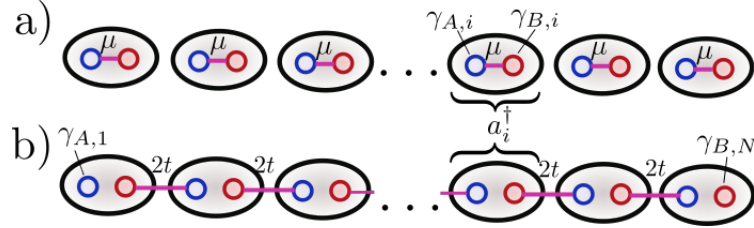


Figure 2.2: Illustration of the Kitaev chain for open boundary conditions in the Majorana representation. Dirac fermions are depicted by the big globes. Each one of them contains two Majoranas (small blue and red circles) a)Represents the trivial case where the hopping and the superconducting term approaches to 0. b) The non-trivial topological phase. The coupling is produced between Majoranas in different Dirac fermions *By the author*

Hence, we could adventure to say that these Majorana operators are actually splitting the Dirac fermions into real(γ_A) and imaginary (γ_B) part ,the same way as complex numbers are a composite of two real numbers. This is just a possible interpretation to elucidate that each Dirac fermion is composed by two types of Majorana quasi-particles just as in Figure 2.2.

The new Kitaev Hamiltonian in the "Majorana representation" looks like

$$H = \frac{i}{2} \sum_{j=1}^N [-\mu \gamma_{A,j} \gamma_{B,j} + (t + |\Delta|) \gamma_{B,j} \gamma_{A,j+1} + (t - |\Delta|) \gamma_{A,j} \gamma_{B,j+1}] + \text{Const}, \quad (2.5)$$

Depending on the values of parameters μ, t and $|\Delta|$ we can identify two regimes represented by the following situations:

1. If $|\Delta| = t = 0$ and $\mu < 0$, Hamiltonian (2.5) becomes $-\frac{i\mu}{2} \sum_j \gamma_{A,j} \gamma_{B,j}$ which represents the coupling of the Majoranas in the same Dirac fermion. (See Figure 2.2 (a))
2. If $|\Delta| = t > 0$ and $\mu = 0$, the situation is much more interesting. The Hamiltonian (2.5) takes the form $H = 2ti \sum_j \gamma_{B,j} \gamma_{A,j+1}$. This implies that the coupling is performed between Majoranas of different Dirac fermions. Notably, this configuration leaves the edge Majorana operators ($\gamma_{A,1}$ and $\gamma_{B,N}$) uncoupled to the system (See Figure Figure 2.2b)). Note that these uncoupled Majorana fermions can be at any state without any repercussion in the energy of the system. This explains the emergence of a ground state localized at edges of the chain.

These two situations are representatives of two different topological phases. The trivial phase occurs for $\frac{\mu}{2t} > 1$ and the non-trivial phase appears when $\frac{\mu}{2t} < 1$ (See Figure 2.3). The main characteristic of the non-trivial phase is the creation of a robust zero-mode generated by the uncoupled Majorana fermions at the edges of the Kitaev chain. Note that if

$$H = 2ti \sum_j \gamma_{B,j} \gamma_{A,j+1}, \quad (2.6)$$

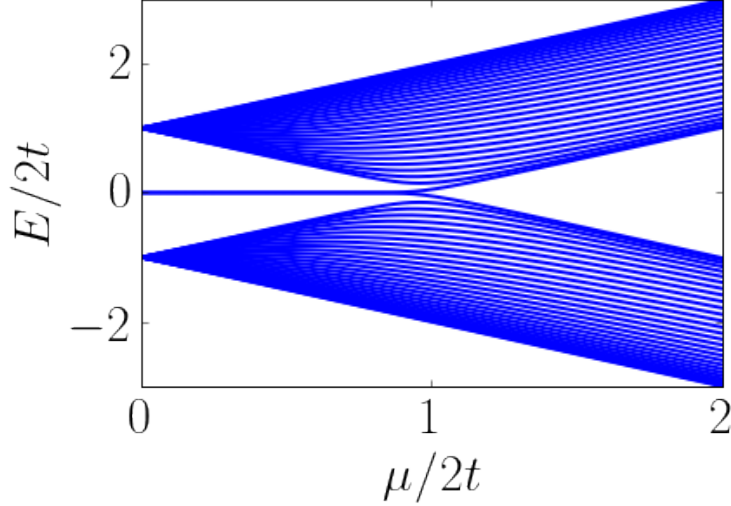


Figure 2.3: Spectrum of Hamiltonian 2.5 with 30 sites and $t = |\Delta|$ s. Method: Numerical diagonalization. *By the author*

it is possible to define new Dirac fermion operators as

$$c_j = \frac{1}{\sqrt{2}} (\gamma_{B,j} + i\gamma_{A,j+1}), \quad c_j^\dagger = \frac{1}{\sqrt{2}} (\gamma_{B,j} - i\gamma_{A,j+1}).$$

Then (2.7) becomes

$$H = ti \sum_{j=1}^{N-1} (2c_j^\dagger c_j - 1). \quad (2.7)$$

Therefore, a ground state $|\Omega\rangle$ of this Hamiltonian is an state vacuum at all sites j from 1 to $N-1$ ($c_j|\Omega\rangle = 0$). This condition allows some degeneracy since the sites at the boundary are not coupled to the Hamiltonian $\gamma_{A,1}$ and $\gamma_{B,N}$. The Dirac operators formed by these Majoranas

$$c_N = \frac{1}{\sqrt{2}} (\gamma_{B,N} + i\gamma_{A,1}), \quad c_N^\dagger = \frac{1}{\sqrt{2}} (\gamma_{B,N} - i\gamma_{A,1}),$$

can be either occupied ($c_N^\dagger c_N|\Omega\rangle = 1$) or empty ($c_N^\dagger c_N|\Omega\rangle = 0$). Each of these results will have a different fermion parity, that is a symmetry of our Hamiltonian. Indeed, we can define a global parity operator as

$$\mathcal{P} = \prod_{i=1}^N (2c_i^\dagger c_i - 1) = \prod_{i=1}^N -i\gamma_{B,i}\gamma_{A,i+1} = \pm 1. \quad (2.8)$$

In the ground state $|\Omega\rangle$, this parity will be defined by the result of $\gamma_{B,N}\gamma_{A,1}$ because the other states are fixed by ($c_j|\Omega\rangle = 0$). This is an important point, since symmetry protection is actually

correlating the two opposite sites of the Kitaev chain i.e. Any attempt to disturb one site of the chain would perturb the other site to guarantee the preservation of fermion parity This is a great deal, it shows how coherent are these Majorana edge states. A possible explanation for this is the topology of the Kitaev chain, which is the objective of the next subsection.

2.1.1 Topological phase transition

Both regimes described previously can be characterized with a topological parameter. A didactic method to explain is the one used by Alicea[2]. First of all, suppose that we have an infinite Kitaev chain chain ($N = \infty$) in (2.5). This system is translation invariant, hence we can make a Fourier transformation to the momentum space as

$$H = \sum_{k \in BZ} (b'_k \ c'_k) H_k \begin{pmatrix} b'_{-k} \\ c'_{-k} \end{pmatrix}, \quad (2.9)$$

with the Bloch Hamiltonian equal to

$$H_k = \begin{pmatrix} 0 & \frac{-i\mu}{2} + it \cos k + |\Delta| \sin k \\ \frac{i\mu}{2} - it \cos k + |\Delta| \sin k & 0 \end{pmatrix} = (|\Delta| \sin k) \sigma_x + \left(\frac{\mu}{2} - t \cos k \right) \sigma_y. \quad (2.10)$$

Here, σ_x and σ_y are the corresponding Pauli matrices. The Brilloin zone (BZ) is the periodic space $[-\pi, \pi]$ which can be mapped to the unitary circle. Equation (2.10) determines the coordinates of the Bloch Hamiltonian in the base $\{\sigma_x, \sigma_y\}$.

We can map these coordinates to the unitary circle by taking the norm of this vector giving

$$\hat{H}_k = \frac{1}{\sqrt{|\Delta|^2 \sin^2 k + (\frac{\mu}{2} - t \cos k)^2}} \begin{pmatrix} |\Delta| \sin k \\ \frac{\mu}{2} - t \cos k \end{pmatrix}. \quad (2.11)$$

Note that $|\Delta|^2 \sin^2 k + (\frac{\mu}{2} - t \cos k)^2 \neq 0$ for all the values of k as long as $\frac{\mu}{2t} \neq 1$. When $\frac{\mu}{2t} = 1$ the $H_{k=0} = 0$, so it cannot be normalized. This is the same point were the phase transition occurs!. At any other value of $\frac{\mu}{2t}$ it is possible to normalize H_k for all values of $k \in BZ$. The result of mapping \hat{H}_k for all k is a path onto the unitary circle.

This path can take two forms as we can observe in Figure 2.4. If $\frac{\mu}{2t} > 1$ the path is an arc in the part of the circle. In the non-trivial phase $\frac{\mu}{2t} < 1$ the path completes a wind around the circle. This is a topological difference between both phases. While the path described by the trivial phase can be contracted to a single dot, the path described by the non-trivial circle is a circle that cannot be contracted. We can determine whether path of a given phase is of type a) or type b) we only need to check if $\hat{H}_{k=0}$ and $\hat{H}_{k=\pi}$ are the same point $(0, 1)$ or the opposite points $(0, 1)$ and $(0, -1)$. This transforms into a simple equation

$$\hat{H}_{k=0,y} \hat{H}_{k=\pi,y} = \begin{cases} 1 & \text{trivial phase} \\ -1 & \text{non-trivial phase} \end{cases} \quad (2.12)$$

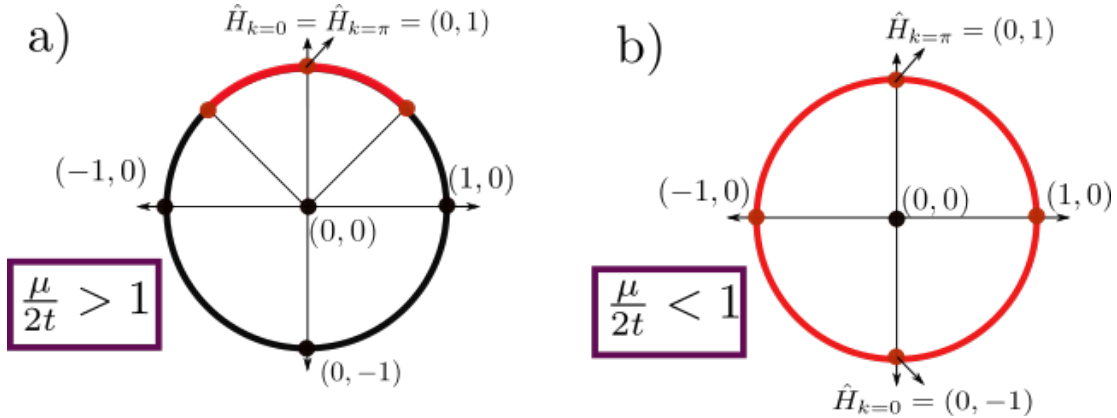


Figure 2.4: Path of \hat{H}_k for the interval $[-\pi, \pi]$. a) Trivial phase: The resulting path can be homotopically deformed to a point. b) Non-trivial phase: The path is a non-contractible loop around the unitary circle. *By the author*

where $\hat{H}_{k=0,y}$ is the y -th component of \hat{H}_k . The term $\hat{H}_{k,y}$ is a particular case of the Pfaffian $\mathcal{P}(k)$, which widely used to characterize topological phase transitions involving Majorana fermions.

In a more general perspective, the main idea behind this topological characterization relies in the adiabatic theorem. In simple words, the adiabatic theorem says that a slow evolution of a gaped Hamiltonian will produce a smooth evolution of its eigenstates, so that the order of energies remains unchanged.

A keyword in the previous definition is "gaped". As we can observe in Figure 2.3 the phase transition occurs at $\frac{\mu}{2t} = 1$. This point is where the gap of the Hamiltonian closes. In periodic boundary conditions no Majorana zero modes will emerge since there are no edges in the system. Therefore, the edge states with zero energy for $\frac{\mu}{2t} < 1$ will not appear. We obtain that the gapless point $\frac{\mu}{2t} = 1$ divides two gapped regimes. According to the adiabatic theorem, these two regions must be separated, hence meaning that no adiabatic evolution could lead from one region to the other since that would involve crossing through a gapless Hamiltonian.

In conclusion, these gapless Hamiltonians are forbidden in an adiabatic evolution. The banned points can be thought as "holes" in the space of Hamiltonians, which generates spaces with non-trivial topologies. Since adiabatic evolutions can be understood as smooth deformations of the Hamiltonian, the relation with topology becomes clear. Thus, characterizing the phase transitions in the Kitaev chain, as in similar robust materials, is mainly a topological problem. This involves computing topological quantities such as Pfaffians, Chern numbers or Winding numbers, which are always integer values.

All of this, lead us to an interesting question. If we have two connected topological materials, one characterized by the number 0 and the other by the number 1, then what should happen at the boundary between these two discrete parameters? Indeed some excitations are

visible at the boundaries of topological materials. In the IQHE, these excitations are quantized currents passing through the edges of the placket. In the Kitaev chain these are the Majorana quasi-particles.

Finally, note that in a system that preserves symmetries, the space of Hamiltonians has more forbidden points. Therefore, these systems have different topological characterizations according to the protected symmetries [27]. This is the case of the Kitaev chain where the topological phase protects the parity of the symmetry under perturbations involving the two opposed Majoranas at the edges. This endowed topological stability combined with Majorana's non-abelian statistics (next subsection) makes the Kitaev chain a promising platform for quantum computation.

2.1.2 Non-abelian statistics

Imagine that we want to exchange two Majorana fermions γ_1 and γ_2 ². This procedure can be performed with an adiabatic evolution of the Hamiltonian $H(t)$ that exchanges both operators while leaving the system invariant. Therefore, after a period T we require that

$$\begin{aligned}\gamma_1(T) &\rightarrow \gamma_2(0) \\ \gamma_2(T) &\rightarrow \gamma_1(0)\end{aligned}\tag{2.13}$$

while $H(0) = H(T)$.

The adiabatic evolution is then represented by a unitary operator $U(t) = e^{-\frac{i}{\hbar} \int H(t)}$ and is applied according to Heisenberg's picture as

$$\gamma_i(T) = U^\dagger(t) \gamma_i U(t).$$

Since Majoranas preserve fermion parity, H must commute with the parity operator $P = -i\gamma_1\gamma_2$. In a Clifford algebra generated by the operators γ_1 and γ_2 (See algebraic relations (2.3)), $[H, \gamma_1\gamma_2] = 0$ implies that $H(t) \propto \gamma_1\gamma_2$ or $H(t)$ is a constant. Taking the non-trivial answer we obtain that the evolution operator has the form $U(t) = e^{\alpha(t)\gamma_1\gamma_2}$, where $\alpha(t)$ is a complex function over t . We can simplify this exponential noting that $(\gamma_1\gamma_2)^2 = -1$ which after Taylor expansion reduces to

$$U(t) = \cos(\alpha(t)) - \gamma_1\gamma_2 \sin(\alpha(t)).\tag{2.14}$$

Replacing this solution in (2.13) we obtain

$$\begin{aligned}\gamma_1(T) &= \gamma_1 \cos(2\alpha(T)) - \gamma_2 \sin(2\alpha(T)) \rightarrow \gamma_2 \\ \gamma_2(T) &= \gamma_2 \cos(2\alpha(T)) + \gamma_1 \sin(2\alpha(T)) \rightarrow \gamma_1,\end{aligned}\tag{2.15}$$

which can only happen if $\alpha(T) = \pm\frac{\pi}{4}$. Hence, we conclude that the exchange operator between both Majoranas is

$$U_{12} = e^{\pm\frac{\pi}{4}\gamma_1\gamma_2} = \frac{1}{\sqrt{2}}(1 \pm \gamma_1\gamma_2).\tag{2.16}$$

²This section is inspired on the webpage topocondmat https://topocondmat.org/w2_majorana/braiding.html, which contains an amazing tutorial about Majorana fermions and topological condensed matter.

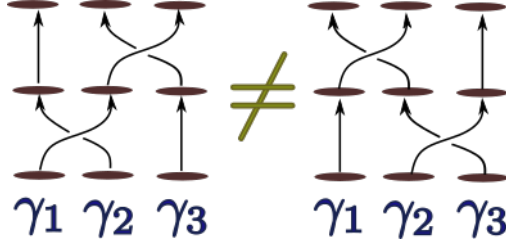


Figure 2.5: Representation of non-abelian braiding .

Note that this exchange does not depend on the evolution, nor the period T .

Now imagine that we have three Majoranas γ_1, γ_2 and γ_3 and we want to perform the following processes. On the first one, we exchange Majoranas 1 and 2 and then the Majorana in 2 (which was initially at 1) is exchanged with Majorana 3 (Figure 2.5[Left]). On the second process, we invert the order, hence exchanging first exchange Majoranas 2 and 3 and then Majoranas 1 and 2 (Figure 2.5[Right]). These two cases are represented by the following operators respectively

$$\begin{aligned} U_{23}U_{12} &= \frac{1}{2}(1 + \gamma_2\gamma_3)(1 + \gamma_1\gamma_2) = \frac{1}{2}(1 + \gamma_2\gamma_3 + \gamma_1\gamma_2 + \gamma_3\gamma_1) \\ U_{12}U_{23} &= \frac{1}{2}(1 + \gamma_1\gamma_2)(1 + \gamma_2\gamma_3) = \frac{1}{2}(1 + \gamma_1\gamma_2 + \gamma_2\gamma_3 + \gamma_1\gamma_3). \end{aligned} \quad (2.17)$$

Since $\gamma_3\gamma_1 = -\gamma_1\gamma_3$, the outcome of both processes is essentially different, which means that it actually matters the order in which the Majoranas are exchanged .

The particles that satisfy this strange property receive the name of non-abelian anyons. While the word "anyon" usually integrates several types of particles including bosons and fermions, the word non-abelian makes emphasis on those anyons with non-commutative exchange statistics.

Non-abelian statistics is what make anyons a fantastic candidate to implement quantum algorithms. The idea of exchanging anyons can be thought as a braiding code like in Figure 2.5. Since the order of braiding matters, different braiding orders can be associated to distinct algorithms. This generates another form of codifying information which has been extensively studied in knot theory [17]. And if these anyons were topological, they will be protected from quantum decoherence [28]. To the date, the closest candidates to satisfy both properties (non-abelian statistics and topological characterization) are the Majorana fermions. Nonetheless, the basic braiding protocol that would unleash the keys to topological quantum computation [16] has not been measured yet. Many theoretical proposals have been set up in this direction, but there is still a long experimental road.

2.1.3 Real implementations of the Kitaev Chain

One of the main problems to implement real devices capable to exhibit Majorana quasi-particles at the boundaries, is that Majorana's are spin-less. Since all materials have fermion doubling, it was necessary to endow the system with a physical property that could separate the spin energy bands. To bypass this problem, Lutchyn et al. proposed using a material with strong spin-orbit Rashba interaction [29] and applying a magnetic field. This would split the energy band by spin, hence destroying fermion doubling.

This idea allowed scientists to designed the first Majorana wires. The recipe consists in-growing a semi-conducting wire with high spin-orbit coupling, over an s'wave superconductor and inducing a Zeeman magnetic field (Figure 2.6(a)). Such model is described by a Hamiltonian of the form [2](65)

$$H = H_{\text{wire}} + H_{\delta} \quad (2.18)$$

with

$$H_{\text{wire}} = \sum_{\sigma \in \{\uparrow, \downarrow\}} \int dx \psi_{\sigma}^{\dagger}(x) \left(\frac{-1}{2m} \partial_x^2 - \mu - i\alpha \sigma_y \partial_x + h \sigma_x \right) \psi_{\sigma}(x), \quad (2.19)$$

$$H_{\Delta} = \int dx \Delta \psi_{\downarrow} \psi_{\uparrow} + \Delta^* \psi_{\downarrow} \psi_{\uparrow}. \quad (2.20)$$

Where $\psi_{\sigma}^{\dagger}(x)$ creates a particle at x with spin σ , μ is the chemical potential, h is the Zeeman splitting energy and $\alpha > 0$ is the Rashba spin-coupling parameter, favoring spin-align. The induced superconducting proximity is depicted by H_{Δ} where Δ is the superconducting gap. Note that this system (2.18) has all the ingredients of the Kitaev chain.

If $\Delta = 0$, the Bloch Hamiltonian is given by

$$\mathcal{H}_k = \frac{k^2}{2m} - \mu + k\alpha \sigma_y + h \sigma_x. \quad (2.21)$$

And diagonalizing this matrix we obtain that the band splits as

$$\varepsilon_{\pm}(k) = \frac{k^2}{2m} - \mu \pm \sqrt{(\alpha k)^2 + h^2} \quad (2.22)$$

with opposed spins as observed in the blue and red lines of Figure 2.6(b).

The superconducting proximity effect ($\Delta > 0$) opens a gap that projects the upper and lower bands forming the black bands of Figure 2.6(b). This separation of both energy channels allows us to think the conduction band as an spin-less. This system enters into the topological phase when

$$h > \sqrt{\Delta^2 + \mu^2}. \quad (2.23)$$

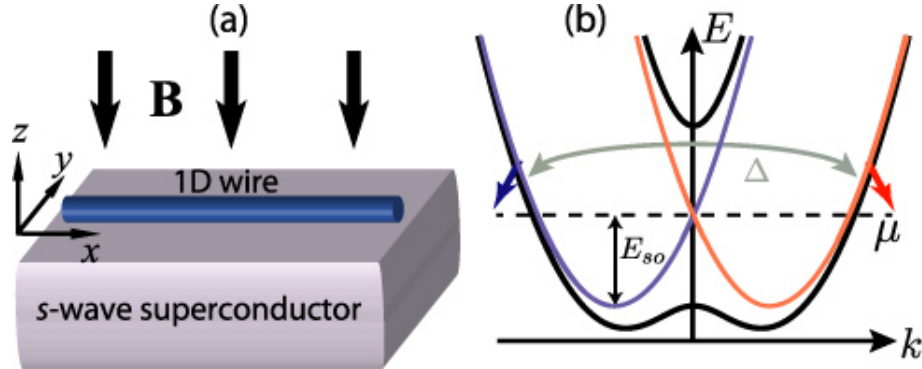


Figure 2.6: (a) Setup of a Majorana wire with high spin-orbit coupling, over a superconducting plane and an induced Zeeman field. (b) Splitting of the energy bands with different spins in the non-superconducting regime (red and yellow bands). With superconducting proximity , a gap is opened and the red and blue energy bands are projected forming the black bands. *Adapted from [2]*

At these points, Majorana bound states emerge at the edges of the wire.

This theoretical proposal led in 2012 to the first observation of Majorana signatures in InSb nanowires ³, by Mourik et al. from the Kavli Institute at Delft. This was a huge boost to the field which immediately attracted abundant experimental and theoretical work.

In just 6 years, more than 5 groups have documented the observation of Majorana signatures [3, 22–24, 30]. This signature is characterized by the emergence of a robust zero bias conductance peak ZBCP of height $\frac{2e^2}{h}$ produced by the Majorana zero mode MZM localized at the edges of the wire. Though the first experiments didn't observe such a stable signature, the last year Zhang et al. published a paper documenting the observation of this robust peak with the expected theoretical magnitude in an InSb wire Figure 2.7. As can be observed in Figure 2.7(b) the ZBCP increases up to $\frac{2e^2}{h}$ for a strong magnetic field, where the system enters the topological phase according to equation (2.23).

Despite the successful experimental results, there is still certain skepticism about the existence of Majorana fermions, mainly because Majorana zero-modes (MZM) have been found in superposition with similar types of phenomena that produce zero-modes. Some examples of these are the Andreev reflection [31] or even the Kondo peak [32]. New experimental proposals focus on distinguishing MZMs from these effects and implementing braiding protocols [33–35]. One promising idea that could lead to important results in both research lines is coupling Majorana wires with QDs. This will be the objective of the following section.

³A material with strong spin-orbit coupling and large g factor.

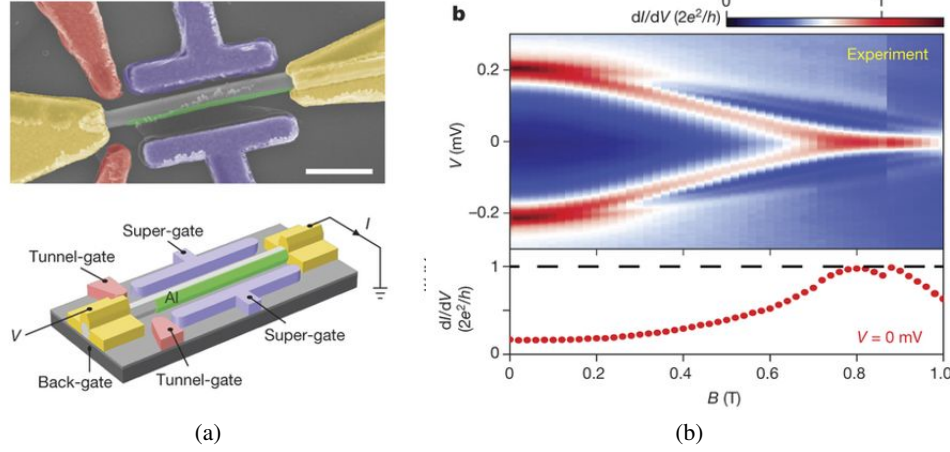


Figure 2.7: (a) Experimental setup (b) Observed magnetic field dependence of the zero bias peak. [3]

2.2 Detecting Majorana zero modes using quantum dots

Liu and Baranger were the first to propose in 2011 the possibility of using QDs to detect Majorana zero modes [36]. When a QD is attached to the end of a Majorana chain in the topological phase, the Majorana Zero Mode at the end of the chain leaks inside the QD [37] producing a zero-bias conductance peak of half a quanta $\frac{e^2}{2h}$ through the dot. This method of detecting Majorana signatures presents important advantages:

- 1. It does not destroy the entire qubit information:** Other detection methods such as tunneling spectroscopy have the downside that it probes not only the end of the Topological Superconductor(TS), but its bulk as well. This completely destroys the qubit information. When attaching the Majorana chain to a QD it is the conductivity is measured through the QD which does not disturb the bulk of the chain.
- 2. Kondo-Majorana physics:** The observation of Kondo signatures in superconducting devices [38] and the similarities between Kondo and Majorana signatures [37] motivated to study the existence of prospective Kondo-Majorana physics [32, 39]. These two effects could co-exist at temperatures of a few mili-kelvins in quantum impurity systems.

Quantum dots (QD) are artificial and adaptable quantum impurities, which makes them the best device to perform this kind of study. In particular, a QD-Majorana system was already studied by my advisor in a previous paper [1], where he proofed that it is possible separate Kondo and Majorana physics by tuning dot's gate voltage or by applying a strong magnetic field.

3. **Manipulation of Majorana zero modes:** Today's precise experimental control over QDs makes us dream with the possibility of implementing scalable braiding proposals Figure 2.8(a) and quantum architectures for topological quantum computation Figure 2.8(b).

These architectures perform adiabatic evolutions similar to the ones described in subsection 2.1.2 to braid Majorana fermions. This operation strongly relies on the possibility of manipulating the Majorana zero modes inside the dots. The main idea of MZM manipulation is to tune the gate voltage of one dot to induce the Majoranas to "move" into the other dots. In a prospective braiding protocol, as the one described in [4] (Figure 2.8(a)), this manipulation process would have to be performed several times. However, till this moment MZM manipulation hasn't been achieved experimentally.

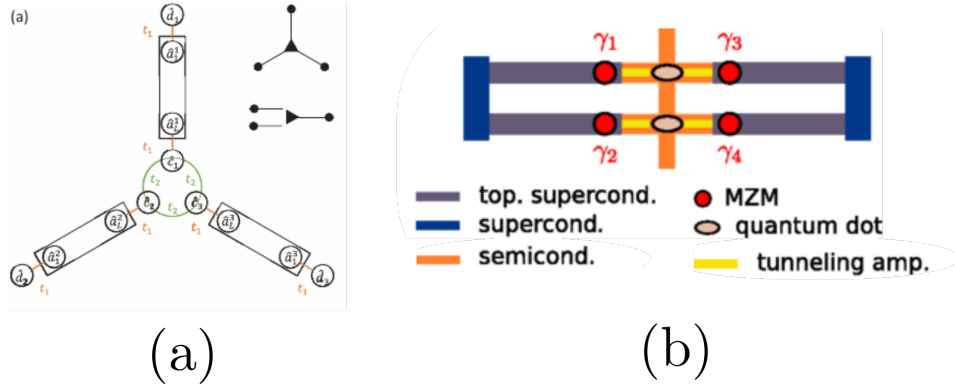


Figure 2.8: a) Braiding proposal b) Basic architecture with four Majorana Zero Modes in a scalable quantum computer. Adapted from (a) [4] (b) [5].

Nonetheless, the future for this area is still very promising. Recent experiments have documented the observation of Majorana signatures in Majorana-QD devices [24] and Andreev molecules in topological superconductors attached to double quantum dots [40]. The next steps are clearly directed to achieve Majorana manipulation.

2.2.1 Why double quantum dots?

The simplest case where Majorana manipulation is possible is in a double quantum dot (DQD). Tunneling Majorana modes in these basic structures have inspired theoretical studies [41, 42] and experimental setups confirming the observations of Andreev molecules [40]. Even though quantum tunneling of a MZM into a double dot shows several possibilities for manipulation of MZM, there is still no complete analysis of the transitions of the Majorana signatures between the QDs in this model.

In this thesis we fill this gap by performing a transport study of a DQD attached to a MZM and a metallic lead. The simplicity of this model allows us to explore analytically different configurations of QD's from symmetric and linear couplings to T-junctions . We considered both non-interacting and interacting regimes, observing major agreement between both approaches about the location of the Majorana signature. While the non-interacting regime is suitable to obtain exact expressions for the Green function, the interacting case shows how the Majorana signature co-exists with strongly correlated phenomena such as the Kondo effect and RKKY interactions [43–45].

2.3 Overview

This thesis is integrated by 4-major chapters:

- In chapter 3, we will take a review to the basis of quantum transport in single electron transistors, the Anderson model and the emergence of the Kondo effect in quantum dots.
- In chapter 4 we provide a description of the methods that we will use to study the Double Quantum Dot-Majorana system. To study non-interacting systems we will use the Zubarev's ballistic transport[46] which is optimized through the Graph-Gauss-Jordan elimination algorithm define in subsection 4.1.2. For non-interacting systems we use Wilson's Numerical Renormalization Group (NRG) technique [47]. We will test our methods in a double quantum dot attached to a magnetic field. Hence, background information about double quantum dots systems will be presented in this chapter.
- In chapter 5 We will test our methods in the QD-Majorana system, confirming the results of previous papers [36, 48] .
- The chapter 6 contains our major contributions to this area. Using the methods from chapter 4 and the previous acquired experience with the double quantum dot and the QD-Majorana model , we study in a double quantum dot attached to a Majorana zero mode and a metallic lead. We will characterize in this simple model the transitions of the Majorana signature for distinct configurations of the dots. The final results are now part of a paper that we hope to submit for publication in the following months.

Chapter 3

Preliminaries

In this preliminary chapter we will give a brief description about transport processes in quantum dots (QDs). We will discuss basic aspects about single electron transistors, the application of the Anderson impurity model in QDs and the subsequent emergence of the Kondo effect, one of the main condensed matter problems of the 20th-century.

3.1 Transport process in quantum dots (QDs)

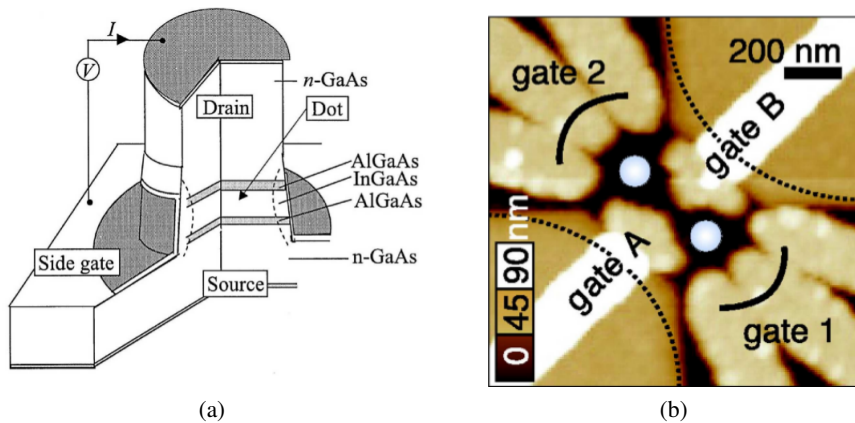


Figure 3.1: a) Vertical quantum dot. b) Atomic force microscopy picture of two coupled lateral QDs (bright central circles). Gates 1 and 2 act as drain and source voltage. A negative voltage is applied at gates A,B to allow the formation of the droplets inside the free space in the 2D electron gas. Adapted from [6]

Quantum mechanical effects are visible when the system size is of the order of the de Broglie wavelength [49, (1.1)]

$$\lambda_f = \frac{h}{\sqrt{3m_{\text{eff}}k_B T}}$$

where m_{eff} is the electron effective mass in the crystal. Since m_{eff} can be much smaller than the free electron mass in some semiconducting materials, size quantization effects can be observed

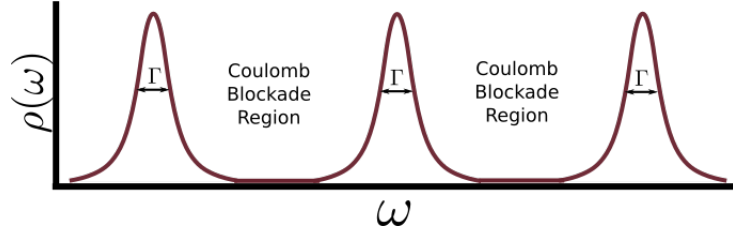


Figure 3.2: Representation of the Density of States of a QD. The gate potential V_G can be tuned to change the fermi energy of the dot.

at system of sizes $\sim 100\text{nm}$ [7]. A 0D quantum system is a device confined in the three spacial dimensions up to this length-scale. This type of device receive the name of quantum dot (QD).

Nowadays, QDs can be manufactured in different substracts, geometries and orientations [49]. They can be integrated in structures like double quantum dots (Figure 3.1(a)) or can even be grown vertical to the based 2D-electron gas (Figure 3.1(b)). The precise experimental control over these devices allows to design atom-like structures with tunable energy levels. This has important applications on laser physics and in the implementation of single electron transistors.

Ideally, the energy spectrum of a QD is a discrete set of energy levels resembling the spectrum of an atom. This atom-like structure is usually connected to three main gates (See Figure 3.3(a)). Two of them are the source and the drain with voltages V_S and V_D , used to control the electric gradient through the QD. When the QD is connected to these leads these energy levels are hybridized with respect to a broadening parameter Γ which increases as the square of the source-drain voltage V_{SD}

$$\Gamma \propto \pi \|V_{SD}\|^2 \quad (3.1)$$

This broadening is depicted in Figure 3.2. Ideally, $\Gamma \ll \Delta E$ is smaller enough such that the energy levels do not overlap each other.

The third gate is the gate voltage V_G which allows to tune the energy levels of the dot with high precision. With this three gates it is possible to execute transport measurements through a QD. An electron can pass from the source to the drain if there is an energy level in the middle of the two voltages, just as in Figure 3.3(a). If this condition is not satisfied, the dot enters into a coulomb blockade region without electron transport between both leads as can be observed in Figure 3.3(b)). Inside the coulomb blockade regions (black diamonds) the number of electrons is constant. When increasing V_G a single electron enters into the dot each time the system makes a transition between blockade regions. Since all of these effects can be controlled precisely with the gate voltage, the system described is indeed a single electron transistor (SET).

Note that when $V_{SD} = 0$, the condition for conductance can still be satisfied if there is an hybridized state at the level of $V_S = V_D$, the Fermi energy. This situation receives the name of zero-bias conductance peak (ZBCP). The effects that can cause robust ZBCPs are quite interesting. In this thesis we will study two of them. The Kondo effect and the Majorana zero

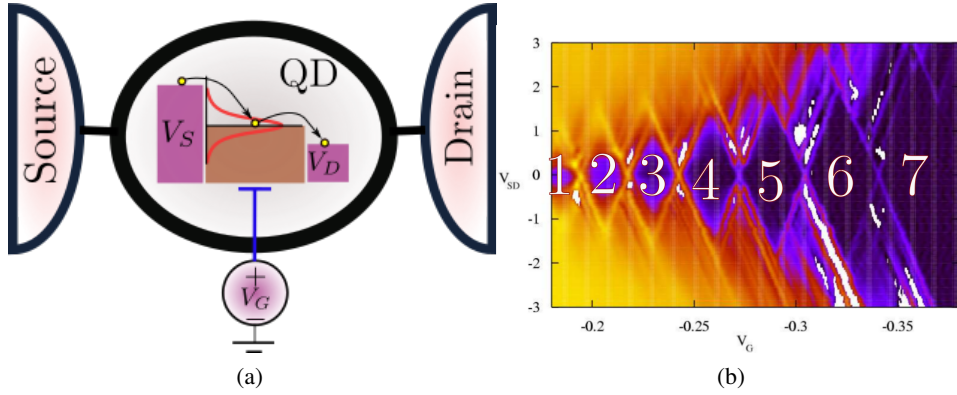


Figure 3.3: (a) Representation of transport through QD. The red curve represents the hybridized energy level. The gate voltage tunes this level. In the case represented, the energy level is in the middle of the drain and source voltages allowing transport between the leads. (b) Charging diagram of a quantum dot. Differential conductance dependence over the gate voltage V_G and the source-drain voltage ($V_{SD} = V_S - V_D$). Coulomb blockade occurs at the diamond-shaped regions with zero conductance. At these regions the number of electrons is constant and increases 1 by 1 when the gate voltage is scaled up. (b) Adapted from [7]

modes.

3.2 The Anderson Model

The Anderson model is used to describe quantum impurity systems [50]. A quantum dot attached to a metallic lead is basically an artificial impurity that can be experimentally designed, modified and manipulated. Hence QDs are the perfect type of structure to test the Anderson mode.

Due to the small confinement space inside these dots, coulomb repulsion is relevant. However, it is usually impossible to provide a complete analytical description of these kind of systems due to the high correlations generated by this factor. Instead, we can obtain an overall description of the transport through the impurity by neglecting this coulomb repulsion. This will allow us to obtain some analytic intuition of the models before adventuring with long-lasting numerical simulations of interacting models. During this thesis, we will consider these two regimes as follows

- **Non-interacting systems:** Coulomb repulsion is not relevant . In this case, spin- \uparrow and spin- \downarrow channels are independent. They can be solved analytically through the equations of motion (section 4.1).
- **Interacting systems:** The coulomb repulsion is relevant. The repulsion factor will be defined by the factor U which will take a fix value during the entire project. In this case,

3.2. The Anderson Model

spin- \uparrow and spin- \downarrow channels are not independent since the coulomb repulsion limits the number of particles inside each dot. We will use the Numerical Renormalization Group to treat this case. The intuition acquired from non-interacting systems will help us to select the input parameters of the algorithm.

To begin the description of the Anderson model, first consider that we have a QD (impurity) coupled to the conduction band of a metallic lead. We will define a coulomb repulsion factor U_i , which will be set to 0 if the system is non-interacting. Using the Hunds rules, we know that the energy levels inside the dot should be filled from lower to higher energies with two electrons with different spin at each state. Each pair of electrons will interact magnetically and electrically. In addition, there is an energy term associated to each electron and a Zeeman splitting factor in case a \hat{z} -directed magnetic field B is placed. Considering these interactions, we can obtain a very general expression in second quantization for the QD Hamiltonian of the form [7, (3.2)]

$$H_d = \sum_{i\sigma} \varepsilon_i d_{i\sigma}^\dagger d_{i\sigma} + \sum_i U_i \hat{n}_{i\uparrow} \hat{n}_{i\downarrow} + \sum_{\sigma\sigma', i \neq j} U_{ij} \hat{n}_{i\sigma} \hat{n}_{j\sigma'} - \mu_B g B \sum_i S_i^z + J \sum_{i \neq j} \mathbf{S}_i \cdot \mathbf{S}_j. \quad (3.2)$$

Where $\sigma \in \{\uparrow, \downarrow\}$, $d_{i\sigma}^\dagger$ ($d_{i\sigma}$) is the dot creation(annihilation) operator, $\hat{n}_{i\sigma} := d_{i\sigma}^\dagger d_{i\sigma}$ is the particle number, \mathbf{S}_i is the spin-vector, ε_i is the energy of the i^{th} -level in the dot, U_i is the coulomb repulsion between electrons in the same energy level i , U_{ij} is the coulomb interaction between electrons in different levels (And therefore smaller than U_i), B is an applied magnetic field in the \hat{z} -direction and J is the term representing the Zeeman splitting.

At low temperatures, the quantum interactions occur only with the level closest to the Fermi energy. Hence, we can make a single-level approximation, neglecting the other energy levels. This assumption reduces the complexity of the dot Hamiltonian to

$$H_d = \sum_{\sigma} \varepsilon d_{\sigma}^\dagger d_{\sigma} + U \hat{n}_{\uparrow} \hat{n}_{\downarrow} - \mu_B g B S^z. \quad (3.3)$$

Besides to the dot Hamiltonian, we need to consider the energy of the electrons in the lead H_{lead} and the dot-lead interaction H_{int} . We can model the conduction band of the lead as an electron gas with the following Bloch Hamiltonian

$$H_{\text{lead}} = \sum_{\mathbf{k}\sigma l} \varepsilon_{\mathbf{k}l} c_{\mathbf{k}\sigma l}^\dagger c_{\mathbf{k}\sigma l}. \quad (3.4)$$

where \mathbf{k} represents the possible crystal momentums in the leads, $l \in \{S, D\}$, $c_{\mathbf{k}\sigma l}^\dagger$ ($c_{\mathbf{k}\sigma l}$) creates(annihilates) an electron with momentum \mathbf{k} and spin σ in the lead l , $\varepsilon_{\mathbf{k}l}$ is the energy of the electron in the leads.

On the other hand, the interaction between the dot and the leads is then given by

$$H_{\text{int}} = \sum_{\mathbf{k}\sigma l} V_{\mathbf{k}l} c_{\mathbf{k}\sigma l}^\dagger d_{\sigma} + V_{\mathbf{k}l}^* d_{\sigma}^\dagger c_{\mathbf{k}\sigma l}, \quad (3.5)$$

3.3. The Kondo Effect

where V_{kl} is a hopping exchange term between the leads and the QD.

The sum of these three interactions receives the name of Anderson Model.

$$\begin{aligned} H &= H_d + H_{lead} + H_{int} \\ &= \sum_{\sigma} \varepsilon d_{\sigma}^{\dagger} d_{\sigma} + U \hat{n}_{\uparrow} \hat{n}_{\downarrow} - \mu_B g B S^z + \sum_{k\sigma l} \varepsilon_{kl} c_{k\sigma l}^{\dagger} c_{k\sigma l} + \sum_{k\sigma l} V_{kl} c_{k\sigma l}^{\dagger} d_{\sigma} + V_{kl}^* d_{\sigma}^{\dagger} c_{k\sigma l}. \end{aligned} \quad (3.6)$$

In this project, we will make two extra modifications to this system. Using the anti-commutation properties of the fermion operators

$$\{d_{\sigma}^{\dagger}, d_{\sigma'}\} = \delta_{\sigma\sigma'}, \quad \{d_{\sigma}^{\dagger}, d_{\sigma'}^{\dagger}\} = \{d_{\sigma}, d_{\sigma'}\} = 0$$

we get

$$\begin{aligned} (d_{\uparrow}^{\dagger} d_{\uparrow} + d_{\downarrow}^{\dagger} d_{\downarrow} - 1)^2 &= \sum_{\sigma} (d_{\sigma}^{\dagger} d_{\sigma})^2 - 2 \sum_{\sigma} d_{\sigma}^{\dagger} d_{\sigma} + 2 d_{\uparrow}^{\dagger} d_{\uparrow} d_{\downarrow}^{\dagger} d_{\downarrow} - 1 \\ &= 2 d_{\uparrow}^{\dagger} d_{\uparrow} d_{\downarrow}^{\dagger} d_{\downarrow} - \sum_{\sigma} d_{\sigma}^{\dagger} d_{\sigma} - 1. \end{aligned}$$

And replacing this in (3.3) we obtain a nice spin-symmetric form of the dot hamiltonian

$$\left(\varepsilon + \frac{U}{2} \right) d_{\sigma}^{\dagger} d_{\sigma} + \frac{U}{2} (d_{\sigma}^{\dagger} d_{\sigma} - 1)^2 - \mu_B g B S^z. \quad (3.7)$$

In addition, it is possible to do a linear transform to the lead operators

$$\frac{1}{\sqrt{V_S^2 + V_R^2}} \begin{bmatrix} V_S & V_R \\ -V_R & V_S \end{bmatrix} \begin{bmatrix} c_{k\sigma S} \\ c_{k\sigma D} \end{bmatrix} = \begin{bmatrix} c_{k\sigma+} \\ c_{k\sigma-} \end{bmatrix} \quad (3.8)$$

After this transformation the operator will be decoupled from the dot hamiltonian $c_{k\sigma-}$. This implies that we can suppose that the dot is coupled with just one lead. In the following chapters we will maintain this convention.

3.3 The Kondo Effect

The Kondo effect is one of the biggest condensed matter problems in the 20th century. There was an uncountable number of experimental and theoretical physicist that contributed to this problem. The most reknown are probably the physicists Jacques Friedel, Jun Kondo and the two nobel prizes Philip Anderson and Kenneth Wilson [51].

The history of the Kondo effect began in the early 1930s. By that time it was known that the resistivity of a metal is regulated by different scattering interactions against lattice phonon vibrations $\rho_{phonon} \sim T^5$, other electrons $\sim T^2$ and static impurities, which is temperature independent. The form of these contribution clearly implies that the resistivity should decay

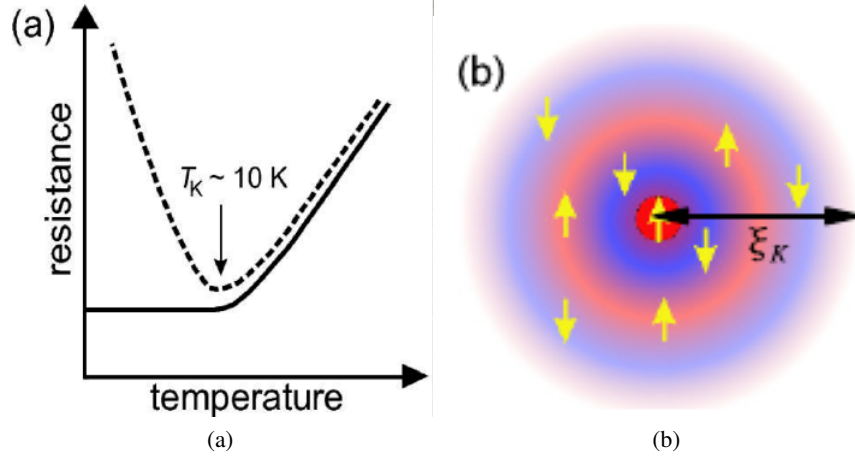


Figure 3.4: (a) Resistivity minimum near the Kondo temperature T_K . (b) Kondo cloud formed by a singlet grouped around the impurity divided in spin- \uparrow , spin- \downarrow regions. Adapted from a) [8], b) [9]

uniformly with a decreasing temperature. Nevertheless, some groundbreaking experiments revealed the observation of a resistance minimum in some metals at temperatures lower than 10K [8](See Figure 3.4 (a)).

This phenomenon intrigued the scientific community for the following decades until the year 1964 when the physicist Jun Kondo gave the first convincing solution to this puzzle. Kondo attributed the phenomenon to the scattering of the electrons due to the spin-interaction with a small concentration of magnetic impurities in the metal. To describe it he proposed the following interaction Hamiltonian

$$H_K = 2J\hat{\mathbf{S}} \cdot \hat{\mathbf{s}} \quad (3.9)$$

$$= J(2S_zs_z + S_+s_- + S_-s_+) \quad (3.10)$$

with $S_{\pm} = S_x \pm iS_y$. The hamiltonian H_K which is better known as the Kondo s-d model describes the spin interaction between the spin of the impurity $\hat{\mathbf{S}}$ and the spin of the particles in the metal $\hat{\mathbf{s}}$.

Kondo took H_K as a perturbation of the electron gas in the metallic lead, with J the perturbation parameter. While the first order led to no important contribution, Kondo was able to obtain on second order perturbation theory a logarithmic correction on the temperature in the resistivity of the form

$$\rho_{imp} \propto \ln \frac{T_K}{T}, \quad (3.11)$$

3.3. The Kondo Effect

where T_K received the name of Kondo temperature. Summing up this term to the other resistivity contributions we obtain the full expression

$$\rho_{metal}(T) = \rho_{imp} + a_e T^2 + b_{Phonon} T^5 + c_m \ln \frac{T_K}{T}. \quad (3.12)$$

When $T < T_K$ the term $\ln \frac{T_K}{T}$ increases. Eventually, it compensates the decaying resistivity which finally explained the resistance minimum.

Although Kondo's explanation was initially very successful it also presented a troublesome outcome. The logarithmic term introduced by Kondo diverges when the temperature approximates to 0, hence proving to be inefficient at temperatures well below T_K . Going to the following orders in perturbation theory also led to divergent contributions to the resistivity. This led physicists to explore non-perturbative approaches to solve the Kondo effect.

By that time, Anderson had already created his famous impurity model. One of his main contributions was the inclusion of the Hubbard term to represent the Coulomb interaction inside the dot, which proved to be fundamental to understand the Kondo effect. Nonetheless, the Anderson model was a huge numerical challenge. The problem was finally solved by Kenneth Wilson, who was able to effectively diagonalize the Anderson model using a numerical method that combines ideas from scalability and the renormalization group.

Wilson's explanation solved the Kondo problem almost completely. It turned out that below the Kondo temperature, which is around

$$K_B T_K = \frac{1}{2} \sqrt{U\Gamma} e^{\varepsilon(\varepsilon+U)/\Gamma U} [7], \quad (3.13)$$

the impurity entangles with the low-energy electrons forming a strongly correlated many-body singlet. This singlet surrounds the impurity in a structure formed by alternating regions of spin- \uparrow and spin- \downarrow particles called the Kondo cloud (See Figure 3.4(b)). The Kondo cloud was the first evidence of an entangled many body state, and is predicted to have an astonishing correlation length between $0.1\mu m$ to $10\mu m$. This is a huge number if we think that the impurity(or QD) can have a radius below $1nm$. Finally, the minimum in the resistivity is produced when the conduction electrons scatter with the Kondo cloud.

3.3.1 Kondo Effect in QDs

The problem of magnetic impurities in metals can be treated using the Anderson model in a similar form as the transport in quantum dots. Hence, it is not a surprise that the Kondo Effect could also occur these systems. In 1998 the technological advances allowed the observation of the Kondo effect for the first time in a single electro transistor [52]. When an odd number of electrons is in the QD the last level bellow the Fermi energy is half-occupied, so that the dot can be considered as a magnetic impurity. The unlocalized electrons in the reservoirs then interact with this localized electron. Spin-exchange can occur as it happened with magnetic impurities

3.3. The Kondo Effect

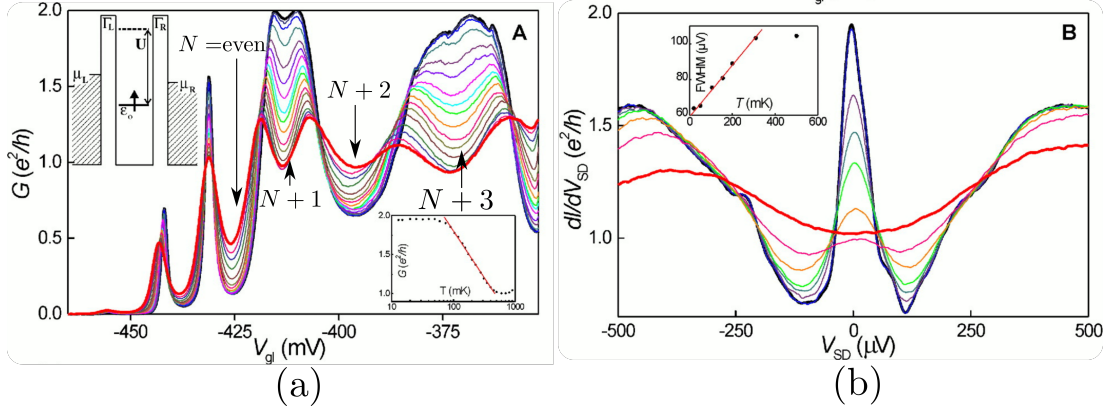


Figure 3.5: Observation of the Kondo effect in a single electron transistor. Color scale temperatures from 15mK (Black) to 800mK(Red) a) Dependence of the zero bias conductance over the gate voltage. A plato in the conductance peak appears in the odd particle regimes. b) Dependence of the conductance over the gate source drain voltage inside an odd electron regime. A zero bias conductance peak (ZBCP) of height $\frac{2e^2}{h}$ is observed. This is the Kondo signature. Adapted from [10]

in metals. At low temperatures, this magnetic interaction gives rise to strong quantum correlations that favor the formation of a singlet state between the localized electron and the electrons in the leads. As a result, the zero-bias density of states is increased producing a zero-bias conductance peak Figure 3.5(b).

Note that the physical implications of the Kondo effect are different in magnetic impurities in metals and in QDs. In fact, they are complete opposite. While in magnetic impurities the resistivity increase, the Kondo effect in QD's leads no an unexpected raised in the zero-bias conductivity. The reason for this disagreement between both situations are the system dimensions. The scattering against a Kondo singlet in a 3D or 2D systems against magnetic impurities is an obstacle to the conducting electrons. Instead, scattering in 1D-devices enhances the conductivity of the QD because there is only one scattering direction.

As we previously discussed in section 3.1, zero-bias transport in quantum dots can only occur if there is a state at the Fermi energy. The Kondo effect creates a zero bias peak that is present whenever the dot has odd electrons . This explains the zero-bias platoes observed in Figure 3.5(a). We may think that the new singlet at the Fermi energy is creating a "channel" that allows quantum transport between both sides of the dot. This explains the Kondo peak.

In the following chapters we will give more details about this zero-energy-mode and theory that explained it: The numerical renormalization group.

Chapter 4

Theory and Methods

The density of states contains important physical information about the presence of zero-modes which can be caused by the Kondo effect or by a Majorana quasi-particle. Studying this quantity will allow us to observe both effects separately inside each quantum dots. In this chapter we describe the two methods that we will use during the entire project to compute the DOS:

- The first method uses Zubarev's Green function formalism [46]. This approach requires the solution of the equations of motion, a process that we simplify introducing the graph-Gauss-Jordan elimination method (subsection 4.1.2). In the non-interacting regime, this method allows us to obtain an exact analytical expression of this quantity for density of states of the system.
- Interacting systems are more complex and cannot be solved analytically. Instead, we appeal to the renown numerical renormalization group (NRG) to deal with the strong correlations of the interacting Anderson model section 4.2. The NRG is famous for providing the most complete explanation of the Kondo effect. Now we intend to use it to study the co-existence of Kondo and Majorana physics.

Both methods will be tested on the model of a double quantum dot attached to a metallic lead. We will observe that at very low energies, the physics of interacting systems emulate characteristic features of the non-interacting model. The methods developed in this chapter will be tested again in chapter 5 for a QD coupled to a Majorana chain. Finally we will use them to make our leading contribution to this theory, the analysis of a double quantum dot attached to a Majorana wire (chapter 6).

4.1 Green function formalism

The Green function G of a Hamiltonian H is the operator that satisfies the homogeneous equation

$$\left(i\hbar \frac{\partial}{\partial t} - H \right) G(t-t') = \delta(t-t'). \quad (4.1)$$

This type of differential equations are usually solved with a Fourier transform

$$G_H(\omega) = \int_{-\infty}^{\infty} d(t-t') G(t-t') e^{-i\omega(t-t')}. \quad (4.2)$$

By convention we took $\hbar = 1$ so that we can unify units of frequency and energy. This turns equation (4.1) into a function of the energy ω such that

$$(\omega + is - H)G_H(\omega) = I. \quad (4.3)$$

The term $+is$ in the previous Hamiltonian is part of a mathematical trick quite common in this theory. During the whole procedure, the Green function acts on the complex field, with $+is$ making reference to a small imaginary part that allows to avoid singularities in the real line. But when we need to obtain a physical interpretation, we will take the limit $s \rightarrow 0$ to obtain the result for real energies.

The next step is to decompose $G_H(\omega)$ in the eigenbase of the Hamiltonian $\{|\alpha\rangle\}$ by

$$\langle \alpha | G_H(\omega) | \alpha' \rangle = \frac{\delta_{\alpha\alpha'}}{\omega - is - \varepsilon_\alpha} = \frac{\delta_{\alpha\alpha'}(\omega + is - \varepsilon_\alpha)}{(\omega - \varepsilon_\alpha)^2 + s^2}. \quad (4.4)$$

From the Cauchy relation

$$\lim_{s \rightarrow 0} \frac{s}{(\omega - \varepsilon_\alpha)^2 + s^2} = \pi \delta(\omega - \varepsilon_\alpha) \quad (4.5)$$

we obtain

$$Im[\langle \alpha | G_H(\omega) | \alpha' \rangle] = \pi \delta(\omega - \varepsilon_\alpha) \delta_{\alpha,\alpha'}. \quad (4.6)$$

Note that the sum of $Im[\langle \alpha | G_H(\omega) | \alpha' \rangle]$ over all the eigenstates of H is simply π times the density of states:

$$\rho(\omega) = -\frac{1}{\pi} \sum_{\alpha} Im[\langle \alpha | G_H(\omega) | \alpha' \rangle] = \sum_{\alpha} \delta(\omega - \varepsilon_{\alpha}). \quad (4.7)$$

4.1.1 Green function of fermion operators and the equations of motion

In many body physics, fermion operators are defined by quantized fields over time satisfying anti-commutation relations, such that for any two independent operators at a time t ($A(t), B(t)$) we have

$$\{A(t), B(t)\} = \delta_{B,A^\dagger}. \quad (4.8)$$

Two types of Green functions are usually defined in this case.

$$G_{A,B}^r(t, t') = -i\theta(t - t') \langle \{A(t), B(t')\} \rangle. \quad (4.9)$$

$$G_{A,B}^a(t, t') = -i\theta(t' - t) \langle \{A(t), B(t')\} \rangle. \quad (4.10)$$

Where $\theta(t - t')$ is the Heaviside step function and the brackets $\langle \rangle$ refer to the statistical mean over thermal states. $G_{A,B}^r$ is called the retarded Green function. It is non-zero only if $t > t'$, such

it allows to compute the response of the system after it has been perturbed. The advanced Green function $G_{A,B}^a$ is the adjoint of $G_{A,B}^r$ and represents exactly the opposite regime.

Usually we can obtain all relevant physical properties just with the retarded Green function, including the density of states. To perform this, we need to take first the Fourier transform of the retarded green function to enter into the energy domain

$$G_{A,B}(\omega) = \int_{-\infty}^{\infty} d(t-t') G_{A,B}^r(t,t') e^{-i\omega(t-t')} . \quad (4.11)$$

Now, in this formalism, the DOS is associated to a fermion operator A . Similar to (4.7), it can be computed as

$$\rho_{A,A^\dagger} = -\frac{1}{\pi} \text{Im} [G_{A,A^\dagger}(\omega)] . \quad (4.12)$$

The density of states contains important physical information related to operator A . In our case, operator A^\dagger will be related to the dot's creation operator d^\dagger . Therefore, computing (4.12) will allow us to observe the hybridization of the dot's discrete states and the creation of other energy levels due to the interaction with the lead and other impurities. In particular, we are interested in studying the zero-modes of the system which are the main signatures of Kondo and Majorana physics.

But before talking more about the DOS, we still need an efficient method to compute the Green function of the system. We can achieve this by analyzing the evolution of the retarded Green function in the time domain. This is determined by Schroedinger's differential equation in the Heisenberg picture

$$i \frac{dA(t)}{dt} = [A(t), H] , \quad (4.13)$$

which allows us to derive

$$i \frac{d}{dt} G_{A,B}^r(t,t') = -i^2 \langle [A(t), B(t)] \rangle \delta(t-t') - i\theta(t-t') \left\langle \left\{ i \frac{dA(t)}{dt}, B(t') \right\} \right\rangle \quad (4.14)$$

$$= \delta_{A^\dagger, B} \delta(t-t') - i\theta(t-t') \langle \{[A(t), H], B(t')\} \rangle \quad (4.15)$$

$$= \delta_{A^\dagger, B} \delta(t-t') + G_{[A,H'],B}^r(t,t') . \quad (4.16)$$

When taking the Fourier transform of (4.16) we obtain the following equation in the energy domain

$$\omega G_{A,B}(\omega) = \delta_{A^\dagger, B} + G_{[A,H'],B}(\omega) . \quad (4.17)$$

In a set of operators $\{A_1, A_2, \dots\}$ (4.17) defines a system of transport equations describing the flow of state transitions of the operators in our model. This system receives the name of equations of motion. In this thesis we will identify each set of equations with a flow graph. This will be our leading method to compute the green functions of the system.

4.1.2 Graph-Gauss-Jordan elimination process: Solving the equations of motion

Solving the transport equations involves dealing with a set of linear equations where all the possible variables including ω , and the Hamiltonian parameters are assumed to be constant. This can be done by Gauss-Jordan elimination, noting that after each elimination process we need to carry on the account in terms of the initial variables. The solution will be a polynomial fraction. When the number of operators in the Hamiltonian increases the number of terms in the polynomial grows-up rapidly according to the number of initial parameters. This reveals the importance of exploring new methods that could simplify the solution of this system, and present a readable factorized expression of the final solution.

The method presented here uses graph theory algorithms that provide a shortcut to Gauss-Jordan elimination [53]. We will explain this method by solving the transport equations for a non-interacting ($U = 0$) DQD connected to one lead.

According to the Anderson model the Hamiltonian for this system looks like

$$H = \sum_{i=1}^2 \epsilon_i d_i^\dagger d_i + t_{dots} d_1^\dagger d_2 + t_{dots}^* d_2^\dagger d_1 + \sum_k \left(V_i d_i^\dagger c_k + V_i^* c_k^\dagger d_i \right) + \epsilon_k c_k^\dagger c_k. \quad (4.18)$$

Where the operators d_1^\dagger and d_2^\dagger create an electron in dots 1 and 2 respectively⁴. Since the system is non-interacting, we ignore the spin-degeneracy of this Hamiltonian. The only new parameter here is the term t_{dots} , which represents the tunneling between both quantum dots.

Using equation (4.17) with $B = d_1^\dagger$ and A shifting among all the other operators we compute the following transport equations

$$(\omega - \epsilon_1) G_{d_1, d_1^\dagger}(\omega) = 1 + t_{dots} G_{d_2, d_1^\dagger}(\omega) + V_1^* \sum_k G_{c_k, d_1^\dagger}(\omega), \quad (4.19)$$

$$(\omega - \epsilon_k) G_{c_k, d_1^\dagger}(\omega) = V_1 G_{d_1, d_1^\dagger}(\omega) + V_2 G_{d_2, d_1^\dagger}(\omega), \quad (4.20)$$

$$(\omega - \epsilon_2) G_{d_2, d_1^\dagger}(\omega) = t_{dots} G_{d_1, d_1^\dagger}(\omega) + V_2^* \sum_k G_{c_k, d_1^\dagger}(\omega). \quad (4.21)$$

This system is already closed, hence, it will have a unique solution. The associated matrix form is

$$\begin{bmatrix} \omega - \epsilon_2 & -V_2 & -t_{dots} \\ -V_2^* & \omega - \epsilon_k & -V_1 \\ -t_{dots}^* & -V_1^* & \omega - \epsilon_1 \end{bmatrix} \begin{bmatrix} G_{c_k, d_1^\dagger}(\omega) \\ G_{d_2, d_1^\dagger}(\omega) \\ G_{d_1, d_1^\dagger}(\omega) \end{bmatrix} = \begin{bmatrix} 0 \\ 0 \\ 1 \end{bmatrix} \quad (4.22)$$

By convenience we changed the order of the rows in the matrix and we removed the sum over k (\sum_k) to simplify the algebraic operations. We will insert these terms back in the equations at the end of the procedure.

⁴This case is different from the Anderson model defined in section 3.2, where the d_i^\dagger where creation operators in distinct energy levels, not dots.

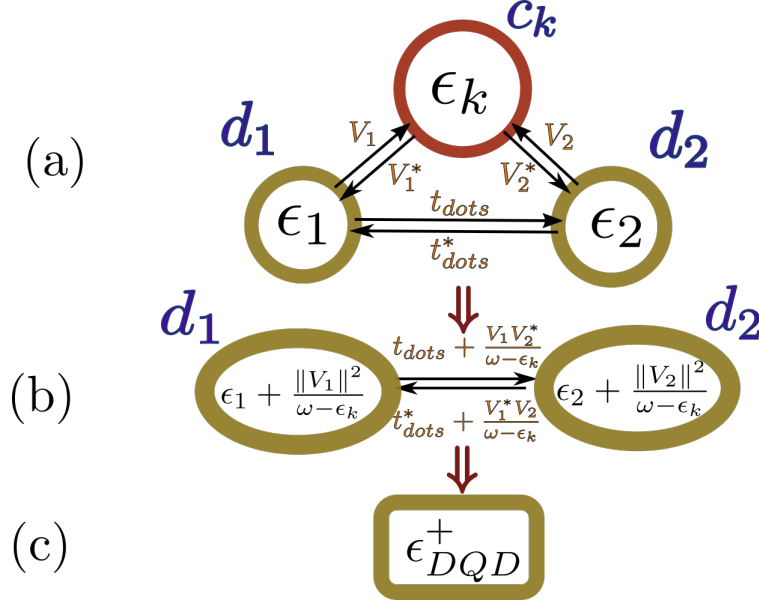


Figure 4.1: Graph representation of Gauss-Jordan elimination a) Graph $\mathcal{G}_{d_1 d_2}$ b) After the elimination of vertex c_k , the energies of dots d_1 and d_2 , and the coupling parameter are changed. c) After Gaussian elimination of dot 2 the energy of the remaining dot ϵ_{DQD}^+ represents the transport information through d_1 of the entire DQD.

Although this matrix is not Laplacian, the procedure in [53] can still be applied with the downside of loosing part of the speed-up of the algorithm. We still preserve some of the advantages of using graphs, such as the schematic representation of the transport process, the possibility of taking minimal cuttings and the relation between Gauss-Jordan elimination and random walks [53]. All of these, simplify the complexity of the solution.

Now, our goal is to compute the green function $G_{d_{1\downarrow} d_{1\downarrow}^\dagger}(\omega)$. To this end, we take the graph $\mathcal{G}_{d_1 d_2}$ associated to the matrix (4.22) (See Figure 4.1(a)). The vertexes of this graph are the operators in the first site of the of the green functions $(d_{1\downarrow}, d_2, c_k, d_1^\dagger)$. d_1^\dagger is not included since it only appears in the second sub-index of the green functions. The edges are given by the non-diagonal sites in the matrix multiplied by -1 and there is a self-energy assigned to each vertex, equal to the difference between ω and the corresponding diagonal term. These self-energies can also be understood as additional edges connecting each vertex with itself. The plot of the energy parameters in this algorithm is quite important, hence we prefer to keep this name to differentiate them from the other couplings.

The algorithm consists in the following: Each step of Gauss-Jordan elimination leads to a new graph with different energies and couplings. The elimination of a row and column is equivalent to eliminate the corresponding vertex in the graph. For instance, lets eliminate the

4.1. Green function formalism

first row and column of the matrix in (4.22). For it we just need to subtract the rank-1 matrix with the same first row and first column

$$\begin{bmatrix} \omega - \varepsilon_k & -V_2 & -V_1 \\ -V_2^* & \omega - \varepsilon_2 & -t_{dots} \\ -V_1^* & -t_{dots}^* & \omega - \varepsilon_1 \end{bmatrix} - \begin{bmatrix} \omega - \varepsilon_k & -V_2 & -V_1 \\ -V_2^* & \frac{V_2^* V_2}{\omega - \varepsilon_k} & \frac{V_2^* V_1}{\omega - \varepsilon_k} \\ -V_1^* & \frac{V_2 V_1^*}{\omega - \varepsilon_k} & \frac{V_1^* V_1}{\omega - \varepsilon_k} \end{bmatrix} \quad (4.23)$$

$$= \begin{bmatrix} 0 & 0 & 0 \\ 0 & \omega - \varepsilon_2 - \frac{V_2^* V_2}{\omega - \varepsilon_k} & -t_{dots} - \frac{V_2^* V_1}{\omega - \varepsilon_k} \\ 0 & -t_{dots}^* - \frac{V_2 V_1^*}{\omega - \varepsilon_k} & \omega - \varepsilon_1 - \frac{V_1^* V_1}{\omega - \varepsilon_k} \end{bmatrix} \quad (4.24)$$

The graph associated to this new matrix can be observed in Figure 4.1(b) where operator c_k has been removed. It is possible to associate the correction to the the energies and couplings to the possible walks passing through the vertex c_k . For instance d_1 's energy ε_1 receives an extra term $\frac{V_1^* V_1}{\omega - \varepsilon_k}$ representing an additional walk from d_1 to d_1 passing through c_k . The same logic can be applied to the other coupling terms. The correction to t_{dots} is $\frac{V_2^* V_2}{\omega - \varepsilon_k}$ which corresponds to a path from d_1 to d_2 passing through the eliminated vertex c_k . Note that this term includes the multiplication of both couplings V_1, V_2^* divided by the difference of ω with the self-energy ε_k of the vertex. This correspondence between the energy correction and eliminated paths through the graph makes the "vertex-elimination" process a straightforward task.

We now proceed to eliminate vertex d_2 , which leaves just a single vertex as shown in Figure 4.1(c). The self-energy of it can be readily computed with the previous path elimination idea which gives

$$\varepsilon_{DQD}^+ = \varepsilon_1 + \sum_{\mathbf{k}} \frac{V_1 V_1^*}{\omega - \varepsilon_{\mathbf{k}}} + \frac{\left\| t_{dots} + \sum_{\mathbf{k}} \frac{V_1 V_2^*}{\omega - \varepsilon_{\mathbf{k}}} \right\|^2}{\omega - \varepsilon_2 - \sum_{\mathbf{k}} \frac{V_2 V_2^*}{\omega - \varepsilon_{\mathbf{k}}}}, \quad (4.25)$$

where we selectively included the $\sum_{\mathbf{k}}$ -terms in the places where k appeared.

As a result of Gauss-Jordan elimination, the linear equation in (4.22) has evolved into the trivial form

$$\begin{bmatrix} 0 & 0 & 0 \\ 0 & 0 & 0 \\ 0 & 0 & \omega - \varepsilon_{DQD}^+ \end{bmatrix} \begin{bmatrix} G_{c_{\mathbf{k}}, d_1^\dagger}(\omega) \\ G_{d_2, d_1^\dagger}(\omega) \\ G_{d_1, d_1^\dagger}(\omega) \end{bmatrix} = \begin{bmatrix} 0 \\ 0 \\ 1 \end{bmatrix}. \quad (4.26)$$

The Green function is then

$$G_{d_1, d_1^\dagger}(\omega) = \frac{1}{\omega - \varepsilon_{DQD}^+} = \left[\left(\omega - \varepsilon_1 - \sum_{\mathbf{k}} \frac{V_1 V_1^*}{\omega - \varepsilon_{\mathbf{k}}} \right) - \frac{\left(t_{dots} + \sum_{\mathbf{k}} \frac{V_1 V_2^*}{\omega - \varepsilon_{\mathbf{k}}} \right) \left(t_{dots} + \sum_{\mathbf{k}} \frac{V_1 V_2^*}{\omega - \varepsilon_{\mathbf{k}}} \right)^*}{\omega - \varepsilon_2 - \sum_{\mathbf{k}} \frac{V_2 V_2^*}{\omega - \varepsilon_{\mathbf{k}}}} \right]^{-1}. \quad (4.27)$$

This Green function will appear again in the last chapter when solving the double dot-Majorana system.

4.1.3 Graph Algorithm

In this part we summarize the steps of the Graph-Gauss-Jordan elimination process to compute the Green function $G_{d,d^\dagger}(\omega)$ of an operator d :

1. Computing the transport equations with the second term of the Green function fixed in the creation operator d^\dagger at all equations.
2. Setting up the graph associated to the transport system. The self-energy of each vertex is initialized as ω minus the corresponding diagonal term. The edge weights are given by the coupling of the off-diagonal terms multiplied by -1 .
3. Eliminating the vertexes of the graph one by one. Each vertex-elimination process carries the following steps.
 - (a) Computing the extra-terms of the energies and couplings based on the walks passing through the eliminated vertex.
 - (b) Removing this vertex from the graph.
 - (c) Iterating till there is only one vertex.
4. The energy in the remaining vertex d is the self-energy $\varepsilon_d = \omega - \frac{1}{G_{d,d^\dagger}(\omega)}$.

This algorithm will be our main method to find the Green function and therefore the density of states of any non-interacting system.

4.1.4 Non-interacting DOS in a double quantum dot coupled to a lead

In this subsection, we describe the remaining steps to obtain the density of states of the double quantum dot from the Green function (4.27). We will plot the results and observe the evolution of the DOS while tuning the parameters of the model.

First note that equation (4.27) depends on the term $\sum_k \frac{V_i^* V_j}{\omega - \varepsilon_k}$, which describes the broadening of the DOS when the QD enters in contact with the lead. This broadening is usually named $\Gamma_i = V_i^* V_i$ (Or Δ depending on the text book). In general, V_i is a function of \mathbf{k} . However, in the limit of flat-band we can assume that V_i is constant. Therefore, it is enough to integrate

$$\sum_k \frac{1}{\omega - \varepsilon_k + is} = \int_{-D}^D \frac{d\varepsilon_k}{\omega - \varepsilon_k + is} = -\ln \left(\frac{D - \varepsilon_k + is}{-D - \varepsilon_k + is} \right) \xrightarrow[D \rightarrow \infty]{} -i, \quad (4.28)$$

where we assumed that there is a maximum energy cutoff D going to infinity in the wide-band limit. Hence

$$-i\Gamma_i = \sum_k \frac{V_i^* V_i}{\omega - \varepsilon_k}. \quad (4.29)$$

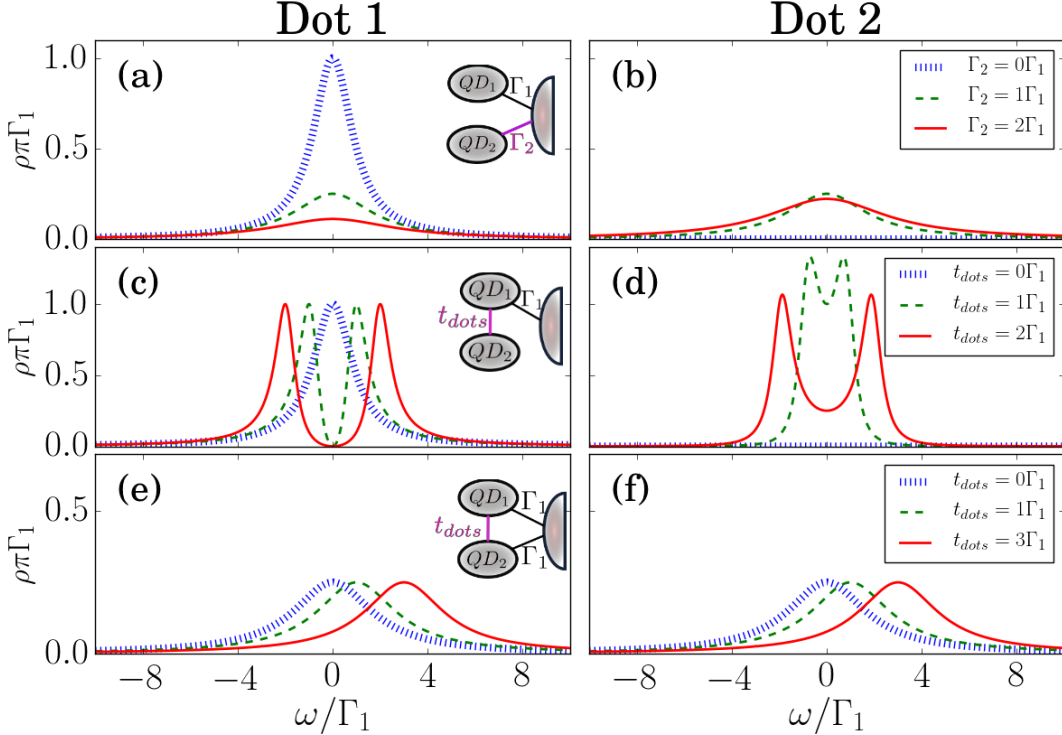


Figure 4.2: Evolution of the density of states at each QD (Left: dot 1, Right: dot 2) at three distinct arrangements of DQD-lead coupling. The inset at the first column depicts the type of coupling. The purple line represents the tuning variable. The energy unit is Γ_1 . $e_1 = e_2 = 0$ in all arrangements. (a),(b) The lead is connected to both QDs. Tuning variable: Γ_2 . (c)(d) Indirect coupling of the second dot through dot one. Tuning variable: t_{dots} . (e)(f) Triangular coupling. Tuning variable: t_{dots} .

We can replace this in equation (4.27) to obtain the real expression for the green function $G_{d_1,d_1^\dagger}(\omega)$. The terms of the form $V_1 V_2^*$ can be replaced for $\sqrt{\Gamma_1 \Gamma_2}$, supposing there is no additional complex phase.

Now, remember from (4.12) that the DOS ρ depends on the imaginary factor of the Green Function $G_{d_1,d_1^\dagger}(\omega)$. This term depends in the broadening Γ . If $\Gamma = 0$ the density of states will be 0 as well. At any other case, one of the dots should be attached to the lead. Let Γ_1 be the broadening of this dot. We will take Γ_1 as our unit for the rest of this thesis.

In Figure 4.2 we can observe the evolution of the Density of States under certain processes. Each plot includes an inset showing the model applied to the figure. The coupling in purple indicates the tuning variable. We set $e_1 = e_2 = 0$ so that both dots satisfy PHS. The primary results are the

1. **Coupling QD2. Figure 4.2(a)(b):** At $\Gamma_2 = 0$ the second dot is decoupled, hence the first dot's DOS is the same of a single dot case. The maximum height is achieved at $\rho\pi\Gamma_1 = 1$ and the width of this peak is approximately Γ_1 , just as in Figure Figure 3.2. When the second dot is attached $\Gamma_2 > 0$, the density of states is divided between both dots. At $\Gamma_1 = \Gamma_2$ the DOS at the Fermi energy is equal to $\frac{1}{4\pi\Gamma}$ for both dots. For higher values of Γ_2 , the DOS in the second dot is higher than in the first one.
2. **Indirect Coupling of QD2. Figure 4.2(c)(d):** This case is interesting. When the second dot is connected indirectly through the first dot, quantum inference splits the central peak in two new states. We will observe later that in the interacting case this procedure can also destroy the Kondo signature. Note that the higher the coupling t_{dots} is, the greater is the gap between the states. We will usually take $t_{dots} = 2\Gamma_1$ to make these gap more visible in the NRG simulations.
3. **Breaking Particle Hole Symmetry. Figure 4.2(e)(f):** Suppose we have $\Gamma_2 = \Gamma_1$. The "triangular connections" break Particle Hole Symmetry, with the central peak detuning to the positive part of the spectrum. We will avoid this situation during this project, because because PHS-breaking will prevent the Majorana to tunnel inside the DQD. Hence, this model won't lead to any interesting result on Majorana manipulation.

4.2 The Numerical Renormalization Group (NRG)

The numerical renormalization group is renowned for providing the most successful and complete explanation of the Kondo problem. of integrating the strong correlations in coulomb interacting systems. In this chapter, we will review the main ideas of the NRG algorithm including the logarithmic discretization, the construction of Wilson's chain and the iterative diagonalization in symmetry blocks. At the end, we will give some specifications about our code and we will show its results in the model of a double quantum dot attached to a metallic lead.

4.2.1 From the Renormalization Group to Wilson's Chain

The real meaning of the divergent logarithmic term in the resistivity predicted by Kondo is that important contributions at low-energy scales caused by the strong quantum correlations in the system are being neglected by perturbation theory. This problem can be solved by introducing ideas from renormalization group theory. A renormalization approach is more adequate for this type of problem since it assigns an appropriate effective Hamiltonian to each scale of temperature. This provides a more accurate representation of the increasing density of correlated states appearing close the Fermi energy.

In renormalization group theory, the Hamiltonian transformations are performed by an operator \mathcal{T} that represents an endomorphism in the space of operators. \mathcal{T} generates the semigroup

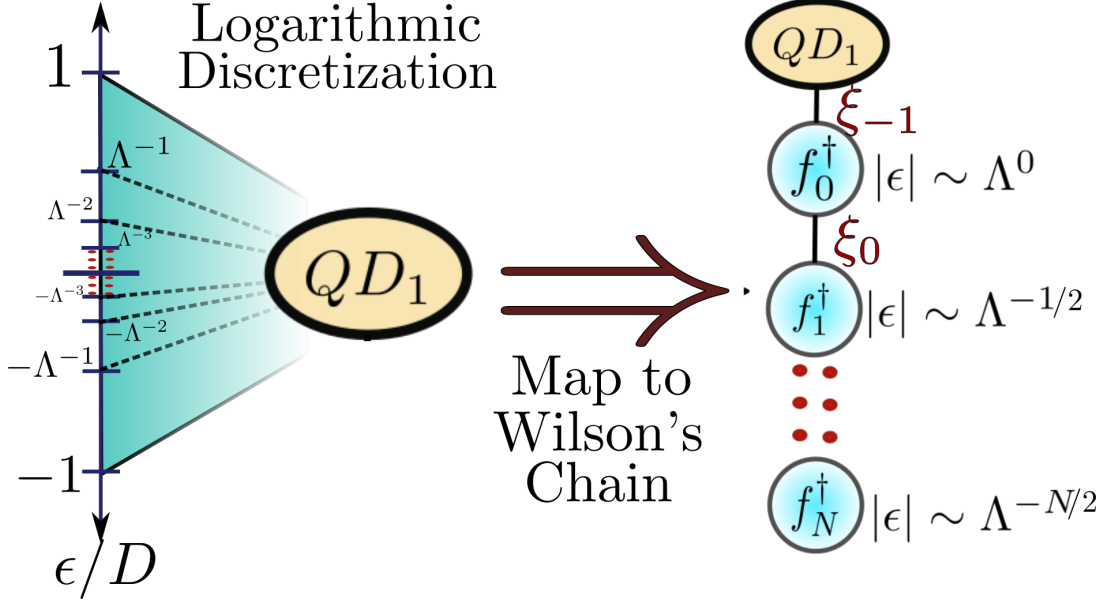


Figure 4.3: NRG algorithm: The logarithmic discretization of the conduction band according to the discretization parameter Λ . The system with the lead attached to the QD-impurity is mapped to the Wilson's chain, such that each step of the chain contains the contributions at different energy scales $\Lambda^{-N/2}$.

$\{1, \mathcal{T}, \mathcal{T}^2, \dots\}$, that defines a complete set of transformations

$$\mathcal{T}[H_0] = H_1, \mathcal{T}[H_1] = H_2, \dots, \mathcal{T}[H_N] = H_{N+1}, \dots$$

If \mathcal{T} is a contracting map⁵ then it is known that this set of operations should eventually lead to a fix point $\mathcal{T}^N[H] \xrightarrow{N \rightarrow \infty} H^*$ such that $\mathcal{T}[H^*] = H^*$. In numerical simulations, N will only increase up to a value where H_N is close enough to the fix point H^* so that no new significant contributions to the Hamiltonian are obtained. For the purposes of this project, taking $N = 51$ will be enough for the NRG code to converge.

In the 1970's G.Wilson used this theory to create the famous Numerical Renormalization Group (NRG) [11, 47, 54]. His main idea was to perform a logarithmic discretization of the conduction band in the lead as shown in Figure 4.3.(Left). Taking into account that the leading contributions to the conductance occur at states close to the Fermi energy $\omega = 0$, we can define a cut-off ($|\omega| < D$) so that the rest at higher contributions are not relevant. Then we use D to rescale the energy interval. As you can observe in the figure, the QD is coupled to all these energy states at the same time. The logarithmic discretization gives more relevance to the

⁵ Let \mathcal{O} be a set of operators, then T is a contracting map if $\mathcal{T}[\mathcal{O}'] \subset \mathcal{O}'$ for every $\mathcal{O}' \subset \mathcal{O}$.

low energy scales by assigning a different Hamiltonian coupling to each one of them. The discretized intervals are determined by a variable $\Lambda > 1$. This value has certain relevance on the convergence of the code. If it is selected to small ($\Lambda \sim 1$) it might never converge, but if it is too high it could produce misleading results. In this thesis we use a definite value of $\Lambda = 2.5$. This value was tested several times, giving positive results.

To complete this idea, the NRG code maps the Hamiltonian of the QD-lead system to the Wilson's chain shown in Figure 4.3(Right), so that each step of the chain contains the contributions of a different energy scale. A detailed description of this map is included in the Appendix section A.1. After these steps we obtain a chain Hamiltonian of the form

$$H = H_d + D \sum_{\sigma} \left[\sqrt{\frac{2\Gamma}{\pi D}} (d_{\sigma}^{\dagger} f_{0\sigma} + f_{0\sigma}^{\dagger} d_{\sigma}) + \frac{1}{2} (1 + \Lambda^{-1}) \sum_{n=0}^{\infty} \Lambda^{-\frac{n}{2}} \xi_n (f_{n\sigma}^{\dagger} f_{n+1,\sigma} + f_{n+1,\sigma}^{\dagger} f_{n\sigma}) \right]. \quad (4.30)$$

In the flat-band approximation the parameters ξ_n can be obtained analytically [11]

$$\xi_n = \frac{1 - \Lambda^{-n-1}}{(1 - \Lambda^{-2n-1})^{\frac{1}{2}} (1 - \Lambda^{-2n-3})^{\frac{1}{2}}}.$$

From equation (4.30) we define the following sequence of shell Hamiltonians

$$H_{N+1} = T[H_N] = \Lambda^{\frac{1}{2}} H_N + \xi_N (f_{N+1,\sigma}^{\dagger} f_{N,\sigma} + f_{N,\sigma}^{\dagger} f_{N+1,\sigma}), \quad (4.31)$$

with

$$H_{-1} := \frac{2H_d \Lambda^{-1/2}}{D(1 + \Lambda^{-1})}, \quad \xi_{-1} = \sqrt{\frac{2\Gamma}{\pi D}}. \quad (4.32)$$

Note that at each step H_N is being rescaled by a factor $\Lambda^{1/2}$ before including the following contribution. This is performed iteratively to eliminate the high order excitations, which allows to obtain an effective model valid for the lower energies. In consequence, each Hamiltonian H_N represents only the physics that is relevant at the energy scale $\Lambda^{-N/2}$.

On the other hand, the Renormalization Group transformation \mathcal{T} can be defined as

$$\mathcal{T}^N H_{-1} = \frac{1 + \Lambda^{-1}}{2} \Lambda^{-\frac{N}{2}} H_N$$

In the limit $\xrightarrow{N \rightarrow \infty}$ we should recover the initial Anderson Hamiltonian. In addition, note that the leading coefficients of the contributions to each Hamiltonian H_N are given by

$$\Lambda^{-\frac{N}{2}} \xi_N \xrightarrow{N \rightarrow \infty} \frac{\Lambda^{-\frac{N}{2}} (1 - \Lambda^{-N})}{1 - \Lambda^{-2N}} \sim \frac{\Lambda^{-\frac{N}{2}}}{1 + \Lambda^{-N}},$$

which decays exponentially with the length of the chain. Therefore, we may think that at some point these new contributions will be so small that the map \mathcal{T} will eventually

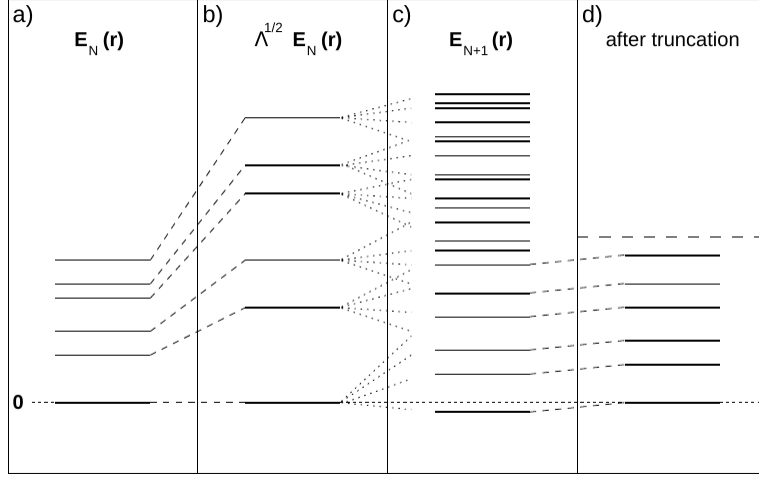


Figure 4.4: Schematic representation of the spectrum in the iterative diagonalization process. a)→b): Rescaling. b)→c): Including next site and diagonalizing. c)→d): Truncation of high energy states . Adapted from [11]

converge. Formally the theory for NRG convergence is too complex for this thesis. However the results show that the operator that truly converges is \mathcal{T}^2 and not \mathcal{T} [54]. This has important consequences, for instance the convergence of the code has to be analyzed on odd and even values of N separately.

To this point, the equation (4.30) and the derived limit of H_N to the Anderson Hamiltonian are exact expressions. The first approximations will be performed in the following section which describes the iterative diagonalization of the shell Hamiltonians.

4.2.2 Iterative Diagonalization

The diagonalization begins with the dot-impurity Hamiltonian H_{-1} , which must be written in matrix form according to a defined basis. The other steps can be defined by induction. Suppose that the spectrum of H_N is diagonal on a given basis. Then the NRG code performs each of the following steps:

1. Rescaling the spectrum of H_N by $\Lambda^{\frac{1}{2}}$ as defined in (A.12). Figure 4.4 (a)→(b).
2. Adding the next step of the chain to form H_{N+1} and diagonalizing the new Hamiltonian such that $H_{N+1} = U_{N+1}^\dagger D_{N+1} U_{N+1}$. After this step, each of the eigenstates of H_N will split in up to 4 new energy states (probably degenerate) determined by the new coupling with the $N + 1$ site basis $|0\rangle, |\uparrow\rangle, |\downarrow\rangle, |\uparrow\downarrow\rangle$. Figure 4.4 (b)→(c).

3. Shifting the spectrum by a certain dephase factor such that the zero of energy is always the ground state. Figure 4.4 (c)→(d).
4. Numerical cutting: If the number of states in the system exceeds a definite number (1000 in this thesis) the exceeding higher energy states are neglected ⁶. This is in agreement with the previously exposed idea of eliminating high order excitations to obtain a valid effective model at low energies. Figure 4.4 (c)→(d).
5. Rotating operators $f_{N,\sigma}$ by $U_N f_{N,\sigma} U_N^\dagger$ to start the next operation.

The final outcome of this operations will be the complete spectrum of the Anderson model at each energy level. However we still need to talk about an important speed-up to the code obtain when considering the symmetries of the system.

4.2.3 Symmetries

The symmetries of the initial Hamiltonian take a very important role in this iterative diagonalization. Lets suppose that the initial Hamiltonian H_d has certain symmetries classified by the quantum number S . Then H_d can be written in block Hamiltonians over a basis of the form $|S, i\rangle$. A diagnoalization process of an square matrix with L rows usually has square order, proportionate to the number of entries $\mathcal{O} \sim L^2$. However, if the matrix is organized in blocks of length L_j such that $\sum_j L_j = L$, then the order of diagonalization will be around $\sum_j L_j^2$ which is in general much smaller than $(\sum_j L_j)^2 L^2$. Therefore the block diagonalization provides an important numerical speed-up to the algorithm.

To maintain this advantage, we must preserve this symmetry structure for the rest of the NRG code. For it, we first need to verify that the picked symmetry also commutes with the hopping terms in the chain Hamiltonian. If so, for each step N of the NRG algorithm the H_N Hamiltonian can be written in a block diagonal form with basis $|S_N, i_N\rangle$. Then it is necessary to define transition rules from the quantum numbers S_N to S_{N+1} . By doing this, we assure that the block architecture is transmitted through the entire algorithm, hence reducing the computational time significantly at each step of the NRG chain. This is a key procedure to optimize the algorithm

In the following subsection we will give a example of this symmetry propagation in the model a quantum dot attached to a metallic lead.

4.2.4 Iterative diagonalization in a single QD attached to a metallic lead

Now that we have an iterative representation of the Anderson Model Hamiltonian (4.30), we will describe how the NRG code works for a QD attached to a lead. We start with the dot Hamiltonian.

⁶ This step must be performed carefully to preserve the symmetries of the system. If two states are entangled and one of them is eliminated and the other is not, the program could lead to misleading results. Further discussions to solve this problem are presented in the symmetry subsection.

$$H_d = \frac{1}{D} \left(\varepsilon + \frac{U}{2} \right) d_\sigma^\dagger d_\sigma + \frac{U}{2D} (d_\sigma^\dagger d_\sigma - 1)^2. \quad (4.33)$$

Now observe that Hamiltonian (4.33) is already in the diagonal form for the basis $\{| \uparrow\downarrow \rangle, | \uparrow \rangle, | \downarrow \rangle, | 0 \rangle\}$

$$H_d = \frac{1}{D} \begin{bmatrix} 2\varepsilon + \frac{3U}{2} & 0 & 0 & 0 \\ 0 & \varepsilon + \frac{U}{2} & 0 & 0 \\ 0 & 0 & \varepsilon + \frac{U}{2} & 0 \\ 0 & 0 & 0 & \frac{U}{2} \end{bmatrix}.$$

Lets define $H_{-1} := \frac{2H_d\Lambda^{-1/2}}{1+\Lambda^{-1}}$ as in 4.32. It is convenient here to define unit-less variables $\varepsilon' = \frac{2\varepsilon\Lambda^{-1/2}}{D(1+\Lambda^{-1})}$, $U' = \frac{2U\Lambda^{-1/2}}{D(1+\Lambda^{-1})}$ and $\Gamma' := \sqrt{\frac{2\Gamma}{\pi D}}$. Then adding the first site of the Wilson's chain interaction to H_d we obtain a new Hamiltonian of the form

$$H_0 = \Lambda^{\frac{1}{2}} H_{-1} + \Gamma' \left(d_\sigma^\dagger f_{0\sigma} + f_{0\sigma}^\dagger d_\sigma \right). \quad (4.34)$$

The Hilbert space for this mew Hamiltonian must be extended to include the 4 degrees of freedom of the $f_{0\sigma}^\dagger$ particles, which are given by $\{| \uparrow\downarrow \rangle, | \uparrow \rangle, | \downarrow \rangle, | 0 \rangle\}$. Therefore, the total Hilbert space for H_0 is given by a base of the form

$$| s_1 \rangle | s_2 \rangle := | s_1 \rangle \otimes | s_2 \rangle \text{ with } | s_i \rangle \in \{| \uparrow\downarrow \rangle, | \uparrow \rangle, | \downarrow \rangle, | 0 \rangle\}.$$

We obtain an space of dimension $4 \times 4 = 16$. Now, before adventuring to write the Hamiltonian for H_0 as a 16×16 -matrix note that H_{-1} preserves the total particle number \mathcal{N} and the total spin S . We can associate each state to one of these symmetries as

$$| \uparrow\downarrow \rangle \longrightarrow | \mathcal{N} = 2, S = 0 \rangle, | 0 \rangle \longrightarrow | \mathcal{N} = 0, S = 0 \rangle \quad (4.35)$$

$$| \uparrow \rangle \longrightarrow | \mathcal{N} = 1, S = \frac{1}{2} \rangle, | \downarrow \rangle \longrightarrow | \mathcal{N} = 1, S = -\frac{1}{2} \rangle. \quad (4.36)$$

The propagation rule for the symmetry is defined with the following identity

$$| \mathcal{N}_1, S_1 \rangle \otimes | \mathcal{N}_2, S_2 \rangle \subset | \mathcal{N}_1 + \mathcal{N}_2, S_1 + S_2 \rangle \quad (4.37)$$

Then we can use \mathcal{N} and S as quantum numbers to generate the the block structure of H_0 . We will observe that the terms in the diagonal will correspond to the eigenvalues of H_{-1} for the first space. The non-diagonal terms are the result of the hopping interactions with the first site.

$$H_{\mathcal{N}=0, S=0} :$$

$$H_{\mathcal{N}=4, S=0} :$$

$$| 0 \rangle | 0 \rangle \rightarrow \left[\frac{U'}{2} \right] \quad | \uparrow\downarrow \rangle | \uparrow\downarrow \rangle \rightarrow \left[2\varepsilon' + \frac{3U'}{2} \right]$$

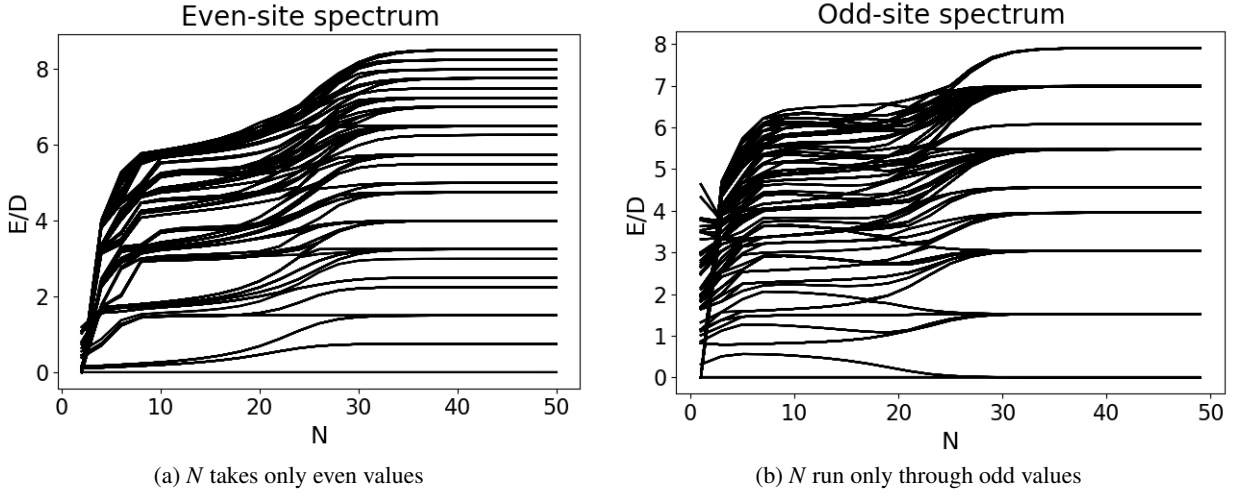


Figure 4.5: Evolution of the QD-spectrum vs number of iterations of the code for $U' = 0.5$, $\varepsilon' = -0.25$, $\Gamma = 2.82 \times 10^{-2}$.

$$H_{\mathcal{N}=1, S=\frac{1}{2}} :$$

$$H_{\mathcal{N}=1, S=\frac{-1}{2}} :$$

$$|\uparrow\rangle|0\rangle \rightarrow \begin{bmatrix} \epsilon' + \frac{U'}{2} & \Gamma' \\ \Gamma' & \frac{U'}{2} \end{bmatrix}$$

$$|\downarrow\rangle|0\rangle \rightarrow \begin{bmatrix} \epsilon' + \frac{U'}{2} & \Gamma' \\ \Gamma' & \frac{U'}{2} \end{bmatrix}$$

$$H_{\mathcal{N}=2,S=-1}:$$

$$H_{\mathcal{N}=2,S=1}:$$

$$|\downarrow\rangle |\downarrow\rangle \rightarrow \left[\epsilon' + \frac{U'}{2} \right]$$

$$|\uparrow\rangle|\uparrow\rangle \rightarrow \left[\epsilon' + \frac{U'}{2}\right]$$

$$H_{\mathcal{N}=2, S=0} :$$

$$\begin{aligned} |\uparrow\downarrow\rangle|0\rangle &\rightarrow \begin{bmatrix} 2\epsilon' + \frac{3U'}{2} & \Gamma' & -\Gamma' & 0 \\ \Gamma' & \epsilon' + \frac{U'}{2} & 0 & \Gamma' \\ -\Gamma' & 0 & \epsilon' + \frac{U'}{2} & -\Gamma' \\ 0 & \Gamma' & -\Gamma' & \frac{U'}{2} \end{bmatrix} \\ |\uparrow\rangle|\downarrow\rangle &\rightarrow \\ |\downarrow\rangle|\uparrow\rangle &\rightarrow \\ |0\rangle|\uparrow\downarrow\rangle &\rightarrow \end{aligned}$$

$$H_{\mathcal{N}=3, S=\frac{1}{2}} :$$

$$H_{\mathcal{N}=3, S=\frac{-1}{2}} :$$

$$|\uparrow\downarrow\rangle|\uparrow\rangle \rightarrow \begin{bmatrix} \epsilon' + \frac{U'}{2} & -\Gamma' \\ -\Gamma' & \frac{U'}{2} \end{bmatrix}$$

$$|\uparrow\downarrow\rangle|\downarrow\rangle \rightarrow \begin{bmatrix} \epsilon' + \frac{U'}{2} & -\Gamma' \\ -\Gamma' & \frac{U'}{2} \end{bmatrix}$$

The next step would be to diagonalize H_0 by blocks ($H_{\mathcal{N},S}$) and then including the next place in the chain. The following Hamiltonians are generated in the same way from equation

(4.31). The symmetries of the new states can be obtained from the propagation rule (4.37). When the number of states surpasses the 1000 states, the code will automatically cutoff the higher energy states. However it is important that a Block is not divided in this cutting, since it could break the preserved symmetry.

Finally, the spectrum for $\Lambda = 2.5$ takes the 'spaghetti' form in Figure 4.5. Note that before $N = 30$, the low-energy contributions generate significant changes in the energy levels. However, the stable spectrum after the step $N = 30$ is a signature that the code has converged. As we previously declared, it is not \mathcal{T} but \mathcal{T}^2 the transformation that has fixed points, which explains why it was necessary to plot the even and the odd spectrum separately.

At the end of the NRG code, we obtain a complete list of the spectrum ($E_{i,N}$) and the eigenstates ($|i,N\rangle$) of the Hamiltonian at each step N of the chain (See Figure 4.5). It is important to keep all of these states since each one of them represents different thermodynamic regimes of the system. While the site $N = 1$ represents the physics of the system relevant at temperatures around $\frac{D\Lambda^{-1}}{K_B}$, the site $N = 30$ shows the low energy contributions at $T \sim \frac{D\Lambda^{-30}}{K_B}$ where the ground state is strongly correlated. Furthermore, the states at low temperatures are entangled with the higher energy states. We need to take this into account to extract dynamical quantities of the system, which is the objective of the following section.

4.2.5 The Density Matrix Renormalization Group (DM-NRG)

The NRG codes allows us to compute several thermodynamic quantities such as the entropy S , the free energy and the partition function $Z(\beta)$. In addition, we can compute the spin magnetization or dynamical quantities such the density of states, the magnetic susceptibility and the conductivity. To perform this we can use the spectrum obtained in the NRG code to define the Boltzman distribution of the system. Then we apply the usual methods of statistical mechanics.

In this thesis we will focus in computing the density of states at the impurity (QD). For this, let $|j\rangle$ and $|q\rangle$ label a base of eigenstates of the Hamiltonian H . Now recall the definition of the retarded green function (4.9)

$$G_{d,d^\dagger}(t) = \theta(t) \langle \{d(t)d^\dagger(0)\} \rangle \quad (4.38)$$

$$= \theta(t) \left\langle \left[e^{\frac{i}{\hbar}Ht} d e^{-\frac{i}{\hbar}Ht} d^\dagger \right] \right\rangle + \theta(-t) \left\langle \left[d^\dagger e^{\frac{i}{\hbar}Ht} d e^{-\frac{i}{\hbar}Ht} \right] \right\rangle \quad (4.39)$$

$$= \theta(t) \sum_{|j\rangle, |q\rangle} p_j \langle j | e^{\frac{i}{\hbar}Ht} d | q \rangle \langle q | e^{-\frac{i}{\hbar}Ht} d^\dagger | j \rangle + \theta(-t) \sum_{|j\rangle, |q\rangle} p_q \langle q | d^\dagger e^{\frac{i}{\hbar}Ht} | j \rangle \langle j | d e^{-\frac{i}{\hbar}Ht} | q \rangle \quad (4.40)$$

$$= \theta(t) \sum_{|j\rangle, |q\rangle} p_j e^{\frac{-i}{\hbar}t(E_j - E_q)} \|\langle j | d | q \rangle\|^2 + \theta(-t) \sum_{|j\rangle, |q\rangle} p_q e^{\frac{i}{\hbar}t(E_j - E_q)} \|\langle j | d | q \rangle\|^2 \quad (4.41)$$

Where $p_j := \frac{e^{-\beta E_j}}{Z(\beta)}$ defines the Boltzmann probability of the eigenstate $|j\rangle$ according to Hamiltonian H .

4.2. The Numerical Renormalization Group (NRG)

It is known that the Fourier transform of an expression of the form $e^{-ax}\theta(x)$ is $\frac{1}{\omega+is-a}$. Then the Green function in the energy domain is

$$G_{d,d^\dagger}(\omega) = \frac{1}{Z(\beta)} \sum_{|j\rangle, |q\rangle} \frac{e^{-\beta E_j} + e^{-\beta E_q}}{\omega + is - E_j + E_q} \|\langle j|d|q\rangle\|^2. \quad (4.42)$$

From the imaginary part of (4.42) we obtain a formula for the spectral density in terms of the eigenstates and energies of the Hamiltonian

$$\rho_d = \frac{1}{Z(\beta)} \sum_{|j\rangle, |q\rangle} \left(e^{-\beta E_j} + e^{-\beta E_q} \right) \delta(\omega - E_j + E_q) \|\langle j|d|q\rangle\|^2. \quad (4.43)$$

This new expression for the DOS can be integrated into the NRG code in different ways . A first method created by Costi *et al.* consists in computing (4.43) with the eigenstates of each shell Hamiltonian H_N [55]. It is necessary to take into account that the operator d is constantly rotating after each diagonalization procedure, which produces different representations at each shell Hamiltonian basis. Then, an important part of Costi's algorithm is to obtain these new representations of d at the H_N -basis ($\langle j|d|q\rangle\|_N$) recursively starting from an input representation $\langle j|d|q\rangle\|_{N=0}$.

Although Costi's method predicts accurately the DOS at low-energies, it fails to fit the high energy levels. The method that corrects this problem receives the name of Density Matrix Numerical Renormalization Group (DMNRG) [12]. The main idea of DMNRG is to include the entanglement corrections with the lower energy-states using the density matrix formalism. For this, Hofstetter defines the density matrix at the last shell Hamiltonian N_{max} $\hat{\rho}$ as the thermal mixed state

$$\hat{\rho}_{N_{max}} = \sum_j e^{-\beta E_j} |j\rangle_{N_{max}} \langle j|, \quad (4.44)$$

where the subindex N_{max} suggests that $|j\rangle_{N_{max}} \langle j|$ is an eigenstate of the last shell Hamiltonian $H_{N_{max}}$.

With this new density matrix, we could rewrite (4.39) as

$$G_{d,d^\dagger}^{N_{max}}(t) = \text{Tr}(\hat{\rho}_{N_{max}} \theta(t) \{ d^\dagger(t), d(0) \}). \quad (4.45)$$

From the Green function $G_{d,d^\dagger}^{N_{max}}(t)$ we can obtain the density of states associated to the temperature $T_{N_{max}}$. Nevertheless, these results are not relevant at higher temperatures.

To solve this problem we may think Wilson's chain as an open quantum system where the environment are the low-energy sites of the chain and the system (ρ_{red}) contains the high-energy sites including the QD-impurity as observed in Figure 4.6. Using this analogy, we can readily obtain the density matrix ρ_S by taking the partial trace over the environment

$$\rho_{sys} = \text{Tr}_{env}[\rho_{N_{max}}]. \quad (4.46)$$

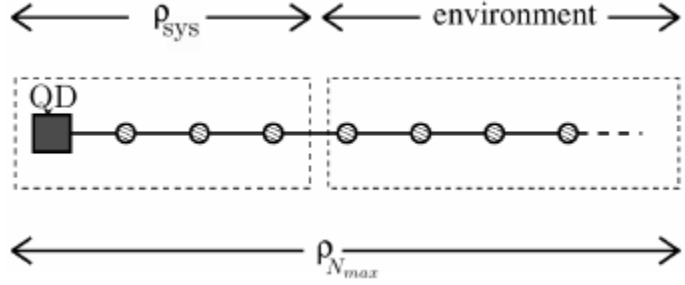


Figure 4.6: Wilson’s chain depicted as an open quantum system. Adapted from [12].

The DM-NRG code applies recursively this idea to obtain the density matrix corresponding to each scale of temperature T_N . It starts from $\rho_{N_{max}}$ defined at (4.44) and obtains $\rho_{N_{max}-1}$ by taking the partial trace over the vector space corresponding to the last site of the chain

$$\rho_{N_{max}-1} = \text{Tr}_{N_{max}}[\rho_{N_{max}}]. \quad (4.47)$$

The other density matrices are computed by induction as

$$\rho_{N-1} = \text{Tr}_N[\rho_N], \quad (4.48)$$

and the density of states at each temperature regime can be computed from the green function

$$G_{d,d^\dagger}^N(t) = \text{Tr}(\hat{\rho}_N \theta(t) \{ d^\dagger(t), d(0) \}). \quad (4.49)$$

The DM-NRG algorithm produces significantly better results at high energies than Costi’s initial idea. Indeed, DM-NRG is still one of the best methods to compute dynamic quantities of an impurity system. In the following subsection we will give some details of how DM-NRG is integrated with the NRG code.

4.2.6 Specifications of the NRG Code

The NRG code used in this thesis was implemented by my thesis advisor Luis Gregorio Dias during his posdoc at the University of Ohio. The general scheme is shown in Figure 4.7. It incorporates different stages.. Here we give a brief description of them:

- **Model:** The model defines the type of impurity that we are going to study. It could be a single QD or more complex structures such as a DQD or a Majorana-QD system. My main contribution to this code was at this stage. I designed the mode DQD-Majorana, which describes a DQD coupled to a Majorana zero mode. These models preserve different symmetries. In the single dot Hamiltonian presented in subsection 4.2.4 we used the symmetry $\mathcal{N}S_z$, which is equivalent to charge-spin QS_z . However we will find that Majorana systems require another symmetry-type that we call as $N \uparrow P \downarrow$. The model is defined

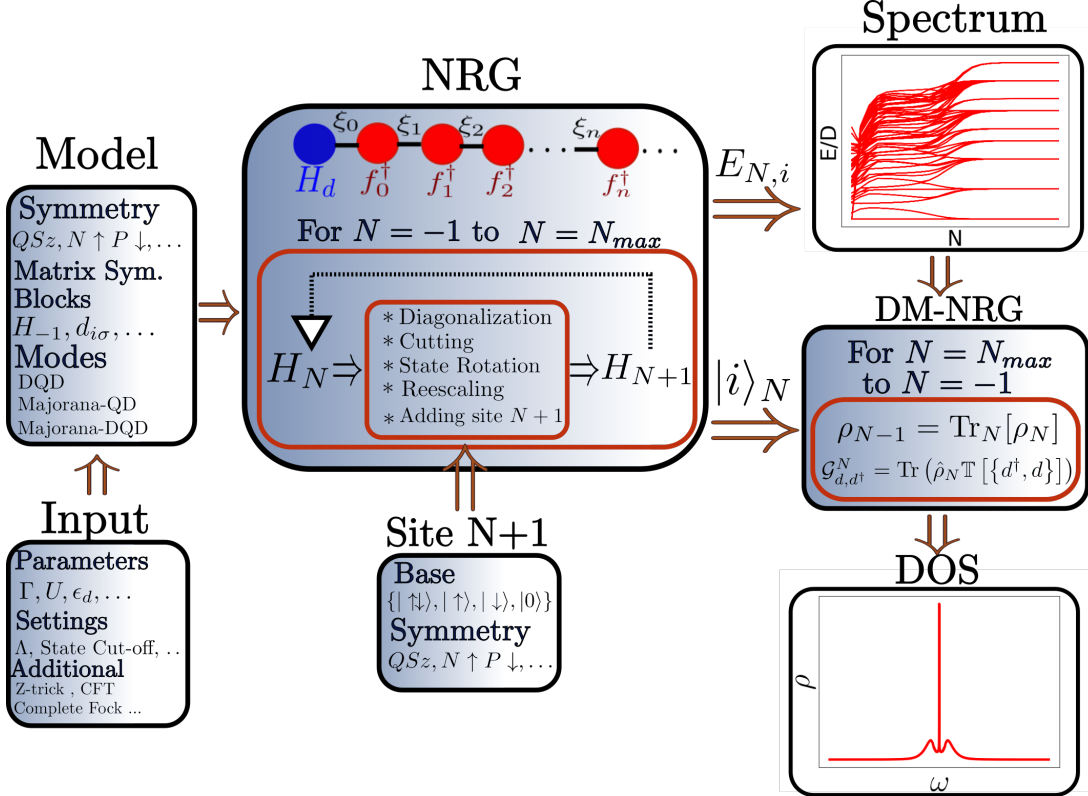


Figure 4.7: Diagram of the NRG code

by an initial Hamiltonian H_{-1} and the annihilation operators $d_{i\sigma}$ which must be submitted in the code written in the block symmetry representation described in subsection 4.2.3.

- **Input:** The input is a '.dat'-file that attributes a numerical value to each parameter of the model. In addition, it allows to set different code specifications as the number of iterations N_{max} , the scaling parameter Λ and the maximum number of states before the cut-off. It is also possible to include additional implementations to improve the results of the NRG code such as the Z-trick [56] and the Complete Fock State. In this project, we only used the Z-trick, which significantly improves the spectral resolution at high energies.
- **NRG:** This part of the code mainly integrates the ideas of subsection 4.2.1 and implements the iterative diagonalization described in subsection 4.2.2. Each shell Hamiltonian H_n is diagonalized. The high-energy eigenstates are cut-off if they exceed the maximum limit. Then, the states are rotated and the eigenvalues are rescaled to include the next step of the Wilson's chain. The symmetry block structure is preserved during the entire loop. NRG's output is a detailed evolution of the spectrum which produces the spaghetti form.

In addition, it can print the states and operators that are necessary to start other instances of the code like DM-NRG.

- **Site $N + 1$:** This is a small class that creates another site of the chain in the base $\{|\uparrow\downarrow\rangle, |\uparrow\rangle, |\downarrow\rangle, |0\rangle\}$. This base must be rewritten according to the symmetry quantum number. It is coupled with the matrices at the NRG code.
- **DM-NRG:** As described in subsection 4.2.5, this code generates iteratively the density matrix associated to each energy scale. Then it computes the green function and the density of states. The DOS of the single QD model is an example of its outputs. The plot shows the characteristic Kondo peak at the Fermi energy in the middle of the Coulomb peaks describing the energy states.

This NRG code is implemented in C++. It can be cloned from the Github link <https://git.io/fh9cM>. To optimize the performance of NRG, the code uses the packages Boost, LAPACK and Gnu Scientific Library (GSL), which provide a rapid interface for numerical matrix diagonalization.

4.2.7 NRG results in a double quantum dot coupled to a metallic lead

We now intend to observe the results of this code applied to the model double quantum dot attached to a metallic lead. The Hamiltonian for this system is the Anderson model with the impurity described by the interacting version of Hamilonian (4.18)

$$H_{DQD} = \sum_{i=1}^2 \sum_{\sigma} \left(\varepsilon_i + \frac{U_i}{2} \right) d_{i\sigma}^\dagger d_{i\sigma} + \left(\sum_{i\sigma} d_{i\sigma}^\dagger d_{i\sigma} - 1 \right)^2 + \sum_{\sigma} t_{dots} d_{1\sigma}^\dagger d_{2\sigma} + t_{dots}^* d_{2\sigma}^\dagger d_{1\sigma} \quad (4.50)$$

The Hilbert space of this system has 16-dimensions and the symmetries in this Hamiltonian are exactly the same than the ones in the single QD case \mathcal{NS} . Nevertheless, we decided to test the DQD-Majorana mode in this system. By setting the Majorana couplings to $t_1 = t_2 = 0$ we can decouple the Majorana mode, hence obtaining the DQD model (See chapter 6). The results we obtained are in agreement with previous previous papers [48], which was an important test to confirm the veracity of this new mode.

For the entire thesis we will fix the value of the coulomb repulsion parameters to

$$U_1 = U_2 = 17.7305\Gamma_1. \quad (4.51)$$

We picked these parameters considerably higher than the broadening unit Γ_1 to guarantee the appearance of Kondo physics at visible temperatures in comparison with the Coulomb peak.

NRG-code We used the same configurations from Figure 4.2. The results appear in Figure 4.8:

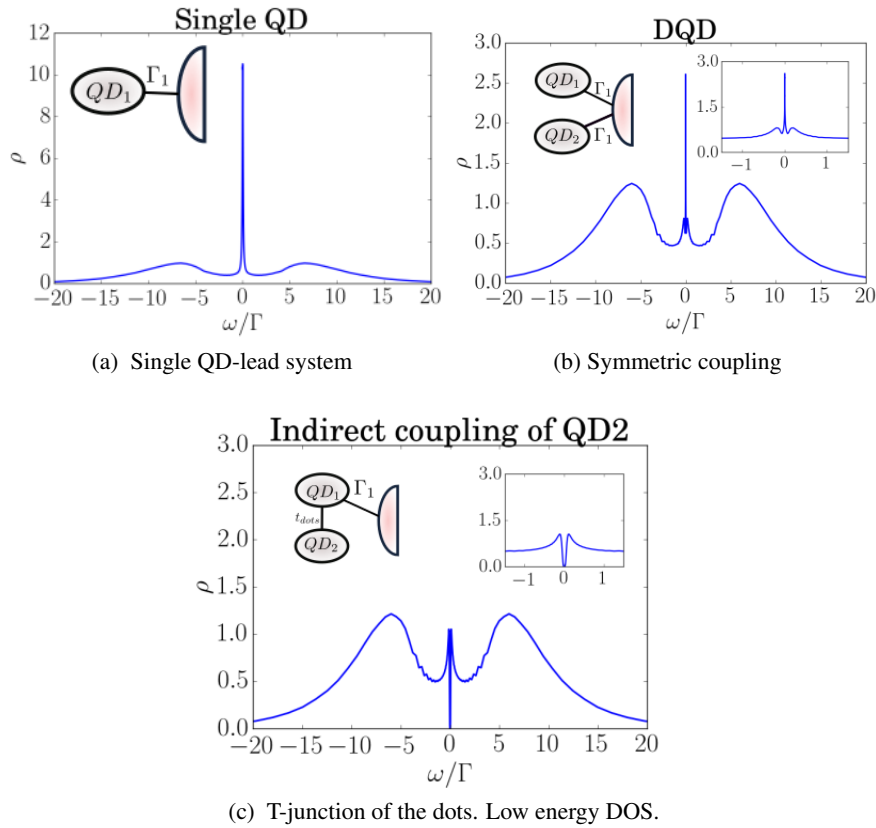


Figure 4.8: Density of states for the DQD attached to the lead at different configurations. Left insets: Setup that is being used. Right insets: Low energy DOS.

- The single QD attached to a metallic lead is a particular case of the double quantum dot model, where the second dot is not attached $\Gamma_2 = t_{dots} = 0$. Figure 4.8 shows the NRG results for this case. The three plots show the external Coulomb peaks at $e_1 = \frac{U}{2} \sim 8.62\Gamma_1$, which represent the DOS of the energy levels. In addition Figure 4.8a shows a central peak at the Fermi energy. Note, that there shouldn't be a state in this position since it is inside a gap between two energy levels (Coulomb peaks). **This is the Kondo Peak** [51]. This peak explains the zero-bias plateaus in Figure 3.5.
 - In Figure 4.8b we observe the DOS when the two QDs are symmetrically attached. At low energies, the inset shows the appearance of two satellite peaks representing the Ruderman-Kittel-Kasuya-Yosida (RKKY) interaction. This is an anti-ferromagnetic coupling that appears in the interacting case due to the strong correlations between both dots.
 - The most interesting case is in Figure 4.8c. As we already observed in the non-interacting

case, the interference with the second dot completely destroys the zero mode which is now formed by the Kondo peak. This effect is observed at low energies closed to $t_{dots} = 0.689\Gamma$. The paper describing this result was a central part of one of my advisor's project [48]. This result encouraged me to formulate the following question. What happens if we attached a Majorana mode to one of these dots?. Would it be destroyed by interference or it will survive to it. Solving this question is one of the main objectives of chapter 6.

With these results we finish the first test of our methods. We will probe them again in the next chapter in the QD-Majorana system, and again in chapter 6 to study the manipulation of Majorana zero modes in a double quantum dot.

Chapter 5

Coupling a QD with a Majorana zero mode

In the introduction we pointed out three properties that make particularly promising the QD-Majorana systems. These are:

1. It does not destroy the entire qubit information.
2. The possibility of exploring Kondo-Majorana physics.
3. It provides the unique opportunity of manipulating the Majorana zero modes inside the QDs, which has promising applications in the design of quantum architectures.

In this project we will exploit the second and the third properties to manipulate MZMs in double quantum dot systems in the Kondo regime. But before going through that model, we are going to test our methods in the single dot-Majorana system. As we will observe in this chapter, we were able to reproduce effectively the results of previous papers [36, 48].

5.1 Model

In this section we will recreate the results of Liu and Baranger using the methods developed in chapter 4. This will also allow us to probe our methods in a system with Majorana zero modes.

The Hamiltonian for Majorana-QD-lead hybrid system (See Figure 5.1) is given by

$$H = H_{QD-Lead} + H_{M-QD} + H_M. \quad (5.1)$$

Where $H_{QD-Lead}$ is the Hamiltonian for the non-interacting Anderson model (3.6), H_M is the Hamiltonian of the Majorana chain and H_{M-QD} represents the coupling between the QD and the Majorana Fermion at the boundary.

Now, the real question is how to define the coupling between the QD and the MBS. In fact, there are many ways to represent this interaction. One alternative is to replace in H_M with the entire Kitaev chain Hamiltonian (2.1) (or even with the Majorana chain (2.18)) and then pick H_{M-QD} as the coupling between the QD and the first site of the chain [37]. A simpler approach is to define an effective coupling with the Majorana operator at the edge of the Majorana chain. Since the Kitaev chain is spin-less, we choose to couple the Majorana to the spin- \downarrow channel of the QD⁷. Therefore, the Majorana fermion should be the superposition of the creation and

⁷An appropriate justification of this fact can be found in [1]

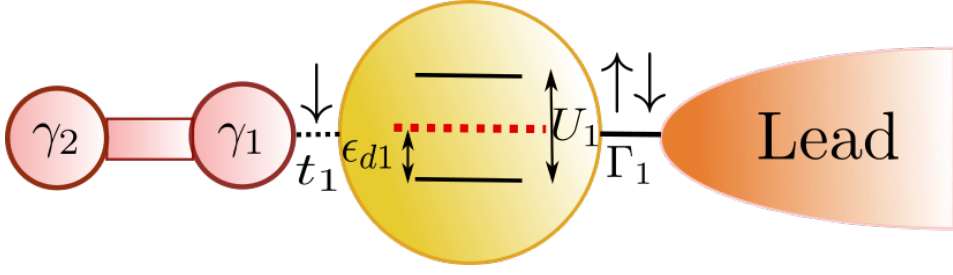


Figure 5.1: Model for the QD-Majorana system. Solid lines: Hopping interactions: V_1 couplings of QD1 . Dashed lines: Majorana spin- \downarrow effective couplings (5.2) t_1 . The atomic energy levels appear inside each QD ϵ_1 are tuned by the gate voltages. The coulomb interaction is represented by U_1 separates two energy levels. The red dashed horizontal lines represent the Fermi level.

annihilation operators of a spin \downarrow particle f_{\downarrow} :

$$\gamma_1 := \frac{1}{\sqrt{2}} (f_{\downarrow}^{\dagger} + f_{\downarrow}), \gamma_2 := \frac{1}{\sqrt{2}} (f_{\downarrow}^{\dagger} - f_{\downarrow}).$$

This makes possible to define an effective coupling between the Majorana Mode and the dot by attaching γ_1 with the spin- \downarrow channel in the QD

$$H_{M-QD} = t_1 (d_{\downarrow}^{\dagger} \gamma_1 + \gamma_1 d_{\downarrow}). \quad (5.2)$$

In addition the two Majoranas at the edges of the chain can have an internal coupling

$$H_M = \epsilon_M \gamma_1 \gamma_2. \quad (5.3)$$

According to Kitaev's initial paper [13], this coupling term decreases exponentially with the length of the chain. This explains why this term is not taken into account in many computations.

Replacing the Dirac fermion operators we obtain the following Hamiltonians

$$\begin{aligned} H_M &= \epsilon_m f_{\downarrow}^{\dagger} f_{\downarrow} \\ H_{M-QD} &= \frac{t_1}{\sqrt{2}} d_{1\downarrow}^{\dagger} f_{\downarrow} + \frac{t_1^*}{\sqrt{2}} f_{\downarrow}^{\dagger} d_{1\downarrow} + \frac{t_1}{\sqrt{2}} d_{1\downarrow}^{\dagger} f_{\downarrow}^{\dagger} + \frac{t_1^*}{\sqrt{2}} f_{\downarrow} d_{1\downarrow}. \end{aligned}$$

Finally we have the Hamiltonian

$$H = \sum_{k,\sigma} \left(\epsilon_k + \frac{U_1}{2} \right) d_{1\sigma}^{\dagger} d_{1\sigma} + \frac{U}{2} (d_{1\sigma}^{\dagger} d_{1\sigma} - 1)^2 + t_1 (d_{1\downarrow}^{\dagger} \gamma_1 + \gamma_1 d_{1\downarrow}) + V d_{1\sigma}^{\dagger} c_{k\sigma} + V^* c_{k\sigma}^{\dagger} d_{1\sigma} + \epsilon_m f_{\downarrow}^{\dagger} f_{\downarrow}. \quad (5.4)$$

The fidelity of this effective model has been discussed by Ruiz-Tijerina et al. [1] concluding that this model reproduces the same results than coupling a Kitaev chain model in the topological phase to a QD. (This statement is true even for more realistic models of the TS including Rashba spin-orbit interactions and a Zeeman field [1]).

5.2 Non-interacting QD coupled to Majorana chain

In the non-interacting case we can use the ballistic transport equations from section 4.1. The green functions are then determined by the following set of linear equations.

$$(\omega - \varepsilon_M) G_{f_{\downarrow}, d_{1\downarrow}^{\dagger}}(\omega) = (\omega + \varepsilon_M) G_{f_{\downarrow}^{\dagger}, d_{1\downarrow}^{\dagger}}(\omega) = \frac{t_1^*}{\sqrt{2}} \left(G_{d_{1\downarrow}, d_{1\downarrow}^{\dagger}}(\omega) - G_{d_{1\downarrow}^{\dagger}, d_{1\downarrow}^{\dagger}}(\omega) \right) \quad (5.5)$$

$$(\omega - \varepsilon_1) G_{d_{1\downarrow}, d_{1\downarrow}^{\dagger}}(\omega) = 1 + \frac{t_1}{\sqrt{2}} t_1 G_{f_{\downarrow}, d_{1\downarrow}^{\dagger}}(\omega) + \frac{t_1}{\sqrt{2}} t_1 G_{f_{\downarrow}^{\dagger}, d_{1\downarrow}^{\dagger}}(\omega) + V_1 \sum_{\mathbf{k}} G_{c_{\mathbf{k}\downarrow}, d_{1\downarrow}^{\dagger}}(\omega) \quad (5.6)$$

$$(\omega - \varepsilon_{\mathbf{k}}) G_{c_{\mathbf{k}}, d_{1\downarrow}^{\dagger}}(\omega) = V_1^* G_{d_{1\downarrow}, d_{1\downarrow}^{\dagger}}(\omega) \quad (5.7)$$

$$(\omega + \varepsilon_1) G_{d_{1\downarrow}^{\dagger}, d_{1\downarrow}^{\dagger}}(\omega) = -\frac{t_1}{\sqrt{2}} G_{f_{\downarrow}, d_{1\downarrow}^{\dagger}}(\omega) - \frac{t_1}{\sqrt{2}} G_{f_{\downarrow}^{\dagger}, d_{1\downarrow}^{\dagger}}(\omega) - V_1^* \sum_{\mathbf{k}} G_{c_{\mathbf{k}\downarrow}^{\dagger}, d_{1\downarrow}^{\dagger}}(\omega) \quad (5.8)$$

$$(\omega + \varepsilon_{\mathbf{k}}) G_{c_{\mathbf{k}}^{\dagger}, d_{1\downarrow}^{\dagger}}(\omega) = -V_1^* G_{d_{1\downarrow}, d_{1\downarrow}^{\dagger}}(\omega) \quad (5.9)$$

The graph representing these green functions is in Figure 5.2 (a) (Look subsection 4.1.2 for details). However using that $(\omega - \varepsilon_M) G_{f_{\downarrow}, d_{1\downarrow}^{\dagger}}(\omega) = (\omega + \varepsilon_M) G_{f_{\downarrow}^{\dagger}, d_{1\downarrow}^{\dagger}}(\omega)$ we can take $G_{f_{\downarrow}^{\dagger}, d_{1\downarrow}^{\dagger}}(\omega)$ out of the equations. After eliminating this term from (5.6) it becomes

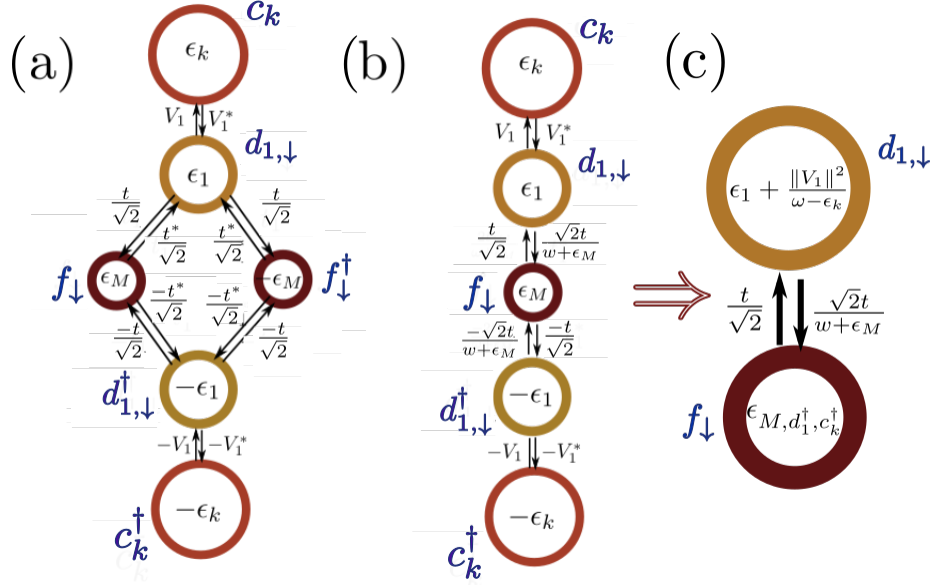
$$(\omega - \varepsilon_1) G_{d_{1\downarrow}, d_{1\downarrow}^{\dagger}}(\omega) = 1 + \frac{t_1}{\sqrt{2}} \left(1 + \frac{\omega - \varepsilon_M}{\omega + \varepsilon_M} \right) G_{f_{\downarrow}, d_{1\downarrow}^{\dagger}}(\omega) + V_1 \sum_{\mathbf{k}} G_{c_{\mathbf{k}\downarrow}, d_{1\downarrow}^{\dagger}}(\omega) \quad (5.10)$$

$$= 1 + \frac{\sqrt{2}t_1}{\omega + \varepsilon_M} G_{f_{\downarrow}, d_{1\downarrow}^{\dagger}}(\omega) + V_1 \sum_{\mathbf{k}} G_{c_{\mathbf{k}\downarrow}, d_{1\downarrow}^{\dagger}}(\omega) \quad (5.11)$$

Similarly,

$$(\omega + \varepsilon_1) G_{d_{1\downarrow}^{\dagger}, d_{1\downarrow}^{\dagger}}(\omega) = -\frac{\sqrt{2}t_1}{\omega + \varepsilon_M} G_{f_{\downarrow}, d_{1\downarrow}^{\dagger}}(\omega) - V_1^* \sum_{\mathbf{k}} G_{c_{\mathbf{k}\downarrow}^{\dagger}, d_{1\downarrow}^{\dagger}}(\omega) \quad (5.12)$$

With these new equations we can construct the graph is in Figure 5.2 (b) . Using the Graph-Gauss-Jordan algorithm from subsection 4.1.3 we proceed to eliminate vertexes c_k , c_k^{\dagger} and d_1^{\dagger} in that order. The result is the graph in figure Figure 5.2(c) with


 Figure 5.2: Graph \mathcal{G}_M representing the transport equations.

$$\epsilon_{M,d_1^\dagger,c^\dagger} = \epsilon_M + \frac{\omega}{\omega + \epsilon_M} \frac{\|t\|^2}{\omega + \epsilon_1 + \sum_{\mathbf{k}} \frac{V_1 V_1^*}{\omega + \epsilon_{\mathbf{k}}}}. \quad (5.13)$$

We finally eliminate f_\downarrow to obtain

$$G_{d_{1\downarrow},d_{1\downarrow}^\dagger}(\omega) = \left[\omega - \epsilon_1 - \sum_{\mathbf{k}} \frac{V_1 V_1^*}{\omega - \epsilon_1} - \frac{\omega}{\omega + \epsilon_M} \frac{\|t\|^2}{\omega - \epsilon_{M,d_1^\dagger,c^\dagger}} \right]^{-1}. \quad (5.14)$$

This is the Green function we have been looking for. After a few algebraic operations it is possible to show that this result is equivalent to the first computation done by Liu and Baranger in the paper [36].

To compute the DOS we need to replace $\sum \frac{V_1 V_1^*}{\omega - \epsilon_{\mathbf{k}}} = -i\Gamma_1$ as we already did in subsection 4.1.2. Note that these computations are only for the spin- \downarrow channel. The spin- \uparrow channel is even simpler since this channel is not coupled to the Majorana mode by convention. Hence it corresponds to the case of a single quantum dot coupled to a Lead. The results for the DOS can be observed in Figure 5.3. Each figure has an inset showing the model in the Majorana representation. The small blue and red balls are Majorana fermions just as the ones in figure Figure 2.2. The Majorana at the edge of the chain is represented by the isolated red ball connected to the QD (Figure 5.3a). The other isolated blue ball in Figure 5.3c represents the Majorana at the other edge which is connected to the sphere by the parameter ϵ .

- **Figure 5.3.(a),(b):** The spin- \uparrow DOS shows the result of coupling the QD with the lead and without Majoranas. When the parameter t is increased, the MZM is coupled to the spin- \downarrow which causes the dispersion of the DOS. The most relevant signature is the robust height of 0.5 in the DOS that is observed in the central peak for all $t > 0$. This mid-height DOS is responsible for the decay of half a quanta in the conductivity of the QD [36].

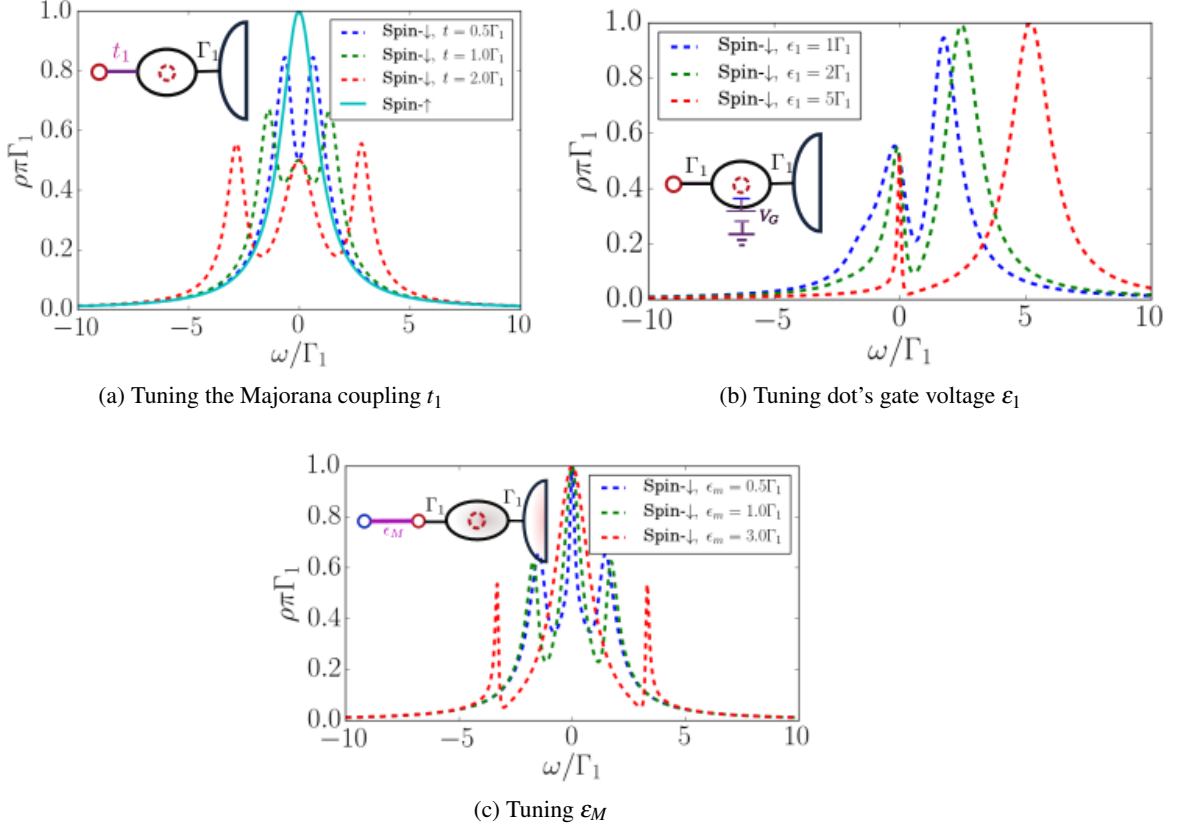


Figure 5.3: Density of states for a Majorana coupled to a QD under the tuning of different parameter. The tuning parameter is drawn in purple line in the inset model.

- **Figure 5.3.(c),(d):** This time a gate voltage is induced in the dot which breaks PHS. However the robust 0.5-height Majorana signature prevails in the dot even at very high gate voltages where the dot is expected to be empty. This result is similar to the one in [37], where the is attached to the last cite of the Kitaev chain.
- **Figure 5.3.(e),(f):** The term ϵ_M couples both Majoranas at the edges of the chain. The strength of this parameter decays exponentially with the length of the Majorana chain so that it is often neglected . Here we observe the consequences of including this parameter

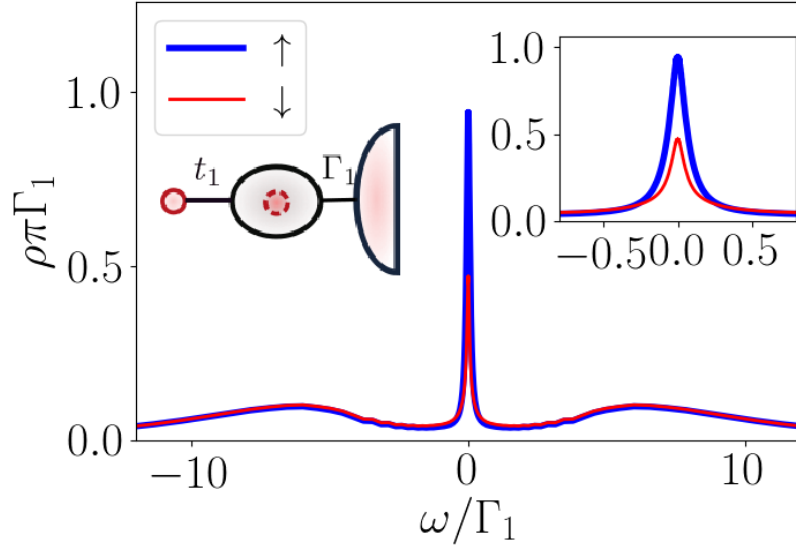


Figure 5.4: DOS at $t_1 = \Gamma_1$ at the PHS-point. Insets: Left: QD-Majorana model. Right: Zoom to low energy DOS..

in the model. The spin- \downarrow DOS for energies $\omega < \varepsilon_M$ is forced to take the same value of the the spin- \uparrow DOS. This clearly destroys the Majorana zero mode in the dot.

5.3 Kondo-Majorana physics

In interacting quantum dots the Kondo effect is visible at low temperatures even when the QD is attached to a Majorana chain, which allows the study Kondo-Majorana physics. To observe this , we used the NRG code with a fixed Coulomb repulsion of $U = 17.6\Gamma_1$ just as in section subsection 4.2.7. Then, particle-hole equilibrium is achieved when $(\varepsilon_1 + \frac{U_1}{2}) \hat{n}_{1\sigma}$. Any tunning of the dots gate voltage must be understood as a displacement $\Delta\varepsilon_1$ from this equilibrium point.

Figure 5.4 shows the PHS case for a Majorana coupling $t_1 = \Gamma_1$. The two small wide peaks at the borders of the plot are the coulomb states. In the right inset of the figure, we observe the low-temperature regime inside the gap. There, two zero modes can be appreciated. While the spin- \uparrow DOS is the same Kondo peak from Figure 4.8a, the spin- \downarrow DOS reveals a Majorana zero mode of half the amplitude of the Kondo peak $(\frac{0.5}{\pi\Gamma_1})$. This Majorana signature resembles the one in Figure 5.3a.

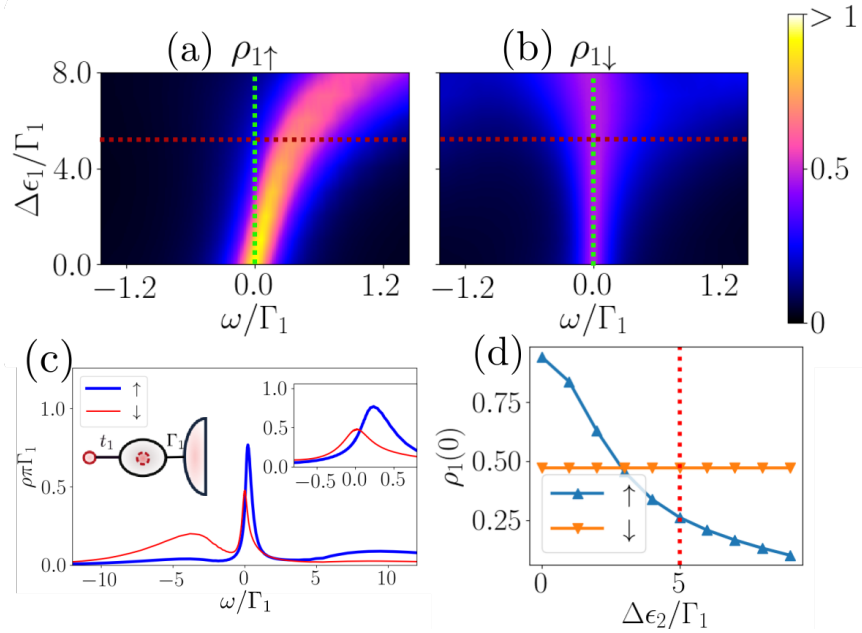


Figure 5.5: (a)&(b): Dependance of the DOS over the gate voltage $\Delta\epsilon_1$ at $t_1 = \Gamma_1$. (a) Spin- \uparrow (b) Spin- \downarrow . (c) DOS at the red-dashed horizontal cut in (a)&(b). Insets: Left: QD-Majorana model. Right: Low energy DOS. (d) DOS at the Green-dashed vertical cut in (a)&(b). .

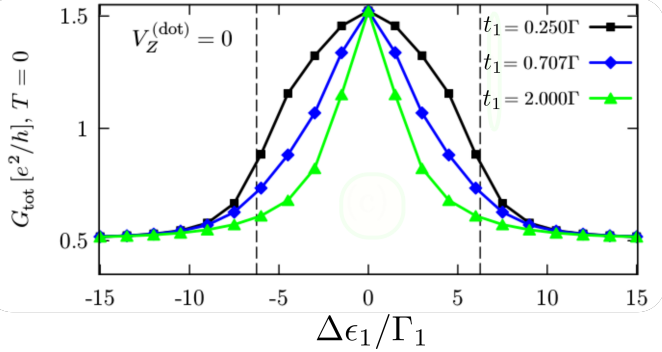


Figure 5.6: Dependence of the zero-bias conductance over tuning voltage *Adapted from [1]*.

It is possible to separate Kondo and Majorana physics by inducing a gate voltage in the dot. As observed in Figure 5.5(a), the gate voltage detunes the Kondo peak from the Fermi energy. Instead, the MZM in Figure 5.5(b) remains at the same position. At $\Delta\epsilon_1 = 5\Gamma_1$ we can already observe a decaying Kondo peak next to the robust Majorana signature of height $\frac{0.5}{\pi\Gamma}$ (Figure 5.5(c)). This is more clear in Figure 5.5(d) where the spin- \uparrow DOS decays with $\Delta\epsilon_1$

while the spin- \downarrow DOS is stable, even at $\Delta\epsilon_1 \sim \frac{U}{2} = 8.6$ where the dot is supposed to be empty.

This interesting result was already pointed out by Ruiz-Tijerina et al. who proved that increasing the gate voltage would produce a visible decay in the the zero bias conductance down to $\frac{0.5e^2}{h}$ (See Figure 5.6). Hence, allowing to measure the Majorana signature without the superposition with the Kondo peak. This result is clear from Figure 5.5. At $\Delta\epsilon = 0$ the DOS at the Fermi energy is $\frac{1}{\pi\Gamma_1}$ for spin- \uparrow and $\frac{0.5}{\pi\Gamma_1}$ for spin- \downarrow . Instead, at big $\Delta\epsilon_1$ the only $\frac{0.5}{\pi\Gamma_1}$ spin- \downarrow peak appear. Since the zero bias conductance at zero temperature is essentially the sum of both spectral densities (times unit correction), Figure 5.5 recovers the results in Figure 5.6.

Another possibility to distinguish Kondo and Majorana physics is quenching the Kondo effect with a strong magnetic field . Similar to what was observed in Figure 5.6, the Kondo peak will be destroyed while the Majorana signature remains stable [1].

In the next chapter we will use these ideas to study the model of DQD attached to a Majorana zero mode.

Chapter 6

Coupling the Majorana Zero Mode to a Double Quantum Dot

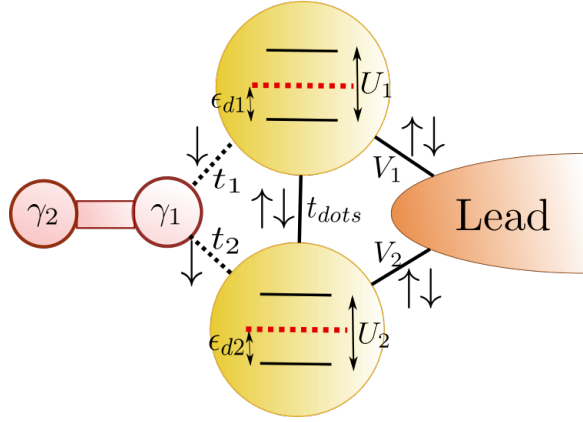


Figure 6.1: Model for the DQD-Majorana system. Solid lines: Hopping interactions (t_{dots} : inter-dot coupling , V_1, V_2 couplings of QD1 and QD2 with the lead). Dashed lines: Majorana spin- \downarrow effective couplings (5.2) t_1, t_2 . The atomic energy levels appear inside each QD ϵ_1, ϵ_2 are tuned by the gate voltages. The coulomb interaction is represented by U_1, U_2 . The red dashed horizontal lines represent the Fermi level.

The DQD-Majorana model is the most fundamental structure where Majorana manipulation is possible. Tunneling Majorana modes in this device have already inspired a few theoretical studies [41, 42] and experimental setups confirming the observations of Andreev molecules [40]. However, there is still no complete analysis of the transitions of the Majorana signatures between the QDs in this model, even though quantum tunneling of a MZM into a double dot offers several possibilities for MZM manipulation.

In this chapter, we will explore different possibilities for Majorana manipulation in a device consisting of a DQD coupled to a MZM and a metallic lead (See Figure 6.1). The simplicity of this model allows us to explore analytically different geometries of QD's from linear and symmetric couplings to T-junctions (Fig. Figure 6.3). As in the previous models , we will consider both non-interacting and interacting regimes.

The model in Figure 6.1 can be described from the combination of the Hamiltonians of a

6.1. Applying our methods to the DQD-Majorana system

QD-Majorana system (5.4) and a DQD (4.18). Integrating these models we obtain

$$H = \sum_{i=1}^2 \sum_{k,\sigma} \left(\varepsilon_i + \frac{U_i}{2} \right) d_{i\sigma}^\dagger d_{i\sigma} + \frac{U_i}{2} (d_{i\sigma}^\dagger d_{i\sigma} - 1)^2 + t_i (\gamma d_{i,\downarrow} + d_{i,\downarrow}^\dagger \gamma) + V_i d_{i\sigma}^\dagger c_{k\sigma} + V_i^* c_{k\sigma}^\dagger d_{i\sigma}. \quad (6.1)$$

Where V_1, V_2 is the coupling of dots 1,2 to the lead. t_1, t_2 define the Majorana couplings with each dot. t_{dots} is the interdot coupling. $\varepsilon_1, \varepsilon_2$ are the energy levels of the dot, which are tuned by the the gate voltage and U_1, U_2 are the coulomb repulsion parameters.

6.1 Applying our methods to the DQD-Majorana system

6.1.1 Non-interacting Green function:

This new model is a combination between the DQD (Figure 4.1) and the Majorana-QD Figure 5.2(b). We can use the trick in section 5.2 to get rid of the Green function $G_{f_{\downarrow}, d_{1\downarrow}^\dagger}(\omega)$ for the second Majorana operator. This allows us to obtain the following transport equations

$$\begin{bmatrix} \omega - \varepsilon_1 & -V_1^* & -t_{dots} & -T_1 & 0 & 0 & 0 \\ -V_1 & \omega - \varepsilon_k & -V_2 & 0 & 0 & 0 & 0 \\ -t_{dots}^* & -V_2^* & \omega - \varepsilon_2 & -T_2 & 0 & 0 & 0 \\ -T_1^* & 0 & -T_2^* & \omega - \varepsilon_M & -T_2^* & 0 & -T_1 \\ 0 & 0 & 0 & -T_2 & \omega + \varepsilon_2 & V_2^* & t_{dots}^* \\ 0 & 0 & 0 & 0 & V_2 & \omega + \varepsilon_k & V_1 \\ 0 & 0 & 0 & -T_1 & t_{dots} & V_1^* & \omega + \varepsilon_1 \end{bmatrix} \begin{bmatrix} G_{d_{1\downarrow}, d_{1\downarrow}^\dagger}(\omega) \\ G_{c_{k\downarrow}, d_{1\downarrow}^\dagger}(\omega) \\ G_{d_{2\downarrow}, d_{1\downarrow}^\dagger}(\omega) \\ G_{f_{\downarrow}, d_{1\downarrow}^\dagger}(\omega) \\ G_{d_{2\downarrow}^\dagger, d_{1\downarrow}^\dagger}(\omega) \\ G_{c_{k\downarrow}^\dagger, d_{1\downarrow}^\dagger}(\omega) \\ G_{d_{1\downarrow}^\dagger, d_{1\downarrow}^\dagger}(\omega) \end{bmatrix} = \begin{bmatrix} 0 \\ 0 \\ 0 \\ 0 \\ 0 \\ 0 \\ 1 \end{bmatrix}, \quad (6.2)$$

where $T_i = \frac{t_i}{\sqrt{\omega + \varepsilon_M}}$.

The graph representing this equation is in Figure 6.2(a). Using the algorithm in subsection 4.1.3 we start eliminating vertexes $c_k, c_k^\dagger, d_{2,\downarrow}$ and $d_{2,\downarrow}^\dagger$ in that order. The self-energies associated to $d_{1,\downarrow}$ and $d_{1,\downarrow}^\dagger$ will be similar to the energy of the DQD (4.25) giving

$$\varepsilon_{DQD}^\pm = \pm \varepsilon_1 + \sum_{\mathbf{k}} \frac{V_1 V_1^*}{\omega - \varepsilon_{\mathbf{k}}} + \frac{\left\| \pm t_{dots} + \sum_{\mathbf{k}} \frac{V_1 V_2^*}{\omega - \varepsilon_{\mathbf{k}}} \right\|^2}{\omega \pm \varepsilon_2 - \sum_{\mathbf{k}} \frac{V_2 V_2^*}{\omega - \varepsilon_{\mathbf{k}}}}. \quad (6.3)$$

There is also a correction in the couplings between the Majorana mode and $d_{1,\downarrow}, d_{1,\downarrow}^\dagger$ given by

$$T_{\pm} = \pm t_1 \pm t_2 \frac{\left(\pm t_{dots} + \sum_{\mathbf{k}} \frac{V_1 V_2^*}{\omega - \varepsilon_{\mathbf{k}}} \right)}{\omega \pm \varepsilon_2 \pm \sum_{\mathbf{k}} \frac{V_2 V_2^*}{\omega - \varepsilon_{\mathbf{k}}}}. \quad (6.4)$$

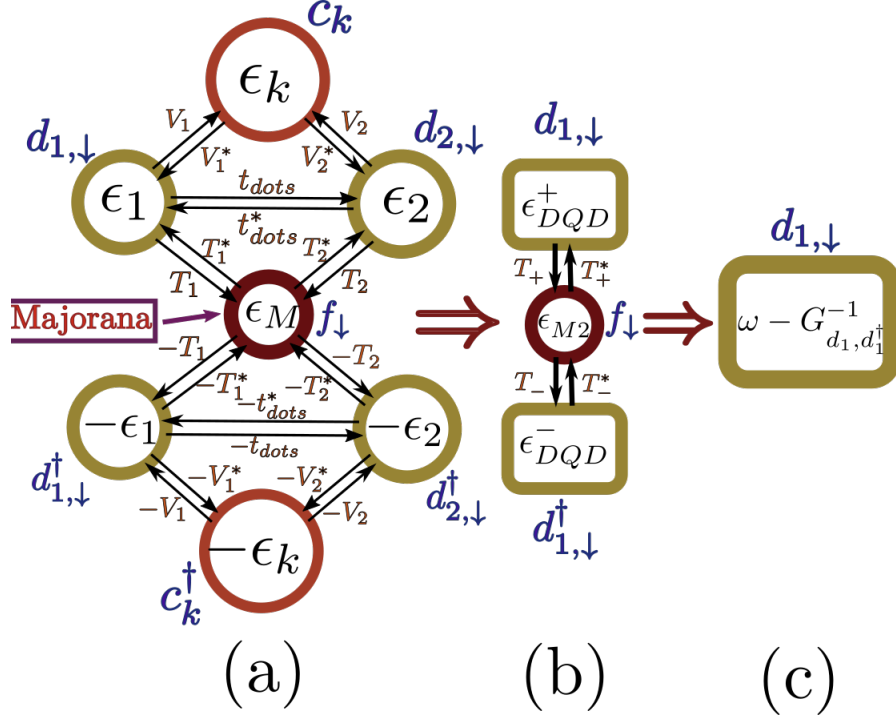


Figure 6.2: Graph method applied to a DQD coupled to a Majorana zero mode. a) Initial stage. b) Eliminated vertexes c_k^\dagger , c_k , $d_{2,\downarrow}$, $d_{2,\downarrow}^\dagger$ in that order. c) Eliminated vertexes $d_{1,\downarrow}^\dagger$ and f_\downarrow , the final energy is $\omega - G_{d_{1,\downarrow}, d_{1,\downarrow}^\dagger}^{-1}(\omega)$.

In addition, since the Majorana is in contact with dot 2, there is an extra-term appearing in the Majorana self-energy given by

$$\varepsilon_{M2} = \omega - \varepsilon_M - \frac{\frac{\omega}{\omega + \varepsilon_M} \|t_2\|^2}{\omega - \varepsilon_2 - \sum_{\mathbf{k}} \frac{V_2 V_2^*}{\omega - \varepsilon_{\mathbf{k}}}} - \frac{\frac{\omega}{\omega + \varepsilon_M} \|t_2\|^2}{\omega + \varepsilon_2 - \sum_{\mathbf{k}} \frac{V_2 V_2^*}{\omega + \varepsilon_{\mathbf{k}}}}. \quad (6.5)$$

It only remains to eliminate out vertexes d_1^\dagger and f_\downarrow to obtain the green function

$$G_{d_{1,\downarrow}, d_{1,\downarrow}^\dagger}(\omega) = \frac{1}{\omega - \varepsilon_{DQD}^+ - \frac{\|T_+\|^2}{\omega - \varepsilon_{M2} - \frac{\|T_-\|^2}{\varepsilon_{DQD}^-}}}. \quad (6.6)$$

This simple formula summarizes the transport information through the first dot of the non-interacting Majorana-DQD system. To compute the DOS we just need to replace $\sum \frac{V_i V_i^*}{\omega - \varepsilon_{\mathbf{k}}} = -i\Gamma_i$ as performed in subsection 4.1.2. By plotting the final DOS in Mathematica we were able to observe the transitions of the Majorana mode under manipulation of the model parameters.

6.1.2 NRG for the interacting system

The Numerical Renormalization Group (NRG) technique described in section 4.2 is the most successful methods to study interacting quantum impurity models. In this model, the impurity is described by the DQD attached to the MZM. In our code, we set a Coulomb repulsion factor of $U = 17.3\Gamma_1$ in both dots and a cut-off energy of $D = 2U = 34.6\Gamma_1$. The spacing with other energy levels is assumed to be higher than D , such that only the two coulomb states are relevant for the system dynamics. When $\varepsilon_i = \frac{U}{2}$ in both dots, the system is in the Particle-Hole-Symmetric region. At this point, each dot has an odd number of electrons, hence, at sufficiently low temperature the system will exhibit characteristic Kondo peaks at the Fermi energy [47]. The coexistence of Kondo and Majorana zero modes is still a point of contention in the area that has never been studied in DQDs and one of the objectives of this part of the project.

To improve the efficiency of the code we used the symmetries of the system to maintain a block structure during NRG's iterative diagonalization process. This model preserves the spin- \uparrow particle number \hat{N}_\uparrow and the spin- \downarrow parity $\hat{P}_\downarrow = \pm (+\text{even}, -\text{odd})$. The spin- \downarrow particle number is not preserved due to superconducting-type Majorana coupling (5.2). The initial Hamiltonian is organized in blocks according to these symmetries. This block structure is preserved during the entire iteration process [11]. To compute the spectral functions, we use the density matrix renormalization group (DM-NRG) described in subsection 4.2.5 in combination with the Z-trick method [56], which improves spectral resolution at high energies.

To initialize the model in Figure 4.7 we set H_{-1} equal to

$$H = \sum_{i=1}^2 \sum_{k,\sigma} \left(\varepsilon_i + \frac{U_i}{2} \right) d_{i\sigma}^\dagger d_{i\sigma} + \frac{U_i}{2} (d_{i\sigma}^\dagger d_{i\sigma} - 1)^2 + t_i (\gamma d_{i,\downarrow} + d_{i,\downarrow}^\dagger \gamma), \quad (6.7)$$

and wrote the Hamiltonian in the symmetry-block diagonal representation (see section A.2). We also include manually the Hamiltonian H_0 into the code (See Figure 4.7) to guarantee that both quantum dots are coupled to the first site of the chain. After this, the code follows the standard NRG algorithm and prints the density matrices to initialize DM-NRG. The final result is the spectral density which contains sufficient physical information to study the MZM-DQD model. In the following section, we show how the density of states can be used to simulate the Manipulation process of an MZM inside the DQD.

6.2 Manipulation of Majorana zero modes

The density of states provides significant information about the presence of a Majorana zero modes in the dot. We characterize the Majorana signature by a robust zero-mode with two possible heights:

- **Type I:** The spin- \downarrow DOS is the half of the spin- \uparrow DOS at the Fermi energy ($\rho_\downarrow(0) = \rho_\uparrow(0)$).

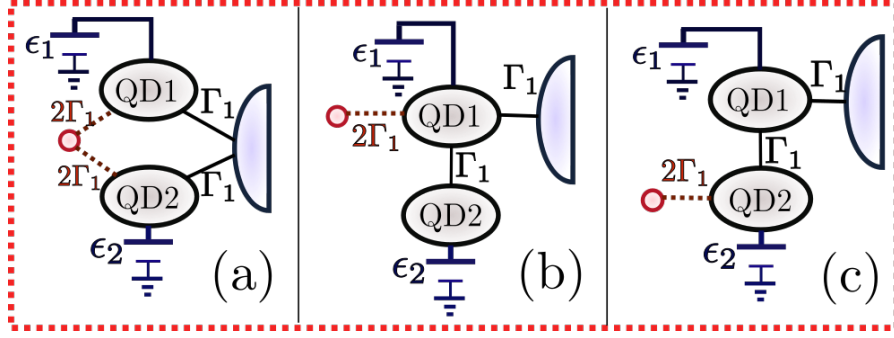


Figure 6.3: .

- **Type II:** A spin- \downarrow zero mode of height $\rho_{\downarrow}(0) = \frac{0.5}{\pi\Gamma_1}$.

In our results we observe several times these two types of signatures. Type I often appears when there is a zero-mode in the spin- \uparrow DOS, which is caused by the Kondo effect in the interacting case. Type II emerges in the remaining situations.

We call MZM manipulation to the "movements" attributed to the Majorana signature under the tunning of the dot gate voltages (ϵ_1, ϵ_2). This manipulation process is performed in three different set ups that are presented in Figure 6.3 with definite values of Γ_2, t_{dots}, t_1 and t_2 . In configuration (a), we coupled the QD symmetrically to the lead and the Majorana mode. With this setup we expect to break the localization of the MZM which should split and tunnel into both dots. In setups (b) and (c) we coupled the second dot indirectly through the first dot. Hence, quantum interference should split the zero mode in two states. Our objective is to observe what occurs with the Majorana signature in this situation. There are two options to connect the MZM in this situation. Attached it directly through the first dot (b) or indirectly through the second dot (c). Both alternatives are geometrically distinct since (b) suggests a T-junction coupling while (c) reflects a connection in series of both QD's between the lead and the MZM.

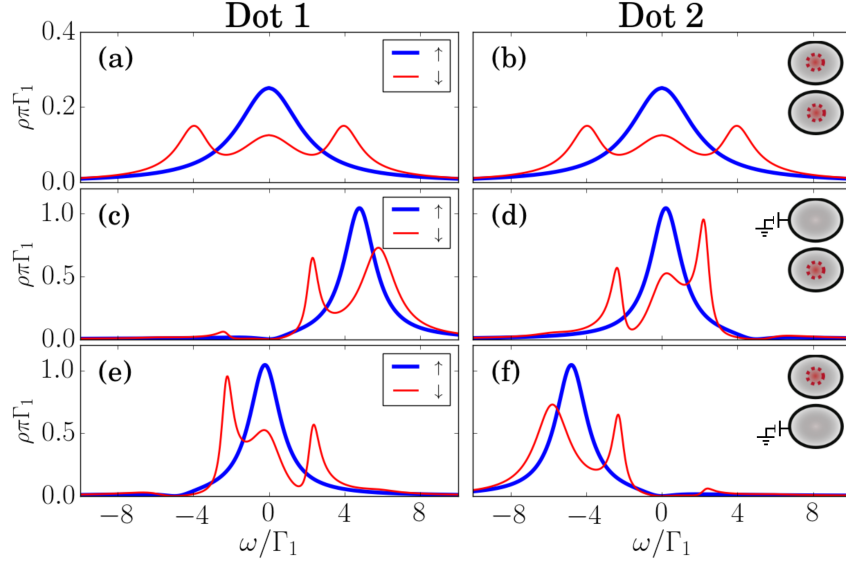


Figure 6.4: Non-interacting DOS in the symmetric coupling(Figure 6.3(a)) at each QD. First column: Dot 1. Second column: Dot 2. The gate voltages vary at each row. First row: Zero-bias in both dots $\varepsilon_1 = \varepsilon_2 = 0$. Second row: $\varepsilon_1 = 5\Gamma_1$, $\varepsilon_2 = 0$. Third row: $\varepsilon_1 = 0$, $\varepsilon_2 = -5\Gamma_1$. Bold blue lines: Spin- \uparrow DOS. Thin red lines: Spin- \downarrow DOS. The insets at the right show which dot carries a Majorana signature, represented by a red dashed circle. Upper: First dot. Lower: Second dot.

6.2.1 Non-interacting manipulation

The non-interacting results for setups (a),(b) and (c) of Figure 6.3 are shown at figures Figure 6.4, Figure 6.5 and Figure 6.6 respectively. Each figure depicts the DOS of dot 1(left) and dot 2(right). The gate voltage is initially 0 in both dots at the first row. In the second row, the gate voltage is turned on to $\varepsilon_1 = 5\Gamma_1$, while the second dot remains at $\varepsilon_2 = 0$. In the third row the first dot's voltage is off $\varepsilon_1 = 0$ and we switch on the second dot with a negative voltage of $\varepsilon_2 = -5\Gamma_1$. The inset figures at the right side of each row show which dots exhibit Majorana signatures, depicted by a red dashed circle inside the dot. These images will continuously change under the tuning of gate voltages which represents the manipulation of the Majorana signature.

In Figure 6.4 we observe the results for the symmetric coupling setup Figure 6.3(a). In the particle hole symmetric case (first row) the DOS is equal in both dots. Note that the spin- \downarrow (Thin red line) DOS is the half of the spin- \uparrow (Bold blue line) DOS at the Fermi energy ($\rho_{\downarrow}(0) = \frac{1}{2}\rho_{\uparrow}(0)$). This type II Majorana signature is similar to the one observed when a single dot is coupled to a Majorana mode. [36] We may conclude that the Majorana in tunneling inside both

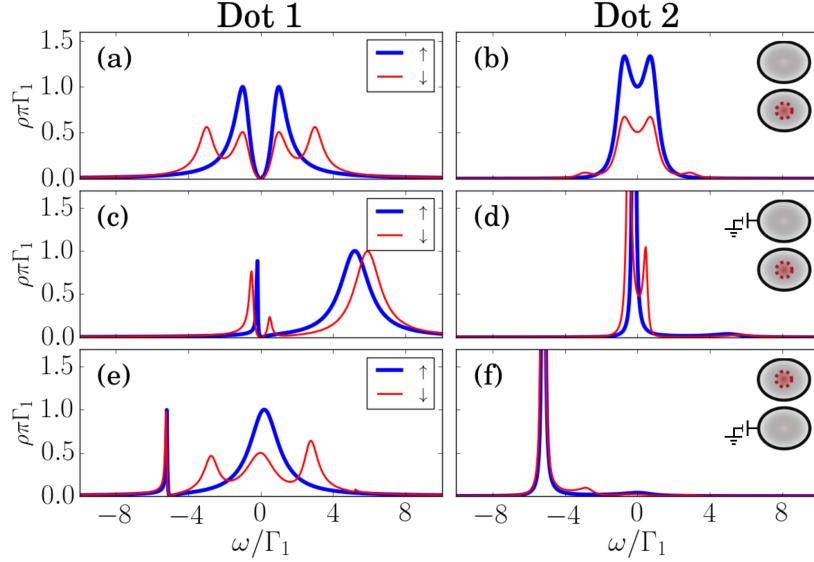


Figure 6.5: Non-interacting DOS of the T-dot coupling Figure 6.3(b). (b). First line (a),(b): $\varepsilon_1 = \varepsilon_2 = 0$. Second line (c),(d): $\varepsilon_1 = 5\Gamma_1$, $\varepsilon_2 = 0$. Third line (e),(f): $\varepsilon_2 = -5\Gamma_1$, $\varepsilon_1 = 0$. Blue bold lines: Spin- \uparrow DOS. Red thin lines: Spin- \downarrow DOS. The inset at the upper-right corner of each line indicates which dots exhibit Majorana signature, which is represented by a red dashed circle inside the dot.

dots breaking the localization of the MZM. If a positive or negative gate voltage is induced in one of the dots, as shown in the second and third row of Figure 6.4(c)-(f), the Majorana zero mode vanishes from that dot. Meanwhile the density of states in the other dot increases while preserving the Majorana signature. This means that the MZM is actually being induced to "leave" this dot and leak into the other by the biased voltage. This is the first example of MZM manipulation.

Another example can occur when the second dot is not directly connected to the lead. In this case, the inter-dot tunneling generates quantum interference which finally destroys the central peak as observed in Figure 6.5(a) at the spin- \uparrow DOS. The spin- \downarrow channel at Figure 6.5(a), which is coupled to the MZM, does not exhibit the characteristic Fermi peak either. Instead, the one half Majorana signature at the Fermi energy ($\rho_{\downarrow}(0) = \frac{1}{2}\rho_{\uparrow}(0)$) appears clearly inside the second dot Figure 6.5(b). This situation prevails when the first dot's gate voltage is turned on Figure 6.5(c)&(d). While the first dot does not seem to exhibit any type of Majorana signature, the second dot's spin- \downarrow DOS exhibits a robust zero-mode of height $\frac{0.5}{\pi\Gamma}$. The results are more exciting when the second dot's gate voltage is turned on in Figure 6.5(e)&(f). These figures clearly show how the MZM, previously localized at the second dot, is induced to leave this dot and to return into the first dot. Moreover, the DOS of spin- \uparrow and spin- \downarrow channels are very

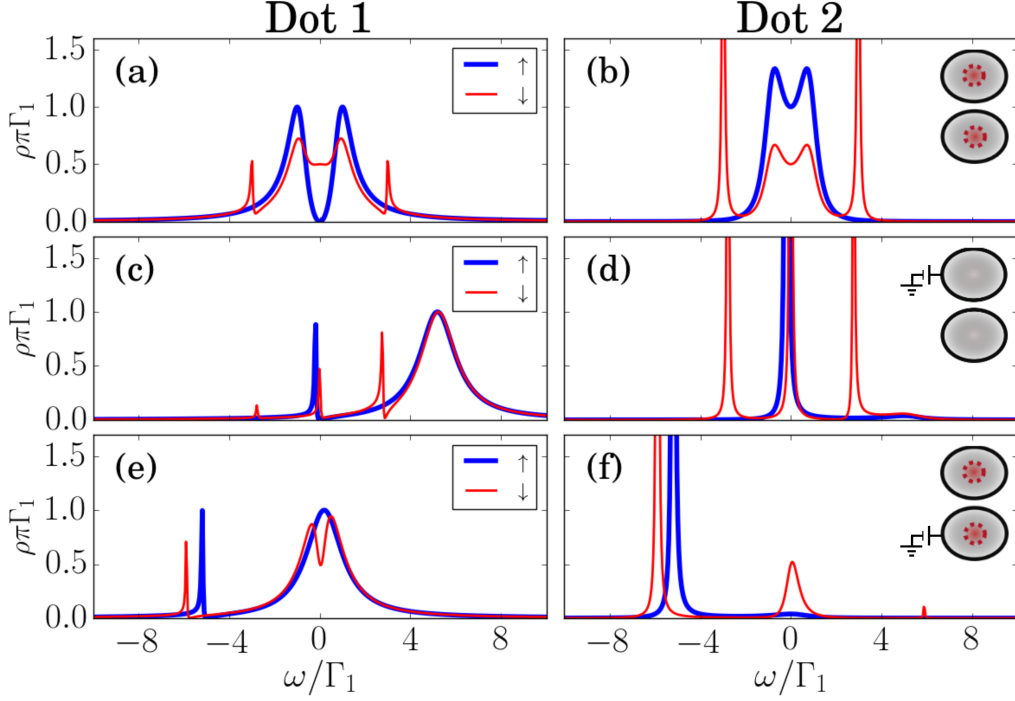


Figure 6.6: Non-interacting DOS of the set up in Figure 6.3(c). First line (a),(b): $\varepsilon_1 = \varepsilon_2 = 0$. Second line (c),(d): $\varepsilon_1 = 5\Gamma_1$, $\varepsilon_2 = 0$. Third line (e),(f): $\varepsilon_2 = -5\Gamma_1$, $\varepsilon_1 = 0$. Blue bold lines: Spin- \uparrow DOS. Red thin lines: Spin- \downarrow DOS. The inset at the upper-right corner of each line indicates which dots exhibit Majorana signature, which is represented by a red dashed circle inside the dot.

similar to the spectral densities observed at Figure 6.4(d)(e), which means that the previous interference pattern has disappeared due to this gate voltage.

The results of the third configuration Figure 6.3(c) appear in Figure 6.6. Contrary to what was observed in the previous case, this time the Majorana signature is not destroyed by the interference but instead, the $\frac{0.5}{\pi\Gamma}$ -height MZM emerges indirectly in the first dot. This is a perfect way to separate the Majorana's spin- \downarrow DOS from the central spin- \uparrow zero-mode which is still destroyed by the interference. In addition, the second dot still exhibits a type I Majorana signature as observed in Figure 6.6(b). In the second row we observe that turning on the gate voltage in dot 1 destroys the Majorana signature in both dots Figure 6.6(c)(d). On the other hand, if the second dot's voltage is switched both dots will preserve their Majorana signature (QD1:type I, QD2: type II), while the spin- \uparrow quantum interference vanishes in the first dot.

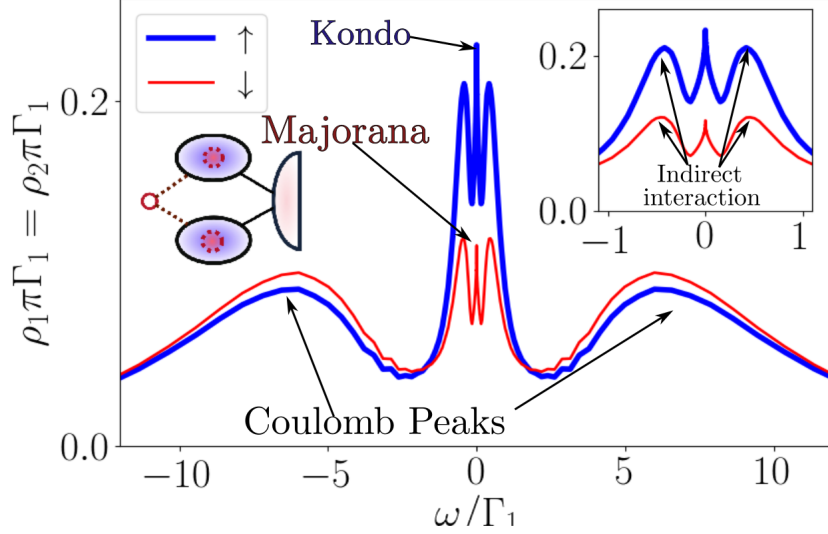


Figure 6.7: Density of states of both dots in the symmetric coupling without gate voltages between the Majorana and the interacting DQD. Bold blue lines: Spin- \uparrow DOS. Thin red lines: Spin- \downarrow DOS. Inset: Low-energy DOS.

6.2.2 Interacting manipulation

Now we consider a Coulomb repulsion energy of $U = 17\Gamma_1$ in both dots. The factor $\frac{U_i}{2}(\sum_{\sigma} \hat{n}_{i\sigma} - 1)^2$ in (6.1) favors states with an odd number of electrons (and holes). In addition, particle-hole equilibrium is now achieved when $\Delta\varepsilon_i := (\varepsilon_i + \frac{U_i}{2})$. Any induced gate voltage must be considered as a shifting $\Delta\varepsilon_i$ from this equilibrium point. Figure 6.7 shows the DOS of both QDs for the symmetric coupling configuration Figure 6.3. The two peaks appearing at around $8.6\Gamma_1 = \frac{U_i}{2}$ represent the two energy levels spaced by the Coulomb repulsion factor U . The central spin- \uparrow peak is a consequence of the Kondo effect, [47, 51] while the two satellite peaks observed in the inset are the result of the RKKY indirect interaction between both dots. [43–45] Moreover, the system presents a Majorana signature characterized by half spin- \downarrow DOS at the Fermi energy ($\rho_{\downarrow}(0) = \frac{1}{2}\rho_{\uparrow}(0)$). Note, that in this case the Majorana signature coexists with the Kondo effect in the DQD as already predicted by Ruiz-Tijerina *et al.* for a single dot. [1]

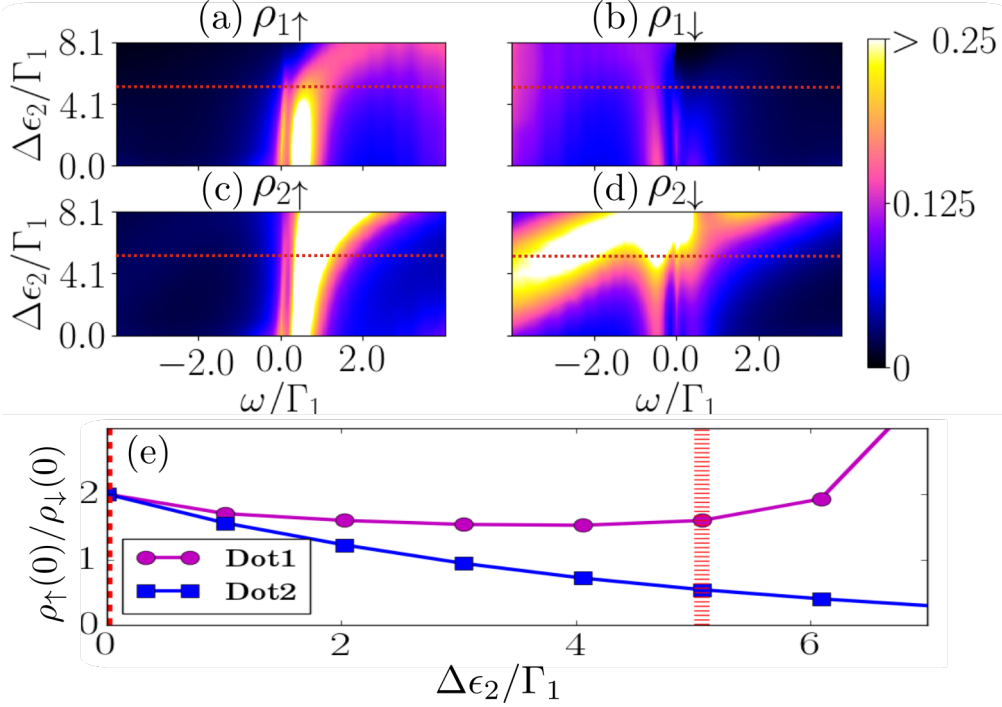


Figure 6.8: (a)-(d) Dependence of the density of states of setup in Figure 6.3(a) over ω and the gate voltage $\Delta\epsilon_2$. $\Delta\epsilon_1 = 0$ Up: Dot 1. Down: Dot 2. Left: Spin- \uparrow . Right: Spin- \downarrow . (e) Evolution of the relation $\frac{\rho_{\uparrow}(0)}{\rho_{\downarrow}(0)}$ for both QDs. While QD2 losses rapidly the Majorana signature, QD1 maintains it till $\Delta\epsilon_2 \sim 5$.

In this part of the project we are interested in the physics at low energy scales $\omega \sim \Gamma_1$ close to the Kondo and MZM temperature. At this scale we can observe similar Majorana signatures compared with the non-interacting case. For instance, the inset Figure 6.7 shows the NRG results for the symmetric setup in Figure 6.3(a). In agreement with the non-interacting results, both dots have type I Majorana signatures.

When the gate voltage is turned on, we observe the number of holes ($\omega > 0$) increasing in the spin- \uparrow , while the particles ($\omega < 0$) increase in the spin- \downarrow (See Figure 6.8(a)-(d)). At $\Delta\epsilon_2 \approx 6\Gamma_1$, the Coulomb peak overlaps with the Fermi energy in the spin- \downarrow channel, destroying the Majorana zero mode. This event is visible in Figure 6.8(e), where the type one Majorana signature is clearly destroyed in Dot 1 after $\Delta\epsilon_2 > 6\Gamma_1$. For $\Delta\epsilon_2 < 6\Gamma_1$ we observe a stable Majorana signature in dot 1 with $\rho_{\downarrow}(0) \approx \frac{1}{2}\rho_{\uparrow}(0)$). In the second dot the zero modes are absorbed by the dot, which slowly destroys the Majorana signature.

The red cuts in Figure 6.8 are plotted in Figure 6.9 where we depict the results of Majorana manipulation. In agreement with the non-interacting case, the particle hole symmetric model receives both Majorana modes. Whenever a gate voltage is switched on, the Majorana is forced

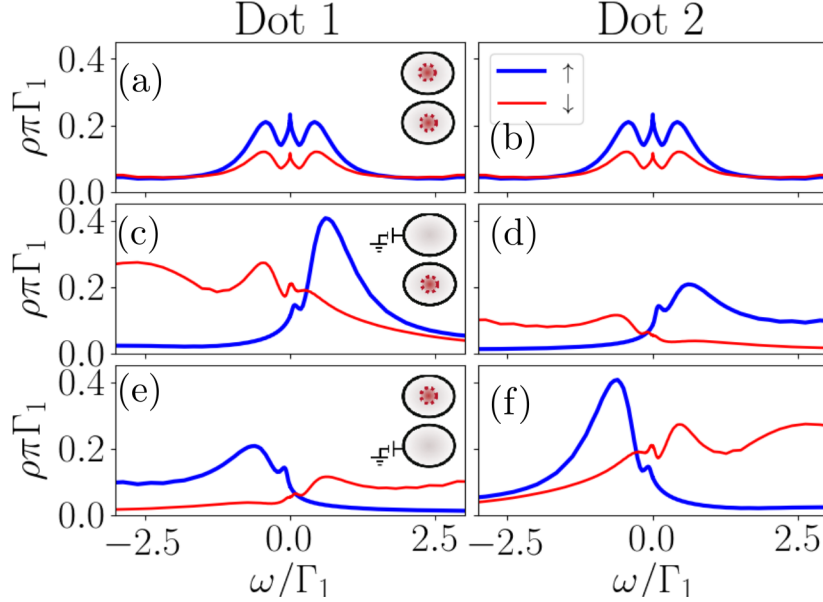


Figure 6.9: The same as in Figure 6.4 for the interacting DOS in the symmetric coupling setup (Figure 6.3).

to tunnel into the other dot. We observe similar results for positive and negative gate voltages.

In the T-dot coupling Figure 6.3(b), the spin- \uparrow Kondo peak in Figure 6.10 is destroyed by interference just as in the non-interacting case. This phenomenon had already been predicted for a T-junction of a double quantum dot attached to metallic leads [48]. The insight of our model is that an attached MZM should also disappear due to the same interference. Furthermore, a type I Majorana signature can be observed at very low energies in the inset of Figure 6.10(b). However we have to recognize that both zero-modes decay significantly in the second dot. When the first voltage is turned on, the Majorana mode jumps onto the first dot which presents a type I Majorana signature. This is a clear difference with the non-interacting results where the Majorana signature stayed in the second dot. If the second dot is switched on, a type II Majorana signature appears at very low energies in dot 1, which is coherent with the idea that the Majorana interference should disappear in this case. In Figure 6.10(e) we identify emergence of a Fano resonance at the Fermi energy causing the sharp-asymmetric peak at $\omega = 0$. Fano resonances have already been documented in similar models in [57]. We are going to talk more about this resonance in following section.

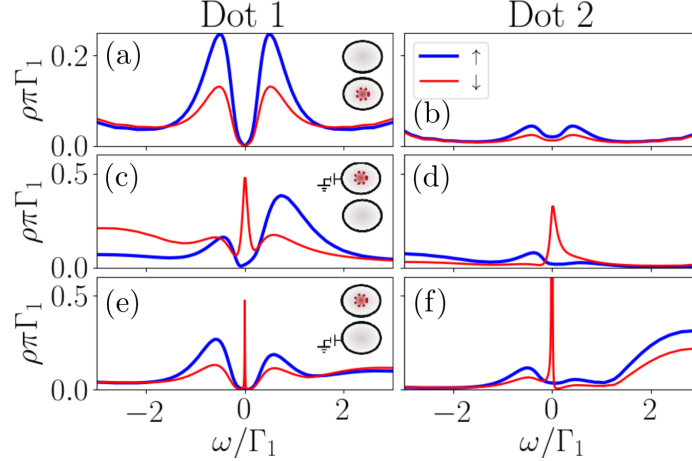


Figure 6.10: The same as in Figure 6.4 for the interacting DOS of the T-dot junction Figure 6.3(b). Inset in b): Low-energy DOS.

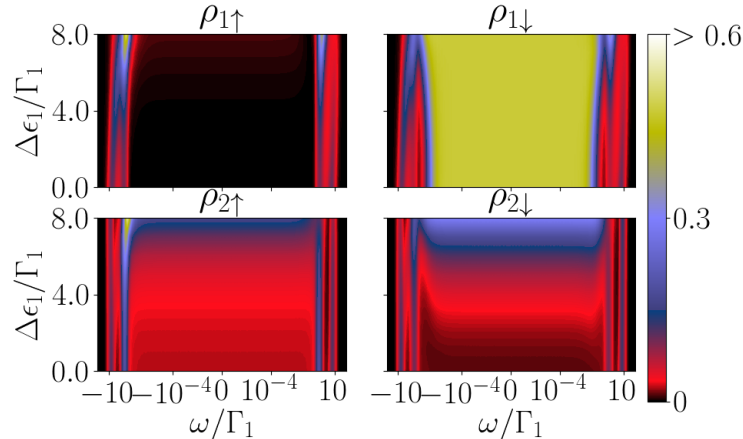


Figure 6.11: Logarithmic dependence of the density of states in setup Figure 6.3(c) over ω and the gate voltage $\Delta\epsilon_1$. $\Delta\epsilon_2 = 0$. The dependence over $\Delta\epsilon_2$ produces similar results.

Finally, Figure 6.12 shows the NRG results for the last configuration, where the dots are coupled in series Figure 6.3(c). Notably, the indirectly-attached MZM exhibits a robust type II Majorana signature in the first dot over a destroyed Kondo peak. This is observed clearly in Figure 6.11 where $\rho_{1\downarrow}$ exhibits a constant $\frac{0.5}{\pi\Gamma_1}$ -height Majorana peak. This signature is stable under the gate voltage tuning in dot 1 and similar results are obtained in dot 2. In addition, only in the particle hole symmetric case the second dot presents a type II Majorana signature (Inset

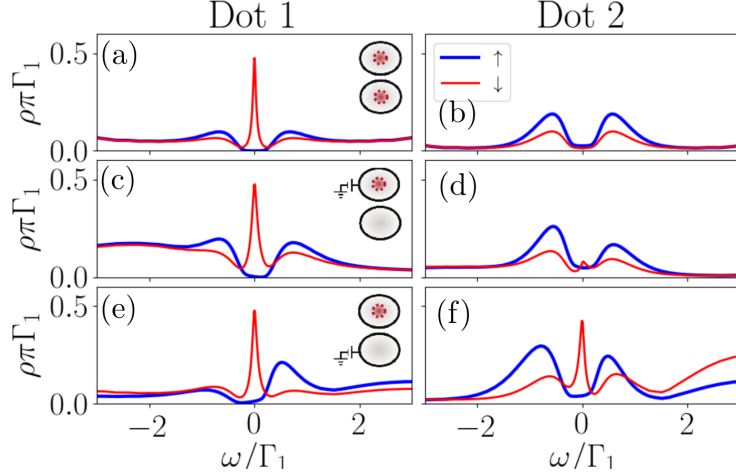


Figure 6.12: The same as in Figure 6.4 for the interacting DOS of the setup in Figure 6.3(b). Inset in b): Low-energy DOS.

Figure 6.12(b)).

We could understand this effect by thinking that the dots in model (c) are attached in series. Therefore both QDs can be thought as extensions of the Kitaev chain, were the first dot is the last place in the wire. Hence the Majorana should be localized at this dot despite the application of gate voltages. This situation is similar to the case of a single dot attached to a Majorana chain, where it is known that the MZM appears in the dot even when this is supposed to be empty [37]. It still remains the doubt about why this effect is not observed in the non-interacting case . On the other hand, there is a fano resonance at the Fermi energy in the spin- \downarrow DOS Figure 6.12(d)(e) . This zero mode was not identified as a potential Majorana signature since it varies with the values of $\Delta\varepsilon_1$ (Figure 6.11) and $\Delta\varepsilon_2$.

We are now writing a paper summarizing these results. As we observed, we were able to characterize the transitions of the Majorana signature in different geometric arrangements of the dots. In the following section we will present some ideas that are still in development. We hope they could lead us to future publications

6.3 Additional results

This section contains additional results which we are considering to study in future publications.

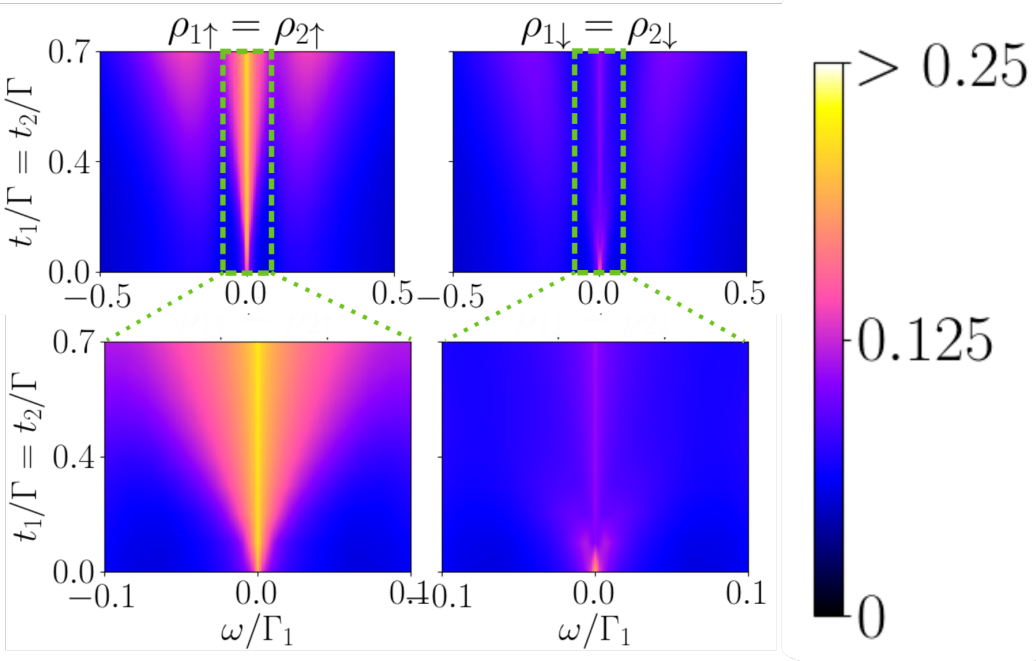


Figure 6.13: Dependence of the DOS in the symmetric model Figure 6.3(a) over $t_1 = t_2$ and ω . Up: High energy . Down: Zoom to low energy states.

6.3.1 Indirect exchange through the Majorana mode

In Figure 6.7 we observed the emergence of satellite peaks at low energies product of anti-ferromagnetic exchange interactions. This exchange interaction can occur through the lead and through the Majorana mode. The reason why we are observing just two satellites is because the Majorana couplings ($t_1 = t_2$) and the broadening parameters ($\Gamma_1 = \Gamma_2$) are about the same order. Hence the peaks are a superposition of both exchange interactions.

We can separate both exchange interactions by observing the dependence of the DOS at different orders of $t_1 = t_2$ in Figure 6.13. We can distinguish two regimes:

1. Low Majorana coupling $t_1 = t_2 < 0.5$: Two additional satellite peaks appear in the spin- \downarrow DOS (See inset in Figure 6.14 for better appreciation). These peaks are similar to the Kondo satellites that appear at high energies. However, since they appear only at low-energies, it is clear that they are produced by the MZM. We conclude that these two satellites are produced by the indirect exchange through the attached Majorana quasi-particle.
2. High Majorana coupling $t_1 = t_2 > 0.5$: When the Majorana coupling is high enough, the indirect exchange through the MZM occurs in the same energy scale as the Kondo sat-

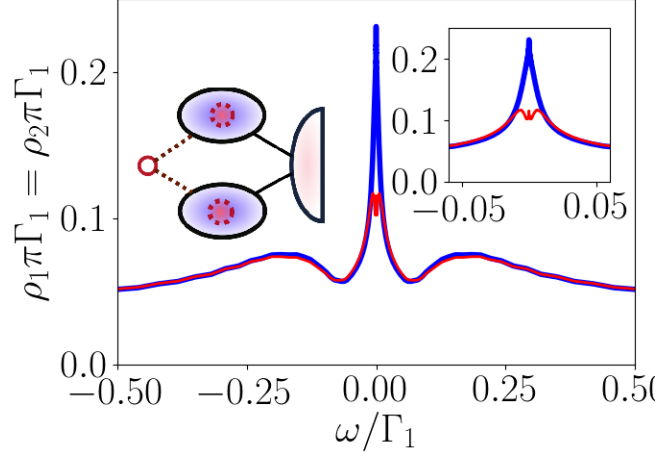


Figure 6.14: Dependence of the DOS in the symmetric model Figure 6.3(a) over $t_1 = t_2$ and ω . Up: High energy . Down: Zoom to low energy states.

lites. Notably, the spin- \downarrow satellite peaks in the high energy regime are not affected by this effect. Instead, a visible inflation of the satellites in the spin- \uparrow DOS is observed. Therefore the MZM is actually correlated with the spin- \uparrow DOS through the satellite peaks. This is unexpected since the Majorana is only coupled to the spin- \downarrow channel. The only explanation for this is that these satellites are formed by a strongly correlated state between the MZM, the dot states and the lead.

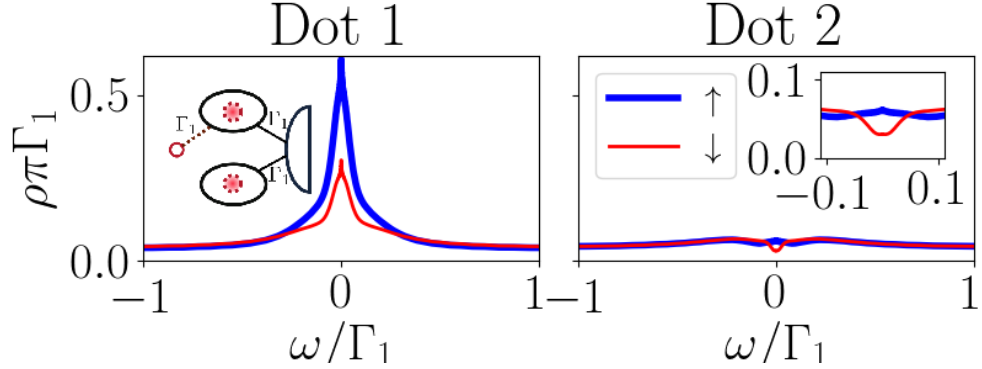


Figure 6.15: DOS at both dots for the model in the left inset. The right inset zooms the low-energy DOS in the second dot.

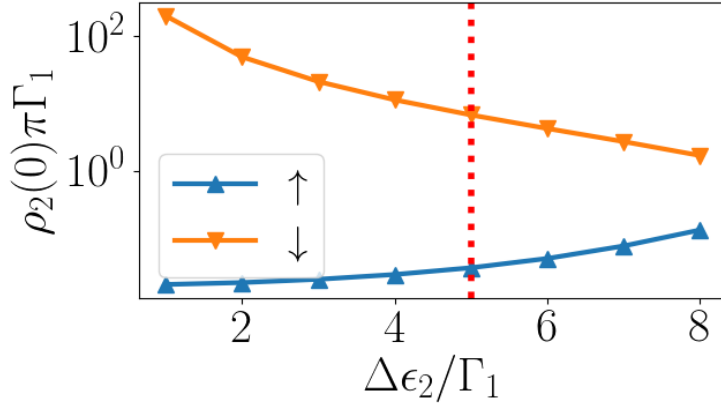


Figure 6.16: Logarithmic dependence of the DOS in the second dot for setup in Figure 6.3(b) over the second gate voltage. Cut at $5\Gamma_1$ corresponds to Figure 6.10(f).

6.3.2 Indirect Majorana coupling through the lead

Imagine a model where we connect both dots symmetrically to the leads but we only connect the MZM to the first dot. In addition, we do not allow inter-dot tunneling. Then the only connection between the MZM and the second dot would be passing through the first dot and the lead. We didn't expect to see any Majorana signature in the second dot in these conditions. However, Figure 6.15 shows a clear type I Majorana signature in the second dot.

Note also that the density of states in the second dot is very small in comparison with the first dot. This is intriguing since this dot is directly connected with the lead and it is still at the Kondo regime. This ambiguity means that the zero-bias DOS is favored by a direct coupling to an MZM.

6.3.3 Critical behavior in zero-bias DOS

In Figure 6.10(f) we observe a sharp peak at DOS. This peak is actually a big problem for our results since they are supported on the spectral densities at the Fermi energy. In Figure 6.16 we observe a critical behavior in the zero-bias DOS close to $\Delta\epsilon_2 = 0$. This is quite intriguing .

Chapter 7

Conclusions

In this work, we developed two methods to study the system of a double quantum dot attached to a Majorana chain. We probed successfully these methods in simpler cases such as the double quantum dot (subsection 4.1.4 , subsection 4.2.7) and the QD-Majorana system (chapter 5). The results obtained in these sections are in agreement with previous papers regarding the Kondo interference in double quantum dots [48], MZM leaking into quantum dots [36] and the co-existence of Kondo-Majorana physics [1].

Moreover, we introduced the Graph-Gauss-Jordan algorithm (subsection 4.1.2) as a simple, didactic, analytical and graphical method to solve the equations of motion. This method allowed us to obtain exact expressions for the non-interacting Green functions at several stages of the project. In particular, in the double quantum dot - Majorana model it proved to be extremely useful to simplify the complexity of the solution given by a fractional polynomial of 9th-degree in up to 7 variables. Furthermore, with this expression we were able to predict interesting parameters for simulation in the interacting regime. We hope for its extended use in condensed matter physics.

In chapter 6 we used the methods from chapter chapter 4 to study the transitions of the Majorana zero modes inside a double quantum dot. Comparing the exact analytical solution in the non-interacting system and the NRG results for interacting quantum dots, we were able to characterize the displacements of the MZM inside the double quantum dot for the three setups in Figure 6.3, representing a symmetric coupling, a T-dot junction and a linear coupling of the dots. All of these manipulations are summarized in Figure 7.1 . We observe a considerable agreement regarding the location of the Majorana signature between the interacting and non-interacting results with minor differences:

Symmetric coupling Figure 7.1 C.I : The MZM leaks inside both dots. For interacting dots, the Majorana signature will emerge near the Kondo temperature. At this regime the system presents combined Kondo-Majorana physics . Additional satellite peaks produced by the indirect exchange through the lead and the MZM appear at low energies. If the gate voltage of one dot is turned on the MZM is induced to tunnel only into the other dot, which is the key to MZM manipulation.

T-dot coupling Figure 7.1 C.II: The the spin-↑ zero mode at QD1 (The Kondo peak if the system is interacting) is destroyed by quantum interference with the second dot. This interference will also destroy the MZM in the first dot but a type I Majorana signature will still appear in the second dot. The Majorana mode can be induced to tunnel back

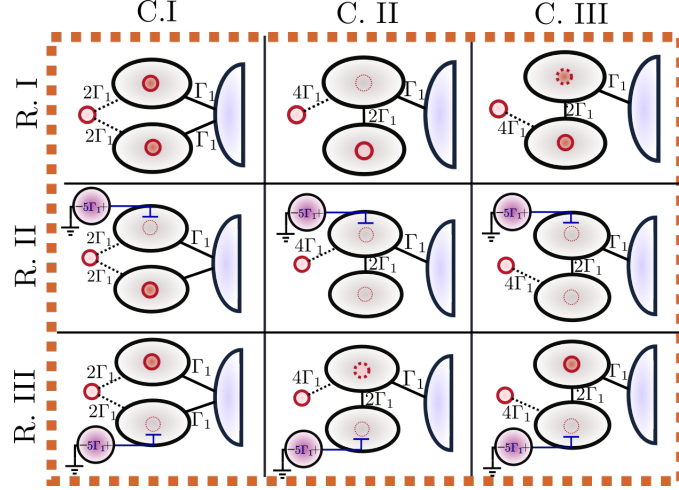


Figure 7.1: Table of Majorana signatures in the studied cases. Non-interacting .

into the first dot if a gate voltage is applied on the second dot. This signature is visible at very low energies (below $0.1\Gamma_1$) in the interacting case.

Dots coupled in series Figure 7.1 C.III : An indirect type II Majorana signature is observed in the first dot. This signature is robust, specially in the interacting case, where it is present in all configurations, despite gate voltage tuning. Fano resonances emerge in the second dot. One of them seems to have critical behavior.

Besides MZM manipulation we also pointed out other cases that could lead to future projects, such as the separation of the exchange interactions produced through the lead and through the MZM, the emergence of an indirect Majorana signature passing through the leads and the critical behavior in the T-dot junction when a gate voltage is applied on the second dot.

Bibliography

- [1] David A. Ruiz-Tijerina, E. Vernek, Luis G. G. V. Dias da Silva, and J. C. Egues. Interaction effects on a majorana zero mode leaking into a quantum dot. 91(11):115435. doi: 10.1103/PhysRevB.91.115435. URL <https://link.aps.org/doi/10.1103/PhysRevB.91.115435>. (document), 2, 7, 5.1, 5.6, 5.3, 6.2.2, 7
- [2] Jason Alicea. New directions in the pursuit of Majorana fermions in solid state systems. *Rep. Prog. Phys.*, 75(7):076501, 2012. ISSN 0034-4885. doi: 10.1088/0034-4885/75/7/076501. URL <http://stacks.iop.org/0034-4885/75/i=7/a=076501>. (document), 2, 2.1.1, 2.1.3, 2.6
- [3] Hao Zhang, Chun-Xiao Liu, Sasa Gazibegovic, Di Xu, John A. Logan, Guanzhong Wang, Nick van Loo, Jouri D. S. Bommer, Michiel W. A. de Moor, Diana Car, Roy L. M. Op het Veld, Petrus J. van Veldhoven, Sebastian Koelling, Marcel A. Verheijen, Mihir Pendharkar, Daniel J. Pennachio, Borzoyeh Shojaei, Joon Sue Lee, Chris J. Palmstrom, Erik P. A. M. Bakkers, S. Das Sarma, and Leo P. Kouwenhoven. Quantized Majorana conductance. *Nature*, 556:74, March 2018. URL <http://dx.doi.org/10.1038/nature26142>. (document), 2, 2.1.3, 2.7
- [4] Corneliu Malciu, Leonardo Mazza, and Christophe Mora. Braiding Majorana zero modes using quantum dots. *Physical Review B*, 98(16):165426, October 2018. doi: 10.1103/PhysRevB.98.165426. URL <https://link.aps.org/doi/10.1103/PhysRevB.98.165426>. (document), 3, 2.8
- [5] Torsten Karzig, Christina Knapp, Roman M. Lutchyn, Parsa Bonderson, Matthew B. Hastings, Chetan Nayak, Jason Alicea, Karsten Flensberg, Stephan Plugge, Yuval Oreg, Charles M. Marcus, and Michael H. Freedman. Scalable designs for quasiparticle-poisoning-protected topological quantum computation with Majorana zero modes. *Physical Review B*, 95(23):235305, June 2017. doi: 10.1103/PhysRevB.95.235305. URL <https://link.aps.org/doi/10.1103/PhysRevB.95.235305>. (document), 2.8
- [6] Alexander W. Holleitner, Robert H. Blick, Andreas K. Huttel, Karl Eberl, and Jorg P. Kotthaus. Probing and Controlling the Bonds of an Artificial Molecule. *Science*, 297(5578):70–72, July 2002. ISSN 0036-8075, 1095-9203. doi: 10.1126/science.1071215. URL <http://science.sciencemag.org/content/297/5578/70>. (document), 3.1

BIBLIOGRAPHY

- [7] Michael Sindel. *Numerical Renormalization Group studies of Quantum Impurity Models in the Strong Coupling Limit.* Text.PhDThesis, Ludwig-Maximilians-Universitat Munchen, January 2005. URL <https://edoc.ub.uni-muenchen.de/3115/>. (document), 3.1, 3.3, 3.2, 3.13, A.1
- [8] W.J. de Haas, J. de Boer, and G.J. van dĂ«n Berg. The electrical resistance of gold, copper and lead at low temperatures. *Physica*, 1(7):1115 – 1124, 1934. ISSN 0031-8914. doi: [https://doi.org/10.1016/S0031-8914\(34\)80310-2](https://doi.org/10.1016/S0031-8914(34)80310-2). URL <http://www.sciencedirect.com/science/article/pii/S0031891434803102>. (document), 3.4, 3.3
- [9] Markus Ternes, Andreas J Heinrich, and Wolf-Dieter Schneider. Spectroscopic manifestations of the kondo effect on single adatoms. *Journal of Physics: Condensed Matter*, 21(5):053001, dec 2008. doi: 10.1088/0953-8984/21/5/053001. URL <https://doi.org/10.1088%2F0953-8984%2F21%2F5%2F053001>. (document), 3.4
- [10] W. G. van der Wiel, S. De Franceschi, T. Fujisawa, J. M. Elzerman, S. Tarucha, and L. P. Kouwenhoven. The Kondo Effect in the Unitary Limit. *Science*, 289(5487):2105–2108, September 2000. ISSN 0036-8075, 1095-9203. doi: 10.1126/science.289.5487.2105. URL <http://science-sciencemag-org.ez67.periodicos.capes.gov.br/content/289/5487/2105>. (document), 3.5
- [11] Ralf Bulla, Theo A. Costi, and Thomas Pruschke. Numerical renormalization group method for quantum impurity systems. *Reviews of Modern Physics*, 80(2):395–450, April 2008. doi: 10.1103/RevModPhys.80.395. URL <https://link.aps.org/doi/10.1103/RevModPhys.80.395>. (document), 4.2.1, 4.2.1, 4.4, 6.1.2, A.1
- [12] Walter Hofstetter. Generalized Numerical Renormalization Group for Dynamical Quantities. *Physical Review Letters*, 85(7):1508–1511, August 2000. doi: 10.1103/PhysRevLett.85.1508. URL <https://link.aps.org/doi/10.1103/PhysRevLett.85.1508>. (document), 4.2.5, 4.6
- [13] A. Yu Kitaev. Unpaired Majorana fermions in quantum wires. *Phys.-Usp.*, 44(10S):131, 2001. ISSN 1063-7869. doi: 10.1070/1063-7869/44/10S/S29. URL <http://stacks.iop.org/1063-7869/44/i=10S/a=S29>. 2, 5.1
- [14] Frank Wilczek. Majorana returns, September 2009. URL <https://www.nature.com/articles/nphys1380>. 2
- [15] A. Yu Kitaev. Fault-tolerant quantum computation by anyons. *Annals of Physics*, 303(1):2–30, January 2003. ISSN 00034916. doi: 10.1016/S0003-4916(02)00018-0. URL <http://arxiv.org/abs/quant-ph/9707021>. arXiv: quant-ph/9707021. 2
- [16] Jiannis K. Pachos. *Introduction to Topological Quantum Computation*. Cambridge University Press, Cambridge ; New York, 1 edition edition, May 2012. ISBN 978-1-107-00504-4. 2, 2.1.2

BIBLIOGRAPHY

- [17] Vladimir G. Turaev. *Quantum Invariants of Knots and 3-Manifolds*. De Gruyter, Berlin, Boston, 3rd corr. ed. edition, 2016. ISBN 978-3-11-043522-1. URL <https://www.degruyter.com/view/product/461906>. 2, 2.1.2
- [18] Liang Fu and C. L. Kane. Superconducting Proximity Effect and Majorana Fermions at the Surface of a Topological Insulator. *Phys. Rev. Lett.*, 100(9):096407, March 2008. doi: 10.1103/PhysRevLett.100.096407. URL <https://link.aps.org/doi/10.1103/PhysRevLett.100.096407>. 2
- [19] Masatoshi Sato, Yoshiro Takahashi, and Satoshi Fujimoto. Non-Abelian Topological Order in \$s\$-\$s\$-Wave Superfluids of Ultracold Fermionic Atoms. *Phys. Rev. Lett.*, 103(2):020401, July 2009. doi: 10.1103/PhysRevLett.103.020401. URL <https://link.aps.org/doi/10.1103/PhysRevLett.103.020401>.
- [20] C.w.j. Beenakker. Search for Majorana Fermions in Superconductors. *Annual Review of Condensed Matter Physics*, 4(1):113–136, March 2013. ISSN 1947-5454. doi: 10.1146/annurev-conmatphys-030212-184337. URL <https://www.annualreviews.org/doi/10.1146/annurev-conmatphys-030212-184337>. 2
- [21] V. Mourik, K. Zuo, S. M. Frolov, S. R. Plissard, E. P. a. M. Bakkers, and L. P. Kouwenhoven. Signatures of Majorana Fermions in Hybrid Superconductor-Semiconductor Nanowire Devices. *Science*, 336(6084):1003–1007, May 2012. ISSN 0036-8075, 1095-9203. doi: 10.1126/science.1222360. URL <http://science-scienmag.org.ez67.periodicos.capes.gov.br/content/336/6084/1003>. 2, 2.1.3
- [22] Anindya Das, Yuval Ronen, Yonatan Most, Yuval Oreg, Moty Heiblum, and Hadas Shtrikman. Zero-bias peaks and splitting in an Al-InAs nanowire topological superconductor as a signature of Majorana fermions. *Nature Physics*, 8(12):887, December 2012. ISSN 1745-2481. doi: 10.1038/nphys2479. URL <https://www.nature.com/articles/nphys2479>. 2.1.3
- [23] M. T. Deng, C. L. Yu, G. Y. Huang, M. Larsson, P. Caroff, and H. Q. Xu. Anomalous Zero-Bias Conductance Peak in a Nb-InSb Nanowire-Nb Hybrid Device. *Nano Letters*, 12(12):6414–6419, December 2012. ISSN 1530-6984. doi: 10.1021/nl303758w. URL <http://dx.doi.org/10.1021/nl303758w>.
- [24] M. T. Deng, S. Vaitiekenas, E. B. Hansen, J. Danon, M. Leijnse, K. Flensberg, J. Nygård, P. Krogstrup, and C. M. Marcus. Majorana bound state in a coupled quantum-dot hybrid-nanowire system. *Science*, 354(6319):1557–1562. ISSN 0036-8075, 1095-9203. doi: 10.1126/science.aaf3961. URL <http://science.scienmag.org/content/354/6319/1557>. 2, 2.1.3, 2.2
- [25] Yuval Oreg, Gil Refael, and Felix von Oppen. Helical Liquids and Majorana Bound States in Quantum Wires. *Physical Review Letters*, 105(17):177002, October 2010.

BIBLIOGRAPHY

- doi: 10.1103/PhysRevLett.105.177002. URL <https://link.aps.org/doi/10.1103/PhysRevLett.105.177002>. 2
- [26] Roman M. Lutchyn, Jay D. Sau, and S. Das Sarma. Majorana Fermions and a Topological Phase Transition in Semiconductor-Superconductor Heterostructures. *Physical Review Letters*, 105(7):077001, August 2010. doi: 10.1103/PhysRevLett.105.077001. URL <https://link.aps.org/doi/10.1103/PhysRevLett.105.077001>. 2, 2.1.3
 - [27] Shinsei Ryu, Andreas P. Schnyder, Akira Furusaki, and Andreas W. W. Ludwig. Topological insulators and superconductors: tenfold way and dimensional hierarchy. *New Journal of Physics*, 12(6):065010, June 2010. ISSN 1367-2630. doi: 10.1088/1367-2630/12/6/065010. URL <https://doi.org/10.1088%2F1367-2630%2F12%2F6%2F065010>. 2.1.1
 - [28] Chetan Nayak, Steven H. Simon, Ady Stern, Michael Freedman, and Sankar Das Sarma. Non-Abelian anyons and topological quantum computation. *Reviews of Modern Physics*, 80(3):1083–1159, September 2008. doi: 10.1103/RevModPhys.80.1083. URL <https://link.aps.org/doi/10.1103/RevModPhys.80.1083>. 2.1.2
 - [29] A. Manchon, H. C. Koo, J. Nitta, S. M. Frolov, and R. A. Duine. New perspectives for Rashba spin-orbit coupling. *Nature Materials*, 14(9):871–882, September 2015. ISSN 1476-4660. doi: 10.1038/nmat4360. URL <https://www.nature.com/articles/nmat4360>. 2.1.3
 - [30] Stevan Nadj-Perge, Ilya K. Drozdov, Jian Li, Hua Chen, Sangjun Jeon, Jungpil Seo, Allan H. MacDonald, B. Andrei Bernevig, and Ali Yazdani. Observation of Majorana fermions in ferromagnetic atomic chains on a superconductor. *Science*, 346(6209):602–607, October 2014. ISSN 0036-8075, 1095-9203. doi: 10.1126/science.1259327. URL <http://science.sciencemag.org/content/346/6209/602>. 2.1.3
 - [31] S. Das Sarma, Jay D. Sau, and Tudor D. Stanescu. A Majorana smoking gun for the superconductor-semiconductor hybrid topological system. *Physical Review B*, 86(22), December 2012. ISSN 1098-0121, 1550-235X. doi: 10.1103/PhysRevB.86.220506. URL <http://arxiv.org/abs/1211.0539>. arXiv: 1211.0539. 2.1.3
 - [32] G. Górski, J. Barański, I. Weymann, and T. DomaÅski. Interplay between correlations and Majorana mode in proximitized quantum dot. *Scientific Reports*, 8(1):15717, October 2018. ISSN 2045-2322. doi: 10.1038/s41598-018-33529-1. URL <https://www.nature.com/articles/s41598-018-33529-1>. 2.1.3, 2
 - [33] David Aasen, Michael Hell, Ryan V. Mishmash, Andrew Higginbotham, Jeroen Danon, Martin Leijnse, Thomas S. Jespersen, Joshua A. Folk, Charles M. Marcus, Karsten Flensberg, and Jason Alicea. Milestones Toward Majorana-Based Quantum Computing. *Physical Review X*, 6(3):031016, August 2016. doi: 10.1103/PhysRevX.6.031016. URL <https://link.aps.org/doi/10.1103/PhysRevX.6.031016>. 2.1.3

BIBLIOGRAPHY

- [34] Sankar Das Sarma, Michael Freedman, and Chetan Nayak. Majorana zero modes and topological quantum computation. *npj Quantum Information*, 1:15001, October 2015. ISSN 2056-6387. doi: 10.1038/npjqi.2015.1. URL <https://www.nature.com/articles/npjqi20151>.
- [35] B. van Heck, A. R. Akhmerov, F. Hassler, M. Burrello, and C. W. J. Beenakker. Coulomb-assisted braiding of Majorana fermions in a Josephson junction array. *New Journal of Physics*, 14(3):035019, March 2012. ISSN 1367-2630. doi: 10.1088/1367-2630/14/3/035019. URL <https://doi.org/10.1088/2.1.3>
- [36] Dong E. Liu and Harold U. Baranger. Detecting a majorana-fermion zero mode using a quantum dot. 84(20). ISSN 1098-0121, 1550-235X. doi: 10.1103/PhysRevB.84.201308. URL <http://arxiv.org/abs/1107.4338>. 2.2, 2.3, 5, 5.1, 5.2, 6.2.1, 7
- [37] E. Vernek, P. H. Penteado, A. C. Seridonio, and J. C. Egues. Subtle leakage of a majorana mode into a quantum dot. 89(16):165314. doi: 10.1103/PhysRevB.89.165314. URL <https://link.aps.org/doi/10.1103/PhysRevB.89.165314>. 2.2, 2, 5.1, 5.2, 6.2.2
- [38] Eduardo J. H. Lee, Xiaocheng Jiang, Ramón Aguado, Georgios Katsaros, Charles M. Lieber, and Silvano De Franceschi. Zero-Bias Anomaly in a Nanowire Quantum Dot Coupled to Superconductors. *Physical Review Letters*, 109(18):186802, October 2012. doi: 10.1103/PhysRevLett.109.186802. URL <https://link.aps.org/doi/10.1103/PhysRevLett.109.186802>. 2
- [39] Minchul Lee, Jong Soo Lim, and Rosa Lopez. Kondo effect in a quantum dot side-coupled to a topological superconductor. 87(24):241402. doi: 10.1103/PhysRevB.87.241402. URL <https://link.aps.org/doi/10.1103/PhysRevB.87.241402>. 2
- [40] Zhaoen Su, Alexandre B. Tacla, Moira Hocevar, Diana Car, Sébastien R. Plissard, Erik P. A. M. Bakkers, Andrew J. Daley, David Pekker, and Sergey M. Frolov. Andreev molecules in semiconductor nanowire double quantum dots. *Nature Communications*, 8(1):585, September 2017. ISSN 2041-1723. doi: 10.1038/s41467-017-00665-7. URL <https://www.nature.com/articles/s41467-017-00665-7>. 2.2, 2.2.1, 6
- [41] Joelson F Silva and E Vernek. Andreev and majorana bound states in single and double quantum dot structures. *Journal of Physics: Condensed Matter*, 28(43):435702, sep 2016. doi: 10.1088/0953-8984/28/43/435702. URL <https://doi.org/10.1088%2F0953-8984%2F28%2F43%2F435702>. 2.2.1, 6
- [42] T. I. Ivanov. Coherent tunneling through a double quantum dot coupled to Majorana bound states. *Physical Review B*, 96(3):035417, July 2017. doi: 10.1103/PhysRevB.96.035417. URL <https://link.aps.org/doi/10.1103/PhysRevB.96.035417>. 2.2.1, 6

BIBLIOGRAPHY

- [43] M. A. Ruderman and C. Kittel. Indirect Exchange Coupling of Nuclear Magnetic Moments by Conduction Electrons. *Physical Review*, 96(1):99–102, October 1954. doi: 10.1103/PhysRev.96.99. URL <https://link.aps.org/doi/10.1103/PhysRev.96.99>. 2.2.1, 6.2.2
- [44] Tadao Kasuya. A Theory of Metallic Ferro- and Antiferromagnetism on Zener’s Model. *Progress of Theoretical Physics*, 16(1):45–57, July 1956. ISSN 0033-068X. doi: 10.1143/PTP.16.45. URL <https://academic.oup.com/ptp/article/16/1/45/1861363>.
- [45] Kei Yosida. Magnetic Properties of Cu-Mn Alloys. *Physical Review*, 106(5):893–898, June 1957. doi: 10.1103/PhysRev.106.893. URL <https://link.aps.org/doi/10.1103/PhysRev.106.893>. 2.2.1, 6.2.2
- [46] D. N. Zubarev. DOUBLE-TIME GREEN FUNCTIONS IN STATISTICAL PHYSICS. *Soviet Physics Uspekhi*, 3(3):320, 1960. ISSN 0038-5670. doi: 10.1070/PU1960v003n03ABEH003275. URL <http://iopscience.iop.org/article/10.1070/PU1960v003n03ABEH003275/meta>. 2.3, 4
- [47] Kenneth G. Wilson. The renormalization group: Critical phenomena and the Kondo problem. *Reviews of Modern Physics*, 47(4):773–840, October 1975. doi: 10.1103/RevModPhys.47.773. URL <https://link.aps.org/doi/10.1103/RevModPhys.47.773>. 2.3, 4.2.1, 6.1.2, 6.2.2
- [48] Luis G. G. V. Dias da Silva, Nancy Sandler, Kevin Ingersent, and Sergio E. Ulloa. Transmission in double quantum dots in the Kondo regime: Quantum-critical transitions and interference effects. *Physica E: Low-dimensional Systems and Nanostructures*, 40(5):1002–1005, March 2008. ISSN 1386-9477. doi: 10.1016/j.physe.2007.08.098. URL <http://www.sciencedirect.com/science/article/pii/S1386947707003074>. 2.3, 4.2.7, 3, 5, 6.2.2, 7
- [49] Dieter Bimberg, Marius Grundmann, and Nikolai N. Ledentsov. *Quantum Dot Heterostructures*. Wiley, Chichester, Eng.; New York, 1 edition, March 1999. ISBN 978-0-471-97388-1. 3.1, 3.1
- [50] P. W. Anderson. Localized Magnetic States in Metals. *Physical Review*, 124(1):41–53, October 1961. doi: 10.1103/PhysRev.124.41. URL <https://link.aps.org/doi/10.1103/PhysRev.124.41>. 3.2
- [51] Alexander Cyril Hewson. *The Kondo Problem to Heavy Fermions*. Cambridge University Press, April 1997. ISBN 978-0-521-59947-4. Google-Books-ID: fPzgHneNFDAC. 3.3, 1, 6.2.2
- [52] D. Goldhaber-Gordon, Hadas Shtrikman, D. Mahalu, David Abusch-Magder, U. Meirav, and M. A. Kastner. Kondo effect in a single-electron transistor. *Nature*, 391(6663):156–

159, January 1998. ISSN 1476-4687. doi: 10.1038/34373. URL <https://www.nature.com/articles/34373>. 3.3.1

- [53] Daniel A Spielman. Algorithms, graph theory, and linear equations in laplacian matrices. In *Proceedings of the International Congress of Mathematicians*, volume 4, pages 2698–2722, 2010. URL <http://www.mathunion.org/ICM/ICM2010.4/Main/icm2010.4.2698.2722.pdf>. 4.1.2, 4.1.2
- [54] H. R. Krishna-murthy, J. W. Wilkins, and K. G. Wilson. Renormalization-group approach to the Anderson model of dilute magnetic alloys. 1. Static properties for the symmetric case. *Phys.Rev.*, B21:1003–1043, 1980. doi: 10.1103/PhysRevB.21.1003. 4.2.1, 4.2.1, A.1, A.1
- [55] T. A. Costi, A. C. Hewson, and V. Zlatic. Transport coefficients of the Anderson model via the numerical renormalization group. *Journal of Physics: Condensed Matter*, 6(13):2519, 1994. ISSN 0953-8984. doi: 10.1088/0953-8984/6/13/013. URL <http://stacks.iop.org/0953-8984/6/i=13/a=013>. 4.2.5
- [56] Wanda C. Oliveira and Luiz N. Oliveira. Generalized numerical renormalization-group method to calculate the thermodynamical properties of impurities in metals. *Physical Review B*, 49(17):11986–11994, May 1994. doi: 10.1103/PhysRevB.49.11986. URL <https://link.aps.org/doi/10.1103/PhysRevB.49.11986>. 4.2.6, 6.1.2
- [57] Alexander Schuray, Luzie Weithofer, and Patrik Recher. Fano resonances in Majorana bound states–quantum dot hybrid systems. *Physical Review B*, 96(8):085417, August 2017. doi: 10.1103/PhysRevB.96.085417. URL <https://link.aps.org/doi/10.1103/PhysRevB.96.085417>. 6.2.2

Appendix A

Appendix

A.1 From the logarithmic discretization to the Wilson's chain.

Logarithmic Discretization:

We start with an Anderson model Hamiltonian such as the one in (3.6) without magnetic field

$$H = \frac{U}{2} + \sum_{\sigma} \left[\left(\varepsilon_d + \frac{U}{2} \right) d_{\sigma}^{\dagger} d_{\sigma} + \frac{U}{2} (d_{\sigma}^{\dagger} d_{\sigma} - 1)^2 + \sum_{\mathbf{k}} \varepsilon_{\mathbf{k}} c_{\mathbf{k}\sigma}^{\dagger} c_{\mathbf{k}\sigma} + V_{\mathbf{k}} d_{\sigma}^{\dagger} c_{\mathbf{k}\sigma} + V_{\mathbf{k}}^* c_{\mathbf{k}\sigma}^{\dagger} d_{\sigma} \right]. \quad (\text{A.1})$$

At low-energies we can assume that QD couples only to s-wave states in the leads[54]. This implies that that the Fermi surface is contained in a single, isotropic conduction band extending inside some fixed cutoffs $-D$ and D . Thus, $\varepsilon_{\mathbf{k}}$ only depends on $|\mathbf{k}|$. This makes possible to transform the sum over \mathbf{k} in equation A.1 into an integral over ε between the energy cutoffs

$$\begin{aligned} H = \sum_{\sigma} & \left[\left(\varepsilon_d + \frac{U}{2} \right) d_{\sigma}^{\dagger} d_{\sigma} + \frac{U}{2} (d_{\sigma}^{\dagger} d_{\sigma} - 1)^2 + \int_{-D}^D d\varepsilon \varepsilon c_{\varepsilon\sigma}^{\dagger} c_{\varepsilon\sigma} \right. \\ & \left. + \int_{-D}^D \sqrt{\rho_{\sigma}(\varepsilon)} d\varepsilon V_{\varepsilon} d_{\sigma}^{\dagger} c_{\mathbf{k}\sigma} + V_{\varepsilon}^* c_{\varepsilon\sigma}^{\dagger} d_{\sigma} \right]. \end{aligned} \quad (\text{A.2})$$

Here $c_{\varepsilon\sigma}^{\dagger}$ creates an electron with energy ε and $\rho_{\sigma}(\varepsilon)$ is the density of states of the system per spin, which appears in the integral due to the change of variable from \mathbf{k} to $\varepsilon \propto |\mathbf{k}|^2$. Finally, we ignore the energy dependence of ρ and V_d and we replace them by their values in the Fermi energy (This approximation has no great relevance which is justified in [54]) and we renormalize the energy band doing the replacements $k = \frac{\varepsilon}{D}$ and $c_{k\sigma} := \sqrt{D} c_{\varepsilon\sigma}$ so that (A.2) becomes

$$H = D \sum_{\sigma} \left[\frac{1}{D} \left(\varepsilon_d + \frac{U}{2} \right) d_{\sigma}^{\dagger} d_{\sigma} + \frac{U}{2D} (d_{\sigma}^{\dagger} d_{\sigma} - 1)^2 + \int_{-1}^1 dk k c_{k\sigma}^{\dagger} c_{k\sigma} \right] + \sqrt{\frac{\Gamma}{\pi D}} \int_{-1}^1 dk d_{\sigma}^{\dagger} c_{k\sigma} + c_{k\sigma}^{\dagger} d_{\sigma} \quad (\text{A.3})$$

$$= H_d + D \sum_{\sigma} \left[\int_{-1}^1 dk k c_{k\sigma}^{\dagger} c_{k\sigma} + \sqrt{\frac{\Gamma}{\pi D}} \int_{-1}^1 dk d_{\sigma}^{\dagger} c_{k\sigma} + c_{k\sigma}^{\dagger} d_{\sigma} \right], \quad (\text{A.4})$$

where $\Gamma = \pi \rho V^2$ is associated to the lever-width [7, (3.5)]. At this point we have our model dependent of three unit-less constants $\frac{\varepsilon_d}{D}$, $\frac{U}{2D}$ and $\frac{\Gamma}{\pi D}$. The logarithmic discretization starts by defining an scaling parameter $\Lambda \geq 1$ in diving the energy domain $[-1, 1]$ into an array of intervals of the form $\{[\pm \Lambda^{-(n+1)}, \pm \Lambda^n]\}_{n \in \mathbb{N}}$, as we can observe in Figure 4.3. Note that the width of these intervals is decreasing exponentially by

$$d_n = \Lambda^{-n} (1 - \Lambda^{-1}).$$

Then inside of these energy intervals we can define a set of orthonormal Fourier series of the form

$$\phi_{np}^{\pm}(\varepsilon) = \begin{cases} \frac{1}{\sqrt{d_n}} e^{\pm i \omega_n p \varepsilon} & \varepsilon \in [\pm \Lambda^{-(n+1)}, \pm \Lambda^n] \\ 0 & \text{a.o.c.} \end{cases} \quad (\text{A.5})$$

with $\omega_n := \frac{2\pi}{d_n}$ so that $\phi_{np}^{\pm}(\pm \Lambda^{-(n+1)}) = \phi_{np}^{\pm}(\pm \Lambda^{-n})$. Then we can decompose the creation operators c_k^{\dagger} into their interval-Fourier contributions as

$$c_k^{\dagger} = \sum_{np} \phi_{np}^{+}(k) c_{np\sigma}^{+\dagger} + \phi_{np}^{-}(k) c_{np\sigma}^{-\dagger} \quad (\text{A.6})$$

with the new creation operators defined as

$$c_{np\sigma}^{\pm\dagger} := (c_{np\sigma}^{\pm})^{\dagger} = \int_{-1}^1 d\varepsilon [\phi_{np}^{+}(\varepsilon)]^* c_{\varepsilon\sigma}^{\dagger}.$$

This decomposition (A.6) is a simple consequence of the orthonormality of the functions defined in (A.5). In addition we can readily proof that $c_{np\sigma}^{\pm\dagger}$ -operators satisfy the anti-commutation relations, so that they are rightful fermionic creation operators.

We can now use (A.6) to replace the k -dependent terms in hamiltonian (A.3). Then we obtain

$$\begin{aligned}
\int_{-1}^1 dk c_{k\sigma}^\dagger d_\sigma &= \int_{-1}^1 dk \left(\sum_{np} \phi_{np}^+(k) c_{np\sigma}^{+\dagger} + \phi_{np}^-(k) c_{np\sigma}^{-\dagger} \right) d_\sigma \\
&= \left(\sum_{np} \left(\int_{-1}^1 dk \phi_{np}^+(k) \right) c_{np\sigma}^{+\dagger} + \left(\int_{-1}^1 dk \phi_{np}^-(k) \right) c_{np\sigma}^{-\dagger} \right) d_\sigma \\
&= \left(\sum_{np} \left(\int_{\Lambda^{-(n+1)}}^{\Lambda^{-n}} dk \frac{e^{i\omega_n p k}}{\sqrt{d_n}} \right) c_{np\sigma}^{+\dagger} + \left(\int_{-\Lambda^{-n}}^{-\Lambda^{-(n+1)}} dk \frac{e^{-i\omega_n p k}}{\sqrt{d_n}} \right) c_{np\sigma}^{-\dagger} \right) d_\sigma \\
&= \left(\sum_{np} \sqrt{d_n} \delta_p c_{np\sigma}^{+\dagger} + \sqrt{d_n} \delta_p c_{np\sigma}^{-\dagger} \right) d_\sigma \\
&= \sqrt{1 - \Lambda^{-1}} \sum_n \Lambda^{-\frac{n}{2}} (c_{np\sigma}^{+\dagger} + c_{np\sigma}^{-\dagger}) d_\sigma. \tag{A.7}
\end{aligned}$$

And

$$\begin{aligned}
\int_{-1}^1 dk k c_{k\sigma}^\dagger c_{k\sigma} &= \sum_{n,n',p,p'} \sum_{s,s'=\pm} \left(\int_{-1}^1 k dk \phi_{np}^s(k) (\phi_{np}^{s'}(k))^* \right) c_{np\sigma}^{s\dagger} c_{n'p'\sigma}^{s'} \\
&= \sum_{n,n',p,p'} \sum_{s,s'=\pm} \left(\frac{\delta_{nn'} \delta_{ss'}}{d_n} \int_{\Lambda^{-(n+1)}}^{\Lambda^{-n}} k dk e^{is\omega_n k(p-p')} \right) c_{np\sigma}^{s\dagger} c_{n'p'\sigma}^s \\
&= \sum_{npp'} \sum_{s=\pm} \left(\frac{s}{2} \Lambda^{-2n} (1 - \Lambda^{-2}) \delta_{pp'} + \frac{1 - \delta_{pp'}}{is\omega_n(p-p')} [ke^{is\omega_n k(p-p')}]_{\Lambda^{-(n+1)}}^{\Lambda^{-n}} \right) \frac{c_{np\sigma}^{s\dagger} c_{n'p'\sigma}^{s'}}{d_n} \\
&= \frac{1}{2} (1 + \Lambda^{-1}) \sum_{np} \Lambda^{-n} (c_{np\sigma}^{+\dagger} c_{np\sigma}^+ - c_{np\sigma}^{-\dagger} c_{np\sigma}^-) \\
&\quad + \sum_n \sum_{p \neq p'} \frac{1 - \Lambda^{-1}}{2i\pi(p' - p)} (c_{np\sigma}^{+\dagger} c_{np'\sigma}^+ - c_{np'\sigma}^{-\dagger} c_{np\sigma}^-) e^{\frac{2i\pi(p-p')}{1-\Lambda^{-1}}}. \tag{A.8}
\end{aligned}$$

Thus, if we replace (A.7) and (A.8) into (A.3) we will obtain a logarithmic discretization of the hamiltonian. The next part will we to map this discretization to an iterative process that is worth for a numerical computations.

Mapping the Anderson model to a Chain-Hamiltonian

We are looking for a model just like the one we have in the right part of Figure 4.3(a). This is because a Chain-Hamiltonian will give an iterative approximation of the Anderson model with an increasing (but still controllable) number of degrees of freedom. This will provide the rightful structure for a numerical diagonalization of the hamiltonian.

A.1. From the logarithmic discretization to the Wilson's chain.

To do this, observe from equations (A.7),(A.8) that the QD (d_σ) couples directly only to the operators with $p = 0$ ($c_{n0\sigma}^{\pm\dagger}$). The $p \neq 0$ terms will appear in the hamiltonian only because they are coupled to $c_{np\sigma}^{+\dagger}$ in Equation (A.8). Thus, as a first approximation we can neglect all terms in (A.8) with $p \neq 0$. This leaves only the first part of (A.8), so that we can define $c_{n\sigma}^{\pm\dagger} := c_{np\sigma}^{\pm\dagger}$. Let

$$f_{0\sigma}^\dagger = \sqrt{\frac{1-\Lambda^{-1}}{2}} \sum_n \Lambda^{-\frac{n}{2}} (c_{n\sigma}^{+\dagger} + c_{n\sigma}^{-\dagger}), \text{ so that } \sqrt{2} f_{0\sigma}^\dagger d_\sigma = \int_{-1}^1 dk c_{k\sigma}^\dagger d_\sigma. \quad (\text{A.9})$$

Note $\{f_{0\sigma}^\dagger, f_{0\sigma}\} = \frac{1-\Lambda^{-1}}{2} \sum_n 2\Lambda^{-n} = 1$. Replacing this in (A.3)we get

$$H = H_d + D \sum_\sigma \left[\sqrt{\frac{2\Gamma}{\pi D}} (d_\sigma^\dagger f_{0\sigma} + f_{0\sigma}^\dagger d_\sigma) + \frac{1}{2} (1 + \Lambda^{-1}) \sum_n \Lambda^{-n} (c_{n\sigma}^{+\dagger} c_{n\sigma}^+ - c_{n\sigma}^{-\dagger} c_{n\sigma}^-) \right].$$

f_0^\dagger will represent the first site of the chain-hamiltonian in Figure 4.3(b) since no other term is coupled to the dot hamiltonian. We also have the coupling term $\xi_0 = \sqrt{\frac{2\Gamma}{\pi D}}$. It is possible to obtain the following f_m^\dagger -operators by supposing a solution of the form

$$f_{m\sigma}^\dagger = \sum_n a_{mn}^+ c_{n\sigma}^{+\dagger} + a_{mn}^- c_{n\sigma}^{-\dagger} = \sum_n \sum_{s=\pm} a_{mn}^s c_{n\sigma}^{s\dagger}, \quad (\text{A.10})$$

such that they satisfy the anti-commutation relations

$$\{f_{m\sigma}^\dagger, f_{m\sigma}\} = \delta_{mm'} \delta_{\sigma\sigma'}, \quad \{f_{m\sigma}^\dagger, f_{m'\sigma'}^\dagger\} = \{f_{m\sigma}^\dagger, f_{m\sigma}^\dagger\} = 0$$

and

$$\frac{1}{2} (1 + \Lambda^{-1}) \sum_n \Lambda^{-n} (c_{n\sigma}^{+\dagger} c_{n\sigma}^+ - c_{n\sigma}^{-\dagger} c_{n\sigma}^-) = \sum_{m=0}^{\infty} \Lambda^{-\frac{m}{2}} \xi_m (f_{m\sigma}^\dagger f_{m+1,\sigma} + f_{m+1,\sigma}^\dagger f_{m\sigma}). \quad (\text{A.11})$$

It is possible to find a solution for this system using the formula of the right part of equation A.11. Since the relation is only given between consecutive terms $m, m+1$ and we already have the coefficients for $m = 0$ ($a_{0n}^s = \sqrt{\frac{1-\Lambda^{-1}}{2}} \Lambda^{-\frac{n}{2}}$). Then it is possible to determine the upper coefficients in a recursive way starting from $m = 0$. Supposing we can obtain the m^{th} -coefficients (a_{mn}^s) and then finding iteratively the coefficients of $m+1$ ($a_{m+1,n}^s$) using the relation given by equation (A.11). This provides a numerical way for obtaining the $f_{m\sigma}^\dagger$ operators. In fact in our case, where we actually did important assumptions, the problem can be solved analytically obtaining that the final Hamiltonian is given by

$$H = H_d + D \sum_\sigma \left[\sqrt{\frac{2\Gamma}{\pi D}} (d_\sigma^\dagger f_{0\sigma} + f_{0\sigma}^\dagger d_\sigma) + \frac{1}{2} (1 + \Lambda^{-1}) \sum_{n=0}^{\infty} \Lambda^{-\frac{n}{2}} \xi_n (f_{n\sigma}^\dagger f_{n+1,\sigma} + f_{n+1,\sigma}^\dagger f_{n\sigma}) \right]. \quad (\text{A.12})$$

A.2. Initial DQD-Majorana Hamiltonian.

with

$$\xi_n = \frac{1 - \Lambda^{-n-1}}{(1 - \Lambda^{-2n-1})^{\frac{1}{2}} (1 - \Lambda^{-2n-3})^{\frac{1}{2}}}.$$

The formal recursive-solution of this problem can be found in [11]. Note that equation (A.12) describes the chain hamiltonian model that we where looking for in Figure 4.3(b). Note that in the limit when $n \rightarrow \infty$

$$\Lambda^{\frac{-n}{2}} \xi_n \rightarrow \frac{\Lambda^{\frac{-n}{2}} (1 - \Lambda^{-n})}{1 - \Lambda^{-2n}} \sim \frac{\Lambda^{\frac{-n}{2}}}{1 + \Lambda^{-n}},$$

which implies an exponential decaying of the hopping term in the chain.

A.2 Initial DQD-Majorana Hamiltonian.

$H_{N_\uparrow=0, P_\downarrow=-1}$:

$$\begin{aligned} |\downarrow, \downarrow, \downarrow\rangle &\rightarrow \left[\begin{array}{cccc} \varepsilon_d^+ + \frac{U^+}{2} - 2h + \varepsilon_m & 0 & -\tilde{t}_{+1} & \tilde{t}_{+2} \\ 0 & \frac{U^+}{2} + \varepsilon_m & \tilde{t}_{-2}^* & \tilde{t}_{-1}^* \\ -\tilde{t}_{+1}^* & \tilde{t}_{-2} & \varepsilon_{d_2} + \frac{U^+}{2} - h - \varepsilon_m & t \\ \tilde{t}_{+2}^* & \tilde{t}_{-1} & t^* & \varepsilon_{d_1} + \frac{U^+}{2} - h - \varepsilon_m \end{array} \right] \\ |0, 0, \downarrow\rangle &\rightarrow \left[\begin{array}{cccc} \frac{U^+}{2} - \varepsilon_m & 0 & \tilde{t}_{+1} & \tilde{t}_{+2} \\ 0 & \varepsilon_d^+ + \frac{U^+}{2} - 2h - \varepsilon_m & \tilde{t}_{-2}^* & -\tilde{t}_{-1}^* \\ \tilde{t}_{+1}^* & \tilde{t}_{-2} & \varepsilon_{d_1} + \frac{U^+}{2} - h + \varepsilon_m & t \\ \tilde{t}_{+2}^* & -\tilde{t}_{-1} & t^* & \varepsilon_{d_2} + \frac{U^+}{2} - h + \varepsilon_m \end{array} \right] \\ |0, \downarrow, 0\rangle &\rightarrow \left[\begin{array}{cccc} \frac{U^+}{2} - \varepsilon_m & 0 & \tilde{t}_{+1} & \tilde{t}_{+2} \\ 0 & \varepsilon_d^+ + \frac{U^+}{2} - 2h - \varepsilon_m & \tilde{t}_{-2}^* & -\tilde{t}_{-1}^* \\ \tilde{t}_{+1}^* & \tilde{t}_{-2} & f(d_1, d_2) + h - \varepsilon_m & -t \\ \tilde{t}_{+2}^* & -\tilde{t}_{-1} & -t^* & f(d_2, d_1) + h - \varepsilon_m \end{array} \right] \\ |\downarrow, 0, 0\rangle &\rightarrow \left[\begin{array}{cccc} \frac{U^+}{2} - \varepsilon_m & 0 & \tilde{t}_{+1} & \tilde{t}_{+2} \\ 0 & \varepsilon_d^+ + \frac{U^+}{2} - 2h - \varepsilon_m & \tilde{t}_{-2}^* & -\tilde{t}_{-1}^* \\ \tilde{t}_{+1}^* & \tilde{t}_{-2} & f(d_2, d_1) + h + \varepsilon_m & -t \\ \tilde{t}_{+2}^* & -\tilde{t}_{-1} & -t^* & f(d_1, d_2) + h + \varepsilon_m \end{array} \right] \end{aligned}$$

$H_{N_\uparrow=0, P_\downarrow=1}$:

$$\begin{aligned} |0, 0, 0\rangle &\rightarrow \left[\begin{array}{cccc} \frac{U^+}{2} - \varepsilon_m & 0 & \tilde{t}_{+1} & \tilde{t}_{+2} \\ 0 & \varepsilon_d^+ + \frac{U^+}{2} - 2h - \varepsilon_m & \tilde{t}_{-2}^* & -\tilde{t}_{-1}^* \\ \tilde{t}_{+1}^* & \tilde{t}_{-2} & \varepsilon_{d_1} + \frac{U^+}{2} - h + \varepsilon_m & t \\ \tilde{t}_{+2}^* & -\tilde{t}_{-1} & t^* & \varepsilon_{d_2} + \frac{U^+}{2} - h + \varepsilon_m \end{array} \right] \\ |\downarrow, \downarrow, 0\rangle &\rightarrow \left[\begin{array}{cccc} \frac{U^+}{2} - \varepsilon_m & 0 & \tilde{t}_{+1} & \tilde{t}_{+2} \\ 0 & \varepsilon_d^+ + \frac{U^+}{2} - 2h - \varepsilon_m & \tilde{t}_{-2}^* & -\tilde{t}_{-1}^* \\ \tilde{t}_{+1}^* & \tilde{t}_{-2} & f(d_1, d_2) + h - \varepsilon_m & -t \\ \tilde{t}_{+2}^* & -\tilde{t}_{-1} & -t^* & f(d_2, d_1) + h - \varepsilon_m \end{array} \right] \\ |\downarrow, 0, \downarrow\rangle &\rightarrow \left[\begin{array}{cccc} \frac{U^+}{2} - \varepsilon_m & 0 & \tilde{t}_{+1} & \tilde{t}_{+2} \\ 0 & \varepsilon_d^+ + \frac{U^+}{2} - 2h - \varepsilon_m & \tilde{t}_{-2}^* & -\tilde{t}_{-1}^* \\ \tilde{t}_{+1}^* & \tilde{t}_{-2} & f(d_2, d_1) + h + \varepsilon_m & -t \\ \tilde{t}_{+2}^* & -\tilde{t}_{-1} & -t^* & f(d_1, d_2) + h + \varepsilon_m \end{array} \right] \\ |0, \downarrow, \downarrow\rangle &\rightarrow \left[\begin{array}{cccc} \frac{U^+}{2} - \varepsilon_m & 0 & \tilde{t}_{+1} & \tilde{t}_{+2} \\ 0 & \varepsilon_d^+ + \frac{U^+}{2} - 2h - \varepsilon_m & \tilde{t}_{-2}^* & -\tilde{t}_{-1}^* \\ \tilde{t}_{+1}^* & \tilde{t}_{-2} & f(d_2, d_1) + h - \varepsilon_m & -t \\ \tilde{t}_{+2}^* & -\tilde{t}_{-1} & -t^* & f(d_1, d_2) + h - \varepsilon_m \end{array} \right] \end{aligned}$$

$H_{N_\uparrow=2, P_\downarrow=-1}$:

$$\begin{aligned} |\uparrow\downarrow, \uparrow\downarrow, \downarrow\rangle &\rightarrow \left[\begin{array}{cccc} 2\varepsilon_d^+ + \frac{3U^+}{2} + \varepsilon_m & 0 & \tilde{t}_{+1} & \tilde{t}_{+2} \\ 0 & \varepsilon_d^+ + \frac{U^+}{2} + 2h + \varepsilon_m & \tilde{t}_{-2}^* & -\tilde{t}_{-1}^* \\ \tilde{t}_{+1}^* & \tilde{t}_{-2} & f(d_1, d_2) + h - \varepsilon_m & -t \\ \tilde{t}_{+2}^* & -\tilde{t}_{-1} & -t^* & f(d_2, d_1) + h - \varepsilon_m \end{array} \right] \\ |\uparrow\uparrow, \uparrow\downarrow, \downarrow\rangle &\rightarrow \left[\begin{array}{cccc} 2\varepsilon_d^+ + \frac{3U^+}{2} + \varepsilon_m & 0 & \tilde{t}_{+1} & \tilde{t}_{+2} \\ 0 & 2\varepsilon_d^+ + \frac{3U^+}{2} - \varepsilon_m & \tilde{t}_{-2}^* & -\tilde{t}_{-1}^* \\ -\tilde{t}_{+1}^* & \tilde{t}_{-2} & f(d_2, d_1) + h + \varepsilon_m & -t \\ \tilde{t}_{+2}^* & \tilde{t}_{-1} & -t^* & f(d_1, d_2) + h + \varepsilon_m \end{array} \right] \\ |\uparrow\uparrow, \uparrow\downarrow, 0\rangle &\rightarrow \left[\begin{array}{cccc} 2\varepsilon_d^+ + \frac{3U^+}{2} + \varepsilon_m & 0 & \tilde{t}_{+1} & \tilde{t}_{+2} \\ 0 & 2\varepsilon_d^+ + \frac{3U^+}{2} - \varepsilon_m & \tilde{t}_{-2}^* & -\tilde{t}_{-1}^* \\ -\tilde{t}_{+1}^* & \tilde{t}_{-2} & f(d_2, d_1) + h + \varepsilon_m & -t \\ \tilde{t}_{+2}^* & \tilde{t}_{-1} & -t^* & f(d_1, d_2) + h + \varepsilon_m \end{array} \right] \\ |\uparrow\downarrow, \uparrow\downarrow, 0\rangle &\rightarrow \left[\begin{array}{cccc} 2\varepsilon_d^+ + \frac{3U^+}{2} + \varepsilon_m & 0 & \tilde{t}_{+1} & \tilde{t}_{+2} \\ 0 & 2\varepsilon_d^+ + \frac{3U^+}{2} - \varepsilon_m & \tilde{t}_{-2}^* & -\tilde{t}_{-1}^* \\ -\tilde{t}_{+1}^* & \tilde{t}_{-2} & f(d_2, d_1) + h - \varepsilon_m & -t \\ \tilde{t}_{+2}^* & \tilde{t}_{-1} & -t^* & f(d_1, d_2) + h - \varepsilon_m \end{array} \right] \end{aligned}$$

with $f(d_i, d_j) = \varepsilon_{d_i} + \frac{U_i}{2} + 2\varepsilon_{d_j} + \frac{3U_j}{2}$.

$H_{N_\uparrow=2, P_\downarrow=1}$:

$$\begin{aligned} |\uparrow\uparrow, \uparrow\downarrow, 0\rangle &\rightarrow \left[\begin{array}{cccc} \varepsilon_d^+ + \frac{U^+}{2} + 2h - \varepsilon_m & 0 & -\tilde{t}_{+1} & \tilde{t}_{+2} \\ 0 & 2\varepsilon_d^+ + \frac{3U^+}{2} - \varepsilon_m & \tilde{t}_{-2}^* & -\tilde{t}_{-1}^* \\ -\tilde{t}_{+1}^* & \tilde{t}_{-2} & f(d_2, d_1) + h + \varepsilon_m & -t \\ \tilde{t}_{+2}^* & \tilde{t}_{-1} & -t^* & f(d_1, d_2) + h + \varepsilon_m \end{array} \right] \\ |\uparrow\uparrow, \uparrow\downarrow, 0\rangle &\rightarrow \left[\begin{array}{cccc} \varepsilon_d^+ + \frac{U^+}{2} + 2h - \varepsilon_m & 0 & -\tilde{t}_{+1} & \tilde{t}_{+2} \\ 0 & 2\varepsilon_d^+ + \frac{3U^+}{2} - \varepsilon_m & \tilde{t}_{-2}^* & -\tilde{t}_{-1}^* \\ -\tilde{t}_{+1}^* & \tilde{t}_{-2} & f(d_2, d_1) + h - \varepsilon_m & -t \\ \tilde{t}_{+2}^* & \tilde{t}_{-1} & -t^* & f(d_1, d_2) + h - \varepsilon_m \end{array} \right] \\ |\uparrow\downarrow, \uparrow\downarrow, 0\rangle &\rightarrow \left[\begin{array}{cccc} \varepsilon_d^+ + \frac{U^+}{2} + 2h - \varepsilon_m & 0 & -\tilde{t}_{+1} & \tilde{t}_{+2} \\ 0 & 2\varepsilon_d^+ + \frac{3U^+}{2} - \varepsilon_m & \tilde{t}_{-2}^* & -\tilde{t}_{-1}^* \\ -\tilde{t}_{+1}^* & \tilde{t}_{-2} & f(d_2, d_1) + h + \varepsilon_m & -t \\ \tilde{t}_{+2}^* & \tilde{t}_{-1} & -t^* & f(d_1, d_2) + h + \varepsilon_m \end{array} \right] \\ |\uparrow\uparrow, \uparrow\downarrow, \downarrow\rangle &\rightarrow \left[\begin{array}{cccc} \varepsilon_d^+ + \frac{U^+}{2} + 2h - \varepsilon_m & 0 & -\tilde{t}_{+1} & \tilde{t}_{+2} \\ 0 & 2\varepsilon_d^+ + \frac{3U^+}{2} - \varepsilon_m & \tilde{t}_{-2}^* & -\tilde{t}_{-1}^* \\ -\tilde{t}_{+1}^* & \tilde{t}_{-2} & f(d_2, d_1) + h - \varepsilon_m & -t \\ \tilde{t}_{+2}^* & \tilde{t}_{-1} & -t^* & f(d_1, d_2) + h - \varepsilon_m \end{array} \right] \end{aligned}$$